**University of Alberta**

# The Effect of Microstructure on Near-Neutral-pH SCC

by

Jeffrey Thomas Bulger ©

A thesis submitted to the Faculty of Graduate Studies and Research in partial
fulfillment of the requirements for the degree of Master of Science

in

Materials Engineering

Department of Chemical and Materials Engineering

Edmonton, Alberta

Fall 2000

0-612-59785-7

# Abstract

The effect of microstructure on near-neutral-pH SCC and corrosion in the NS4 environment was investigated. Corrosion testing was performed on various heat treatments of API X-70 linepipe steel and AISI 1018 and 1045 carbon steel. In order to determine the corrosion rate, three different types of testing were used: polarization resistance, potentiodynamic scans and electrochemical impedance spectroscopy. Testing revealed that the corrosion rate of the steels involved was a function of the microstructure. Some of these microstructures were also subject to slow strain rate testing to determine their SCC performance. Again, the SCC performance was dependant on the microstructure. The SCC performance of the various microstructures had a direct relationship with their corrosion rate indicating that near-neutral-pH SCC has an anodic dissolution mechanism.

## Table of Contents

## List of Tables

## List of Figures

## List of Symbols

| Symbol | Meaning |
|---|---|
| a | atomic diameter |
| AISI | American Iron and Steel Institute |
| API | American Petroleum Institute |
| ASTM | American Society for Testing and Materials |
| CGHAZ | coarse grain heat affected zone |
| CV | crack velocity |
| $D_s$ | self-diffusion coefficient |
| $E_b$ | hydrogen-vacancy binding energy |
| $E_{corr}$ | corrosion potential |
| EDX | energy dispersive x-ray |
| EIC | environmentally induced cracking |
| EIS | electrochemical impedance spectroscopy |
| El | elongation |
| F | Faradays constant |
| FBE | fusion bonded epoxy |
| HRB | Rockwell B |
| HRC | Rockwell C |
| i | anodic current density |
| $i_{corr}$ | corrosion current density |
| $i_o(H^+/H_2)$ | exchange current density for the reduction of hydrogen |

| | |
|---|---|
| I.D. | inside diameter |
| k | Boltzmanns constant |
| $k_H$ | coefficient to account for the effect of hydrogen on the corrosion current |
| $k_{H\sigma}$ | coefficient to account for the combined effect of hydrogen and stress on the corrosion current |
| $k_\sigma$ | coefficient to account for the effect of stress on the corrosion current |
| K | stress-intensity factor |
| $\Delta K$ | difference between maximum and minimum stress-intensity factor |
| $K_C$ | fracture toughness |
| $K_{IC}$ | plane strain fracture toughness |
| $K_{ISCC}$ | critical stress intensity factor for SCC |
| $K_{max}$ | maximum stress-intensity factor |
| L | diffusion path length |
| mV | millivolts |
| $mV_{CCS}$ | millivolts versus a copper/copper sulfate electrode |
| $mV_{SCE}$ | millivolts versus a saturated calomel electrode |
| M | atomic weight |
| MVC | microvoid coalescence |
| OCP | open circuit potential |
| O.D. | outside diameter |

| | |
|---|---|
| P | pressure |
| PD | potentiodynamic scan |
| PE | polyethylene |
| PR | polarization resistance |
| Q+T | quenched and tempered |
| R | radius |
| R | stress ratio of minimum applied stress to maximum applied stress in during cyclic loading |
| $R^2$ | goodness of fit |
| RA | reduction of area |
| %RA | percent reduction in of area |
| $RA_{Air}$ | reduction of area of a specimen failed in air |
| $RA_{scc}$ | reduction of area of a specimen failed due to SCC |
| RH | right hand |
| $R_p$ | polarization resistance |
| $R_s$ | solution resistance |
| SCC | stress corrosion cracking |
| SEM | scanning electron microscope |
| SIMS | secondary ion mass spectrometry |
| SMYS | specified minimum yield strength |
| SSRT | slow strain rate test |
| t | thickness |
| T | absolute temperature |

| | |
|---|---|
| UNF | unified national fine |
| UTS | ultimate tensile strength |
| $V_{SCE}$ | voltage versus a saturated calomel electrode |
| $Z$ | valence of the solvated species |
| $Z_{Imag}$ | imaginary component of impedance |
| $Z_{Real}$ | real component of impedance |
| $\alpha$ | degree of hydrogen saturation of the vacancies at the crack tip |
| $\varepsilon_f$ | failure elongation |
| $\rho$ | density |
| $\sigma$ | stress |
| $\sigma_{app}$ | applied stress |
| $\sigma_{\tau\eta}$ | threshold stress for SCC |
| $\sigma_{ys}$ | yield stress |

# Chapter 1 Introduction

Stress corrosion cracking (SCC) is a time dependent cracking process that first became a known problem in the late 1800's with cracks developing in cold drawn brass cartridges. Over time the number of failures increased and the number of affected metals increased from cartridge brass to stainless steels, carbon steels, aluminum alloys, titanium alloys, nickel alloys, etc..

SCC failures of piping systems was identified early with failures occurring in the late 1800's of brass condenser tubing. However, in the 1960's SCC failures of underground pipelines were reported (Wenk, 1974) to have occurred on the external surface of pipelines even though the pipeline was thought to be completely protected with external coatings and cathodic protection. This type of SCC became known as classical SCC and received extensive research to find its mechanism and mitigation procedures.

After years of research and answers to many fundamental questions about classical SCC, external SCC failures on Canadian underground pipelines were reported (Delanty and O'Beirne, 1992) and were found to be vastly different from classical SCC failures and was therefore termed non-classical SCC. Although about half the failures that did occur resulted in leaks developing in the pipeline, several explosive failures forced the National Energy Board to hold an inquiry on SCC of Canadian pipelines (National Energy Board, 1996). The resulting report outlined the knowledge gained from field observations and research and outlined areas that required further investigation. This thesis presents one of the areas that to date has not received any attention, namely the effect of microstructure on non-classical SCC.

There are two main objectives of this study:

1) To investigate if microstructure affects the SCC susceptibility of pipeline steel;
2) To find if microstructure affects the corrosion rate of pipeline steel.

Chapter 2 covers a review of general SCC characteristics common to most SCC failures and then presents relevant field investigations and laboratory studies on SCC of pipelines.

Chapter 3 presents the experimental procedure that was used to meet the objectives of the study including various heat treatments and the nomenclature for referring to the different microstructures.

Chapters 4 through 6 present the results and discussion for the differences in the microstructures, the corrosion results and finally the SCC results.

Finally, conclusions are made in Chapter 7 along with recommendations for further research.

# Chapter 2 Literature Review

## *2.1 Introduction*

This chapter first presents an overview of the general characteristics and mechanisms of SCC and then concentrates on external pipeline SCC. Two types of pipeline SCC, classical and non-classical, are presented due to their similarities of material, environment and testing procedures. Both the field observations and the research on pipeline SCC are reviewed to illustrate the necessity of the research.

## *2.2 Definition of SCC*

SCC is a cracking process that is caused by the synergistic effect of corrosion and sustained tensile stress and leads to a macroscopically brittle failure. Although other types of materials fail due to the combined application of stress and corrosion, stress corrosion cracking is reserved for metallic alloys. Three components are required for SCC to occur: a SCC causing environment, a susceptible metal and tensile stress. Merely a combination of an environment, metal and tensile stress probably will not experience SCC since only certain combinations experience SCC, for instance carbonate/bicarbonate solutions are known to cause SCC of carbon steels but stainless steels are resistant in this environment.

The simultaneous occurrence of corrosion and stress is key to the definition of SCC. Individual application of either component may lead to failure, but the combined occurrence of tensile stress and corrosion may lead to a premature failure.

The tensile stresses involved in a SCC failure are normally below the macroscopic yield stress and are either externally applied or internal such as residual stresses from forming or welding operations. The type of external loading changes the type of failure with static loading causing a SCC and cyclic loading causing corrosion fatigue. However, a failure due to a small alternating component with a low frequency superimposed on a much larger tensile loading (as experience on a pipeline) is normally classified as a SCC failure.

Depending on the system (combination of environment/metal/stress), the crack path can either be intergranular or transgranular (or both) and can also have extensive branching. Normally SCC is associated with a group of cracks with some cracks propagating and others dormant. Since corrosion is a key component, cathodic protection usually suppresses SCC but excessive cathodic protection can lead to hydrogen embrittlement.

### *2.3 Stages of SCC*

SCC failures occur by a slow, environmentally induced process involving a series of events:

- Stage I: Initiation of conditions;
- Stage II: Crack initiation;
- Stage III: Steady crack growth;
- Stage IV: Crack coalescence;
- Final failure.

These stages are shown in Figure 2-1. The number of stages and the length of time spent in each stage depend on the system. For instance, a system may take a month to move through stage I and II while another system could take 10 years to complete these stages.

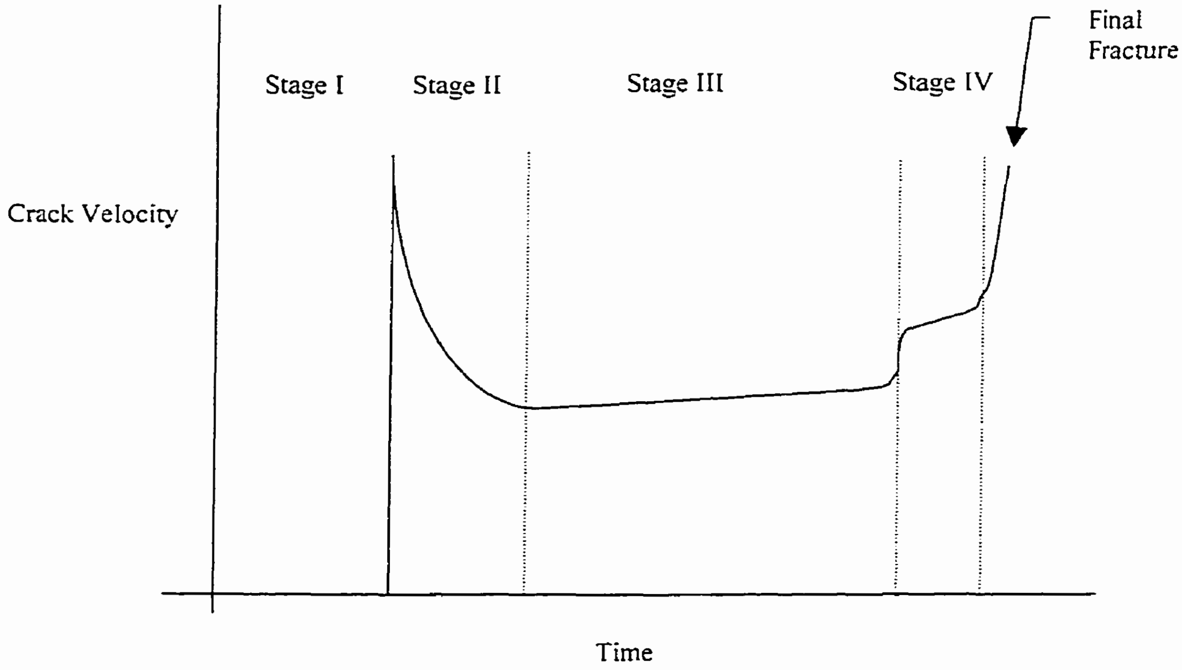

**Figure 2-1: Sequence of events for SCC as a function of time**

This sequence of events ending in fracture was proposed for pipeline failures in Australia (Baker et al., 1986) but can be applied directly to other systems. The sequence involves an initial period with no crack growth in which the SCC causing environment is developed. The development of the environment might require accumulation of specific ions, change of the pH, aeration/deaeration, breakdown of inhibitors or coatings, failure of cathodic systems, etc. The second stage is the initiation of the cracks after the SCC causing environment has been established. Stage III is a period of relatively constant crack growth rate with the growth of the cracks taking place normally by extension for most systems but can also occur by crack coalescence for other systems. Stage IV is a stage that not all systems have and is the coalescence of large cracks. The final stage has an acceleration of crack velocity until final failure occurs when the fracture occurs at velocities up to the speed of sound.

Average crack velocities during SCC failures range from $10^{-6}$ to $10^{-9}$ m/s. However, with reference to Figure 2-1, the estimation involves an assumption of the time spent in Stage I and II where the environment is established and cracks are initiated. For instance, if a pipeline has been in the ground for 10 years and a SCC crack with length of 1 mm was found, then the average crack velocity is $3.2 \times 10^{-12}$ m/s based on crack initiation occurring instantaneously (Stage I and II are assumed to occur instantaneously). If the assumption was made that it took 4 years for the environment to establish and 1 year for the crack to initiate, then the average crack velocity doubles. Obviously the assumptions made in estimating crack velocities play an important role.

## *2.4 Effect of Stress on SCC*

As mentioned earlier, tensile stress is a requirement of SCC being either externally applied or residual and can either be static or cyclic with certain restrictions. Two types of specimens are used to investigate the effect of stress on SCC in a laboratory, smooth and pre-cracked specimens. Smooth specimens are used to investigate the effect of various stress levels on SCC. In this type of test, a smooth specimen is immersed in a SCC causing environment and a load is applied. The result of the testing leads to the type of graph shown in Figure 2-2 and displays many key concepts of SCC.

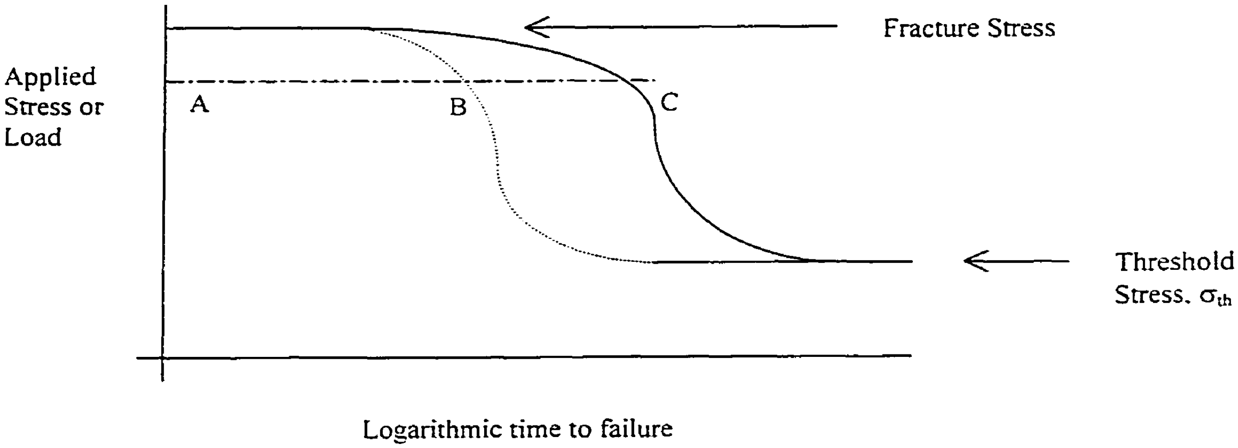

**Figure 2-2: Typical time to failure for specimens under constant load**

If a specimen is loaded at a high enough stress level, the component fails due to mechanical overload. The solid horizontal line at the highest applied stress level in Figure 2-2 represents the ultimate tensile strength (UTS) and instantaneous fracture occurs if the specimen is loaded above this level. As the stress level decreases below the UTS the component no longer fails by mechanical failure, but it does fail due to SCC. The long dashed horizontal line shows the loading "life" of a specimen loaded in a SCC causing environment. At point A, time zero, the specimen is loaded with a certain load and remains loaded with no apparent damage up to point B. At point B at the dashed line, SCC cracks initiate and begin to propagate and so the time spent between points A and B represent Stages I and II in Figure 2-1. With the load remaining on the specimen, the cracks propagate and eventually failure occurs due to SCC at point C.

Generalities can be taken from Figure 2-2 that apply to a large number of metal/environment combinations that experience SCC. At high stress levels below the failure stress, the initiation time for SCC is minimized as well as the time to failure. As the applied load is decreased, the initiation time and time to failure increases. If the applied stress is low enough, SCC will not occur. This stress is the threshold stress ($\sigma_{th}$) and is normally below the yield strength of the metal ($\sigma_{th}<\sigma_{ys}$). The fact that $\sigma_{th}<\sigma_{ys}$ is the reason that SCC is dangerous since a component that is expected not to fail since it is loaded so that the applied stress ($\sigma_{app}$) is less than $\sigma_{ys}$, may fail if $\sigma_{app}>\sigma_{th}$. $\sigma_{th}$ is often not known since it has to be determined for every metal (including various heat treatments)/environment combination and this increases the complexity for a design engineer.

The situation changes if a flaw is present in the specimen since fracture mechanics concepts must be used. For instance, if a specimen with a pre-existing crack is loaded in a SCC causing environment, the crack will propagate and stress intensity factor (K) will continue to increase. If the velocity of the crack is plotted against the stress intensity factor, a graph similar to Figure 2-3 is obtained.

There are three different stages in Figure 2-3 as the stress intensity increases. At low stress intensity levels the crack growth rate increases rapidly and constant growth occurs when the stress intensity reaches intermediate levels in stage 2. The independence of the crack growth rate in stage 2 indicates that the velocity is determined by the metal/environment combination possibly by mass transport of SCC causing species to the crack tip. As the stress intensity increases the component fails when $K_{IC}$ (or $K_C$) is reached.

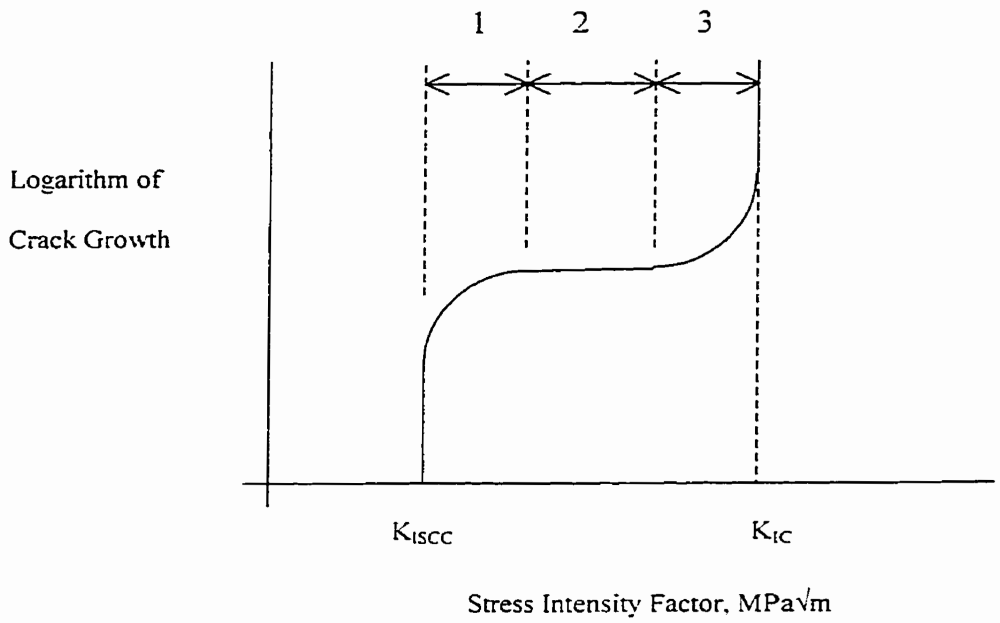

**Figure 2-3: Typical crack propagation rate versus stress intensity factor**

If the stress intensity factor is below a threshold level, designated as $K_{ISCC}$, then no propagation by SCC will occur and the specimen will not fail due to SCC. The $K_{ISCC}$ concept is equivalent to $\sigma_{th}$ discussed earlier for smooth specimens. Both of these threshold levels where SCC will not occur are dependent on the metal/environment combination. If any factor is changed such as a heat treatment, solution composition, alloy composition, environment temperature or environment velocity, a new threshold level will exist and must be determined experimentally.

### *2.5 Controlling Parameters During SCC Propagation*

Figure 2-1 shows that SCC has two regions that consume the majority of life of a component or specimen before fracture. The first region is occupied by the development of the SCC causing environment and crack initiation, that is stages I and II. The length of time spent in this region is highly variable and depends on the environment and possibly also on the breakdown of protective systems such as cathodic protection. The second region is the constant crack propagation stage III and also corresponds to stage 2 of Figure 2-3. As mention in section 2.4, the crack velocity is independent of stress and therefore is a function of the environment. Examining the controlling parameters that affect the crack velocity reveals factors that influence SCC.

In a constant velocity region in which mechanical stress does not influence crack propagation, there is a series of events that influence the growth rate that may include:

- Reactions in the solution;
- Surface reactions;
- Surface diffusion;
- Adsorption at the crack tip;
- Absorption into the metal;
- Mass transport to and from the crack tip;
- Atomic bond rupture within the metal.

Similar to all kinetic events, the slowest process in the above list will be the rate-determining step and will determine the crack velocity. When the environment changes (pH, temperature, pressure, composition, velocity, etc.) it may influence the rate determining step and in turn affect the crack velocity. As an example, an increase of the chloride concentration of a solution may lead to an increase in the breakdown of a passive film thus increasing crack velocity; or an increase in temperature might increase mass transport and increase crack velocity if mass transport was the rate-determining step. However, changes in the bulk environment are not always associated with a change in the crack velocity since the crack tip environment might be occluded from the bulk environment (also well known phenomena affecting crevice corrosion and influencing pitting corrosion).

## *2.6 Environmental Species that Influence SCC*

Early proposed theories of SCC speculated that specific ions are required to cause SCC and so it was hypothesized that pure environment (water at a pH 7) will not cause SCC. These conclusions proved to be false as the amount of research has increased in the past 50 years. Partial lists of environment/alloy combinations that cause SCC exist as a guideline basis for design (Jones, 1996). These lists are only partial since more combinations are found to be susceptible to SCC.

In actual failures, the SCC causing environment might not be initially present. Generation of the environment might require migration of a certain species to the region, generation of a species like hydroxide ($OH^-$) from cathodic systems, evaporation to concentrate the solution or bacteria to establish anaerobic conditions.

## 2.7 *Mechanisms of SCC*

Understanding the mechanisms of SCC provides insight to the variables that control the possible fracture of a structure or component. Early researchers suspected that a single mechanism could explain SCC, but as the number of environment/material combinations increased, it became clear that there was likely more than one mechanism. The main mechanisms that have received attention are presented in this section along with hydrogen embrittlement mechanisms since SCC failure can also be attributed to hydrogen damage.

### 2.7.1 Anodic Dissolution Mechanisms

Corrosion controlling the advancement the crack front was an early proposal. The advance of the crack front in an anodic dissolution mechanism will be dissolution controlled and will have a crack velocity (CV) that is related to the Faraday's relationship:

$$CV = \frac{iM}{ZF\rho}$$

where i is the anodic current density, M the atomic weight of the metal, Z the valence of the solvated species, $\rho$ is the density of the metal and F is Faraday's constant. The relationship of the crack velocity to Faraday's equation depends on the mechanism, but the maximum crack velocity on a macroscopic level is limited to the above equation.

The two major anodic dissolution mechanisms are film rupture and stress-assisted intergranular corrosion.

### a) Film Rupture

Film rupture is one of the first mechanisms to be proposed (Champion, 1948 and Logan, 1952) and also is known as slip dissolution. The film rupture mechanism is a model where stress ruptures a protective surface film, exposing bare metal to the corrosive environment and the crack front is advanced by the corrosion of the newly exposed metal, Figure 2-4. There are differing opinions on the exact cracking sequence with some researchers assuming that once propagation begins, the crack tip remains active since the rate of repassivation is not great enough to reform a protective film at the crack tip (Engle, 1971) and others assume that the crack tip repassivates and the process repeats itself with the rupture of the protective film (Staehle, 1971).

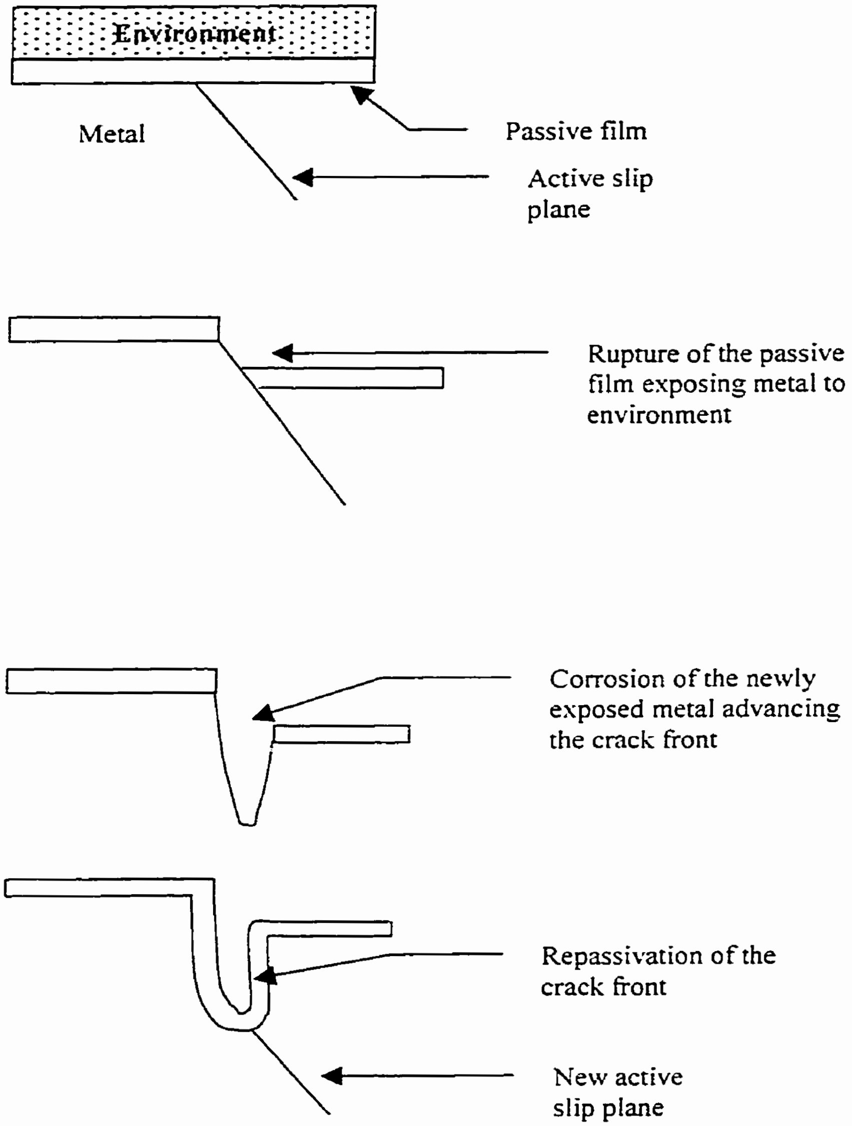

**Figure 2-4: Sequence of the film rupture mechanism**

The kinetics of the repassivation process plays an important role in the film rupture mechanism. Three kinetic situations exist: 1) repassivation is rapid and dissolution is small, 2) repassivation occurs at an intermediate rate so dissolution of the crack tip is more substantial, 3) repassivation is slow, leading to extensive lateral dissolution. In terms of this mechanism, the kinetics represented in case 2 leads to optimum cracking conditions since not enough dissolution occurs in case 1 to advance a crack front substantially and the lateral dissolution of case 3 leads to the formation of a pit rather than a crack. A detailed overview of the effect of the repassivation kinetics is given by Scully (1975). The different passivation kinetics allows the film rupture mechanism to explain intergranular fracture. If the passivation kinetics of a grain boundary is type 2 kinetics whereas the internal grain passivation kinetics is type 1, then cracking will occur along the grain boundary.

The mechanics of the film-rupture mechanism has also brought up several different variations due to criticisms. In the mechanism there is a need for repeated plastic deformation at the crack tip to rupture the film, so under a constant load the cracking process should cease. Champion addressed this issue by suggesting that dissolution needs to be fast enough to provide a stress concentration that leads to further deformation. Thus Champions (1948) version of the film rupture mechanism is a continuous process where the crack front is always advancing as an active front. However, Vermilyea (1972) indicated that room temperature creep might play an important role where plastic deformation occurs in the metal and at a critical strain the film ruptures. In Vermilyea's version of the film rupture mechanism, the dislocations do not play a direct role in the rupture of the film and the film remains intact during deformation until the film ruptures at a critical strain. Likely the emergence of slip steps from dislocations playing an important role in the film rupture mechanism occurs on thin passive films whereas the critical strain criteria is more important for thicker passive films.

The major criticism against the film rupture model is it cannot explain SCC in material/environment combinations that do not form protective films. Another criticism of the mechanism is the inability of the mechanism to explain fractographic features. Transgranular cleavage features cannot be explained by the film rupture mechanism since the anodic dissolution would obscure the cleavage face.

### b) Stress-Assisted Intergranular Corrosion

This model is often grouped with the film-induced cleavage mechanism that is described in the next section. This model requires that a brittle film forms preferentially along a grain boundary and the film ruptures due to stress. The process repeats itself and so crack propagation occurs by the rupture of the corrosion-produced film (as opposed to the rupture of the film and advancement of the crack front due to corrosion in the film rupture model). If no stress were present the film would attain a limiting depth along the grain boundary and the metal would not fail due to SCC. This mechanism is nearly identical to the film-induced cleavage mechanism presented fully in the next section, except the crack produced with film-induced cleavage is substantially propagated in the matrix and occurs transgranularly.

### 2.7.2 SCC Mechanical Fracture Mechanisms

The fore mentioned mechanisms relied on dissolution processes to advance the crack front but there is another group of mechanisms, the SCC mechanical fracture mechanisms. SCC mechanical fracture mechanisms are normal fracture processes that are enhanced by a corrosion process. The mechanism can further be divided into ductile and brittle failures with the film-induced cleavage being a brittle type mechanism and corrosion tunneling and adsorption-enhanced plasticity being ductile mechanical models.

#### a) Film-Induced Cleavage

The relationship between the formation of a film and corrosion advancing a crack front was discussed in the film rupture mechanism. Observations of some systems such as α-brass in ammonia solutions showed discontinuous cracking, where there would be a brief moment of rapid crack propagation followed by a long period where there was no propagation (Edeleanu and Forty, 1960). This type of discontinuous behaviour is not consistent with the film rupture type mechanism. In fact, many systems that show transgranular SCC exhibit cleavage planes which are also not consistent with the film rupture mechanism. It had become evident that intergranular SCC in most systems could be explained by the film rupture mechanism but a different type of mechanism was responsible for transgranular SCC that shows cleavage features.

The early work of Edeleanu and Forty and later work by Pugh (1985) and Sierdzki and Newman (1985) developed the film-induced cleavage mechanism to account for the discontinuous nature of the cracking. Cracking occurs in a repetitive three steps:

- The formation of a brittle film due to corrosion;
- Initiation of a crack in the brittle film due to stress and propagation of the crack from the brittle film into the underlying ductile matrix. This step represents the actual propagation of the crack since the crack propagates substantially into the ductile matrix.
- Crack arrest in the ductile matrix with blunting of the crack and eventually the formation of another brittle film at the crack front.

The third step in the cracking process causes the formation of crack arrest marks, which was one of the original observations that led to the film-induced cleavage mechanism, but the postulation of the cracking sequence was based on several other methods including crack-trace and acoustic emission

Although similar to the stress-assisted intergranular corrosion mechanism, the crack in the film-induced cracking mechanism propagates into the ductile matrix outside the corrosion zone whereas the stress-assisted intergranular cracking propagation halts upon reaching the ductile matrix.

### b) Adsorption Induced Cleavage or Stress Sorption Cracking

The occurrence of a failure with a particular dissolved species was an early concept of SCC. Uhlig (1959) proposed that specific anions were adsorbed onto the surface and weakened the cohesive bonds of atoms at the crack tip. The adsorption of the anions was proposed to be potential dependent to account for the decrease in SCC severity with primarily cathodic potentials. The role of inhibiting species on SCC can also be explained by this mechanism by assuming that the inhibiting species is adsorbed preferentially on the surface.

One of the key aspects in stress sorption cracking is the adsorption at mobile defect sites but these remain relatively unstudied and therefore no direct evidence has been given that there is preferential adsorption at these sites.

### c) Surface-Mobility Mechanism

Galvele's (1992) surface-mobility mechanism is an attempt to provide a single mechanism to explain all types of environmentally induced cracking from SCC to hydrogen embrittlement and liquid metal induced cracking. The mechanism proposes that stress at the crack tip causes an atom at the crack to diffuse on the surface of the crack away from the tip. The diffusion of the atom away from the crack tip introduces a vacancy and advances the crack by one atomic distance. The mechanism predicts that cracking should exist at temperatures under 0.5 times the melting point and is maximized in the presence of low melting point compounds that increase surface diffusivity.

In this mechanism the crack velocity is predicted to be:

$$CV = \frac{D_s}{L}\left[\exp\left(\frac{\sigma a^3 + \alpha E_b}{kT}\right) - 1\right]$$

where $D_s$ is the self-diffusion coefficient of the metal, L the diffusion path length, a is the atomic diameter, $\sigma$ is the stress at the crack tip, $E_b$ is the hydrogen-vacancy binding energy, $\alpha$ is a the degree of hydrogen saturation of the vacancies at the crack tip, T is the absolute temperature and k is Boltzmann's constant. Since L is approximately constant and the term inside the brackets has only a small variation, the surface self-diffusion parameter ($D_s$) is the controlling parameter. In order to accommodate all types of environments and cracking, it was proposed that the environment strongly influences $D_s$ by forming low melting compounds with the metal that maximizes the surface mobility.

The observations that Galvele used to support his mechanism have been used to criticize the mechanism. Newman and Proctor (1990) noted that the observations for the surface-mobility mechanism could be used to propose a mechanism that is based on a reduction in the surface-energy similar to some hydrogen damage mechanisms. Further observations that are not consistent with the surface-mobility mechanism is the development of surface secondary cracks away from the precrack on C-Mn steel compact-tension specimens in carbonate-bicarbonate solutions. The secondary cracks are developed due to plastic strain which is not accounted for in Galvele's mechanism. Although the surface-mobility mechanism can explain the SCC of iron in nitrates since a low melting point compound is formed, which would increase surface mobility, the mechanism fails to explain iron systems that experience SCC and form high melting point compounds such as $Fe_3O_4$.

### d) Tunnel Model

The tunnel model involves discontinuous crack propagation by both tunnel growth and ductile tearing (Pickering and Swann, 1973). The model proposes that there is an array of corrosion tunnels formed at slip steps that eventually lead to ductile fracture between the tunnels. After the tearing, the corrosion process begins again with the formation of another set of corrosion tunnels. The original concept of the model predicted grooved fracture surfaces which were not found on actual fracture surfaces, so the model was refined to the formation of flat tunnels and then upon tearing giving a flatter fracture surface that is normally associated with transgranular fracture. Although Harston and Scully (1969) have shown that the tunnel model likely applies to a stainless steel in sulfuric acid containing chlorides, the tunnel model appears to be a unique failure mechanism applicable to only a select combination of metal/environments.

### e) Localized Surface Plasticity

Anodic currents caused by corrosion have been shown to enhance creep processes (Revie and Uhlig, 1974) through softening by a surface defect structure. During a SCC cracking sequence, localized high anodic currents at the crack tip significantly soften the material in the volume behind the crack tip. With the component under stress, the softened material is constrained by the harder material outside the crack tip region and so is in a triaxial stress state. Therefore fracture occurs by brittle crack formation in the softened material. This model can explain SCC characteristics such as the high resistance of pure metals, the low resistance of high strain hardenable alloys like stainless steel and discontinuous crack growth.

### 2.7.3 Hydrogen Damage Mechanisms

Although hydrogen induced cracking and SCC are separate types of environmental induced cracking (EIC), there is an overlap between them. A failure of a stressed component due to hydrogen damage where the hydrogen was created during a corrosion process can be considered a SCC failure. Similar to SCC mechanisms, there are a variety of mechanisms that have been proposed to account for hydrogen damage.

### a) Decohesion

This model is based on dissolved hydrogen interacting with the lattice cohesive forces (Oriani, 1977). As the concentration of hydrogen increases in front of a crack tip, the hydrogen decreases the maximum point of the cohesion force/distance relationship. The decrease in this force allows a lower applied stress to exceed the cohesive force between the atoms and thus rupture the material.

The adsorption model (Petch, 1952) is similar to the decohesion model in that the hydrogen lowers the stress for rupture. In this model the adsorbed hydrogen lowers the surface energy of the metal and by Griffith's fracture criteria lowers the required applied stress for fracture. The difference between the two models is the shape of the cohesive force/distance curve. The adsorption model requires a decrease in the area under this curve whereas the decohesion model requires a decrease in the maximum force.

### b) Hydride Formation

Hydrides in metals are complex, brittle compounds consisting of hydrogen and an element of the metal. The existence of a hydride represents an easy path or initiation point for a crack (Gahr, 1977). Absorbed hydrogen migrates to the crack tip and if the concentration of hydrogen reaches a critical value the hydride will form. Due to its brittle nature, the hydride cracks and the crack propagates into the matrix and the tougher matrix arrests the crack. This sequence is repeated resulting in propagation that occurs in distinct events. Certain metals such as titanium, zirconium and magnesium can form these brittle hydrides and the hydrogen damage is attributable to the hydrides.

### c) Hydrogen-Enhanced Local Plasticity

Beachem (1972), based on fractography, first proposed that hydrogen embrittlement was associated with localized plastic deformation at the crack tip. The plastic deformation observation seemed to be in contradiction with the term embrittlement, but on the macroscopic level the failure was still brittle. Beachem suggested that hydrogen reduced the flow stress that resulted in localized deformation and failure by ductile processes. The mechanism is known as either enhanced localized plastic flow or hydrogen-enhanced local plasticity (HELP).

The application of stress to a metal in the presence of hydrogen results in a non-uniform distribution of hydrogen with a high concentration of hydrogen at the crack tip. The presence of the hydrogen has been shown to reduce the flow stress in many systems by reducing the stress for dislocation motion (Tabata and Birnbaum, 1983 and 1984). Thus, in regions of high hydrogen concentration the flow stress is decreased and slip occurs at stresses well below the normal stress required for deformation in other parts of the specimen so the deformation process is localized in the high concentration region. The specimens show embrittlement at the macroscopic level and at low-resolution of the fracture surface, but the high-resolution studies reveal plastic deformation.

The reason for enhanced dislocation mobility due to hydrogen remains unknown. This model was based on fractography and has largely been abandon since few materials exhibit this behaviour.

### d) Pressure Theory

An early model developed to explain hydrogen damage was the pressure theory (Zapffe, 1941). The pressure model developed by Zapffe was able to explain the appearance of blisters, shatter cracks, flakes and fish eyes and was based on hydrogen diffusing to certain hydrogen traps such as voids or other internal surfaces. As hydrogen accumulates at these internal surfaces, the hydrogen pressure increases and eventually expands the void it occupies or initiates a crack.

The original pressure theory postulated that as the pressure inside a void increase the fulfillment for unstable fracture would occur. Objections to the pressure theory came from Troiano (1960) who found that hydrogen embrittlement was a discontinuous process whereas the pressure theory was a continuous process. The pressure theory was then later modified (Tetelman, 1967) to account for the discontinuous process but the objections to the theory still remain and likely the theory only accounts for blistering in terms of hydrogen damage.

## *2.8 SCC of Pipelines*

External SCC of pipelines occurs when a ground water based environment comes into contact with a pipeline and when conditions are appropriate the SCC will initiate. The cracks initiate in groups called colonies and have a common orientation. Over time some of the cracks will grow in both length and depth and crack coalescence occurs (the joining of smaller cracks to create a larger crack). Eventually failure may occur resulting in leaks or rupture of the pipeline, but the slow initiation and growth of SCC cracks results in a long period between installation and failure.

There are two types of pipeline SCC. High-pH, or classical, SCC has been recognized to have occurred in the U.S. since 1965 and has had limited field observations reported (Wenk, 1974; Fessler, 1976). More recent reports have shown that classical SCC is not confined to the U.S., with an occurrence reported in Australia (Baker, 1983). A more recent type of SCC known as either low-pH, or near-neutral-pH or non-classical SCC was discovered on Canadian pipelines and several field observations were documented (Delanty and O'Beirne, 1992; Wilmott and Diakow, 1996; National Energy Board, 1996).

The two types of pipeline SCC differ in the environment, location, corrosion potential, role of temperature and crack path and morphology and is best summarized in Table 2-1.

**Table 2-1: Main characteristics of classical and non-classical SCC (based on National Energy Board, 1996)**

| Parameter | Classical | Non-classical |
|---|---|---|
| Location | Within 20 km of compressor station. | No correlation with distance from compressor station.<br>Associated with terrain. |
| Role of temperature | Increasing growth rate with increasing temperature | No relation within the tested temperatures |
| Electrolyte | Concentrated carbonate/bicarbonate solution with pH>9.3 | Dilute bicarbonate solution with pH between 6 and 6.8 |
| Cracking Potential | -530 to –680 $mV_{SCE}$ | -690 to –720 $mV_{SCE}$ |
| Cathodic Protection | Requires cathodic protection to attain cracking potential | Region does not receive cathodic protection |
| Cracking | Intergranular<br>Narrow cracks with limited corrosion | Transgranular<br>Wide cracks with substantial crack wall corrosion |

The following are the various factors that affect pipeline SCC. Each section presents the related field observations (all observations for non-classical SCC are from eithier Delanty and O'Beirne (1992) or Wilmott and Diakow (1996) and the classical SCC observations are referenced from either Wenk (1974) or Fessler (1976)) and then each section reviews the knowledge gained through laboratory experimentation.

### 2.8.1 Environment

Field Observations

Original attempts to classify the soils surrounding classical SCC failures used colour, texture and it was found that classical SCC can occur in a variety of soils. Even when the features were expanded, no single characteristic was common to all the soil samples. Characterizing the soils by soaking them in water and analyzing the water also showed that there was no common chemical composition to the soil.

In several different classical failures, liquids found in disbonded regions were found to contain principally carbonate ($CO_3^{2-}$) and bicarbonate ($HCO_3^-$) with pH's varying from 9.6 to 12.3. Other ions that could also be found in very small quantities were chlorides ($Cl^-$), nitrates ($NO_3^-$) and hydroxides ($OH^-$). In addition to the ions, sodium bicoarbonate ($NaHCO_3$) crystals were also found to have precipitated out near the crack surface.

Analysis of the electrolytes taken from directly above non-classical SCC colonies has determined that they were all dilute, low pH solutions. The solution consists mainly of $HCO_3^-$ with some carbonic acid ($H_2CO_3$) and limited amounts of $CO_3^{2-}$ and $Cl^-$. Table 2-2 lists the average composition of the classical and non-classical environments. The difference between the environments is not only in terms of the pH due to differing amounts of $H_2CO_3$-$HCO_3$-$CO_3^{2-}$, but the concentration of each type of ion is much greater for the classical environment.

**Table 2-2: Average weight percent of solutions found under coatings in the region of SCC (based on Delanty and O'Beirne, 1992)**

| Species | Classical | Non-classical |
|---|---|---|
| $H_2CO_3$ | NA | 0.04 |
| $HCO_3^-$ | 0.47 | 0.15 |
| $CO_3^{-2}$ | 0.83 | 0.00002 |
| H (in terms of pH) | 10.3 | 7.1 |
| $Cl^-$ | 0.063 | 0.0024 |
| $NO_3^-$ | 0.0037 | 0.000005 |

Sampling of the soil gas in non-classical failures revealed a varying composition with respect to the time of year. The gas composition changed from 5% carbon dioxide ($CO_2$) in the summer to 24% in winter and this variation affects the groundwater composition as well. The increasing amount of carbon dioxide the $H_2CO_3$ and $HCO_3^-$ levels was found to increase with a corresponding drop in the pH to 6.8 from 7.6 in the summer. The seasonal variation of the composition related to the three original failures on the Transcanada Pipeline system that occurred in the fall and winter months suggesting that SCC propagates in only the lower pH environment.

Iron and steel normally have low corrosion rates in deaerated water but the presence of bacteria can increase the corrosion rate by depolarizing the cathodic reaction. Sampling of bacteria from non-classical SCC sites showed that as the severity of the SCC increased, so did the concentration of sulfate reducing and acid-producing bacteria.

## Experimental Results

The environment that is known to cause external pipeline SCC is a carbonate system ($H_2O$-$H_2CO_3$-$HCO_3^-$-$CO_3^=$) and other ions. To understand either type of pipeline SCC it is useful to understand the carbonate system and how additional ions affect the equilibrium and also the solubility of various substances. When carbon dioxide is brought into contact with water, the water absorbs the carbon dioxide and converts a portion of this to carbonic acid. Normally the dissolution of the carbon dioxide is not represented as a separate step in thermodynamic analysis and the dissolution is represented as a direct formation of carbonic acid:

$$CO_{2(g)} + H_2O \leftrightarrow H_2CO_3$$

The carbonic acid dissociates into the bicarbonate ion and the bicarbonate ion dissociates to form the carbonate ion:

$$H_2CO_3 \leftrightarrow H^+ + HCO_3^-$$

$$HCO_3^- \leftrightarrow H^+ + CO_3^{-2}$$

The equilibrium constants for these three reactions that describe the carbonate system are:

$$K_{CO_2} = \frac{a_{H_2CO_3}}{P_{CO_2}} = 10^{-1.47}$$

$$K_1 = \frac{a_{H^+} \cdot a_{HCO_3^-}}{a_{H_2CO_3}} = 10^{-6.35}$$

$$K_2 = \frac{a_{H^+} \cdot a_{CO_3^{-2}}}{a_{HCO_3^-}} = 10^{-10.33}$$

Experimental work on non-classical SCC sometimes uses a simulated groundwater solution called NS4 with composition shown in Table 2-3 with a 5% $CO_2$/ 95% $N_2$ purge gas.

**Table 2-3: Solution composition of NS4, a simulated groundwater**

| Substance | (g/L) |
|---|---|
| KCl | 0.122 |
| $NaHCO_3$ | 0.483 |
| $CaCl_2 \cdot 2H_2O$ | 0.181 |
| $MgSO_4 \cdot 7H_2O$ | 0.131 |

Simplifying this environment to include only the purge gas and the sodium bicarbonate, an evaluation of the system equilibrium at 25°C gives a pH=6.23 which agrees well (considering the assumption that concentration equals activity) with the field observations of pH values for non-classical SCC.

The corrosive behaviour of carbon dioxide solutions is well documented with carbon dioxide solutions having higher corrosion rates than a solution of the same pH containing no carbon dioxide. A detailed electrochemical investigation of aqueous carbon dioxide solutions (Nesic et al., 1996) showed that in solutions above pH 5, the major cathodic reduction reaction is:

$$H_2CO_3 + e^- \rightarrow H + HCO_3^-$$

with reduction of $H^+$ being a secondary cathodic reaction.

There is only a slight difference in the SCC performance when minor variations are made to the non-classical environment (Parkins et al., 1994). The variations of the NS4 environment were made by altering the concentration of KCl, $NaHCO_3$, $CaCl_2 \cdot 2H_2O$ and $MgSO_4 \cdot 7H_2O$ (environments named NS1, NS2, and NS3) and also using or not using a $CO_2$ purge gas. There was no effect on the SCC characteristics between the various NS environments, but there was a difference based on the type of purge gas. A schematic showing the effect of the various environments is shown in Figure 2-5 with the ratio $RA_{SCC}/RA_{Air}$ a measure of the severity of the SCC (the lower this ratio the more the severe the SCC) and the blocked region for each pH indicating the range of failure ratios obtained over a range of potential. The environment with a pH=8.2 in the various solutions with no $CO_2$ purge gas, pH=5.8 is a full $CO_2$ purge and pH=6.4 is a

$CO_2/N_2$ purge gas. The environment with the lowest pH had the most severe SCC at most potentials.

The effect of the purge gas has to do with the pH control of the solution where a lower pH environment can evolve more hydrogen and decreases the ductility of the steel. The effect of potential is discussed in a later section.

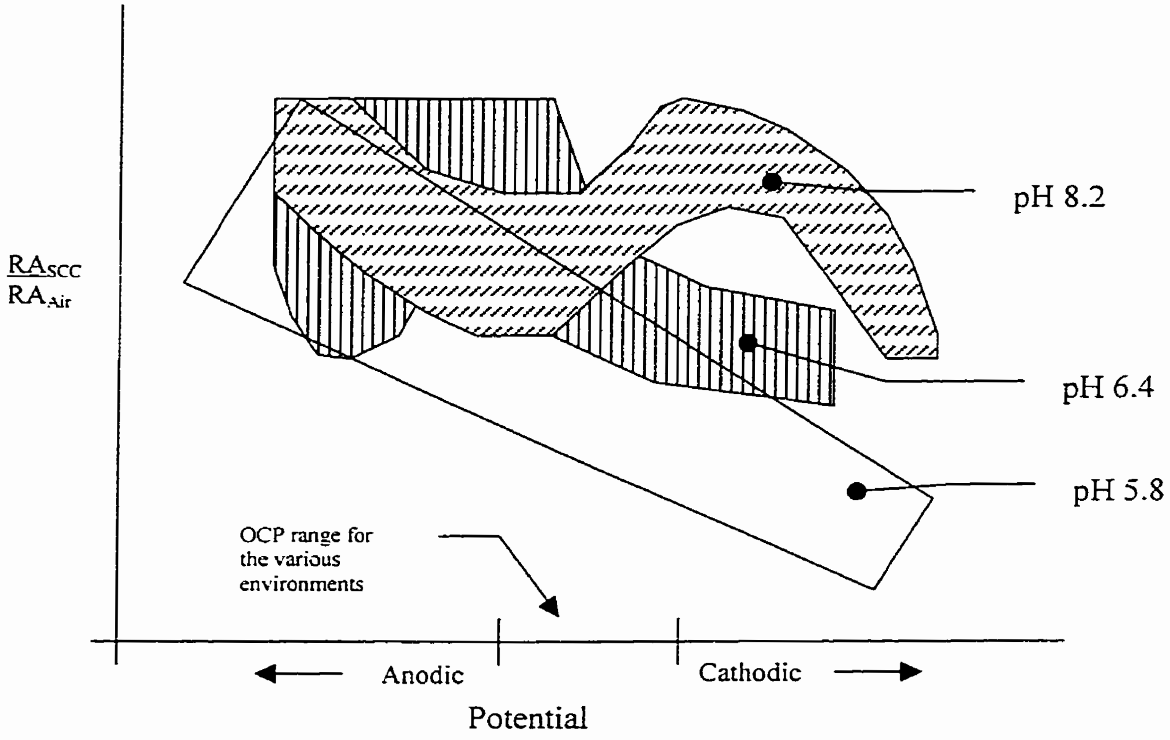

**Figure 2-5: Schematic of the non-classical SCC characteristics of X-65 pipeline steel in different environments (based on Parkins et al., 1994)**

### 2.8.2 Temperature Effect

Field Observations

Most occurrences of classical SCC have been near the discharge side of a compressor station with 65% being within 8 km and >90% being within 16 km of the compressor station. This proximity to the compressor station is likely related to the high temperatures created during the compression of the gas. The temperatures estimated at the failure sites range from 13°C to 58°C with most being around 35°C.

Failures due to non-classical SCC do not show the same dependency with temperature. Non-classical failures have been detected near the outlet of a compressor station and as far away as 67 km from the station. There does not appear to exist a relationship between non-classical SCC and temperature.

Experimental Results

Parkins et al. (1994) conducted slow strain rate tests, SSRT, on X-65 linepipe in various solutions that simulated ground water at pH 6.4 and 5.8. The results show that non-classical SCC does not have a temperature relationship since the failure ratios at various temperatures overlapped one another. This held true when the potential at which the SSRTs were conducted was varied from approximately $-550\ mV_{SCE}$ to $-800\ mV_{SCE}$.

### 2.8.3 Corrosion and Cracking Potential

Field Observations

The actual potential of a pipeline that experienced a SCC failure is difficult to determine. The soil-to-pipe measurements cannot be considered representative of processes that are occurring underneath a coating since there would be an associated potential drop across the coating. The potential can be somewhat inferred by the environment and state of the pipeline surface. Conversely, the non-classical environment requires no cathodic protection implying that the pipeline is at the open circuit potential or the free corrosion potential. Indeed observations of the pipe surface also suggest that the pipeline is at the free corrosion potential since cracking is associated with substantial corrosion. For classical SCC, the pipe surface shows little corrosion indicating that the potentials might be cathodic.

Experimental Results

Early work by Sutcliffe et al. (1972) indicated that there was a narrow potential range where classical SCC could occur. Linepipe steel in a concentrated carbonate/bicarbonate solution displays an active/passive behaviour and the cracking potential could be determined by performing slow and fast potentiodynamic scans and comparing the scans to SCC testing results. The results indicated that severe SCC occurred when there were large differences in the current of the two scan rates and that this occurred at approximately $-675\ mV_{SCE}$.

Parkins et al. (1994) investigated the effect of potential on non-classical SCC in various environments. Figure 2-5 showed the relative SCC susceptibility characteristics of X-65 steel in various environments. For pH=8.2 there are two peaks, one at ~-0.5 $V_{SCE}$ and the other at ~-0.8 $V_{SCE}$, that show increased resistance to SCC. At this pH the open circuit potential (OCP) was ~-0.72 $V_{SCE}$ so the expected reason for a decrease in the resistance as the potential first became anodic was due to an increase in pitting that increases the initiation sites for SCC. As the potential became more anodic the SCC resistance increased as the corrosion process turned into general corrosion due to the high corrosion rates. Conversely, as the potential first became cathodic there was an increase in the SCC resistance due to a decrease in the pitting and general corrosion. As the potential becomes more cathodic there was an increase in the rate of hydrogen generation, resulting in a sharp decrease in the SCC resistance at the lowest potential. The same general trend occurred for the environment at pH=6.4 except that the failure ratios were lower indicating more severe SCC and the potentials were more noble. The final environment at pH=5.8 showed a distinctly different effect of potential on SCC resistance with the resistance decreasing with decreasing potential. The greater corrosion rate and hydrogen generation in this environment was noted as the reason for this trend.

Beavers et al. (1993) found that the free corrosion potential was sensitive to surface finish for the concentrated carbonate/bicarbonate environment. They found that at 25°C a X-52 linepipe with a mill-scale surface had a free corrosion potential between –400 and –500 $mV_{CCS}$ and a grit blasted surface had a potential of –900 $mV_{CCS}$. Normal cathodic protection for pipelines uses a surface potential minimum of –850 $mV_{CCS}$ and classical SCC has a cracking potential of –722 $mV_{CCS}$. This reveals that if a mill scale surface of a pipeline is exposed through a holiday and begins to be cathodic protected from approximately –450 $mV_{CCS}$ to –850 $mV_{CCS}$ it will pass through the SCC cracking potential in the classical environment. However, a grit blasted surface would not pass through the cracking potential and should be immune to classical SCC.

### 2.8.4 Crack Morphology

Field Observations

Classical SCC cracks were found to exist in disbonded areas under coatings that contained small pinholes. The cracks were found to occur in groups with smaller cracks coalescing to form larger cracks. The intergranular cracks of classical SCC are narrow and fine with a black deposit on the crack walls that is the magnetic iron oxide, $Fe_3O_4$, and there is also minor amounts of iron carbonate ($FeCO_3$).

Non-classical SCC cracks are found in colonies that consist of numerous cracks with spacing between the cracks of less than 1mm. The small cracks can coalesce to form larger cracks similar to what was found for classical SCC. The process of coalescence is similar for both types of SCC with the tips of cracks passing one another before turning and growing towards one another. Field measurements of the non-classical crack length to the spatial separation of the cracks show that coalescence may occur if the crack separation is $< 0.14(2a)$ where 2a is the length of the crack. Cracks tend to grow with an aspect ratio (surface length to depth) much greater than unity meaning the cracks tend to elongate rather than grow through thickness.

Non-classical SCC has a transgranular path and there is substantial corrosion of the crack walls. The dissolution of the crack walls can make the process of identifying the transgranular nature difficult since the crack walls can be corroded beyond the grain size, so the transgranular nature of the cracking is normally only identified near the crack tip. The effect of corrosion is also found in depth of the crack when a bulbous cavern is found that is the result of preferential corrosion. Normally large amounts of $FeCO_3$ are found between the pipe surface and the coating.

## Experimental Results

Experimental procedures used to simulate and investigate parameters of SCC normally depend on examining the crack morphology in order to confirm that the proper type of SCC has occurred. Once the occurrence of SCC has been confirmed, further analysis of the crack morphology and the fracture surface can be performed to increase the knowledge of the mechanism and parameters.

Crack coalescence in the laboratory is readily producible by cyclic loadings (Parkins et al., 1994). Cyclic loading of X-65 linepipe steel in the non-classical environment produced bands of cracks and coalescence occurred if crack separation was < 0.156(2a). The appearance of bands of cracks led the researchers to believe that the generation of new cracks occurs at the ends of previously existing cracks due to hydrogen accumulation at the ends of the cracks.

Further analysis of the cracks showed that the cracking was transgranular with corrosion of the crack walls. Both these experimental results and also that the spatial correlation of the crack coalescence parameter was near that observed in the field, confirmed that these researchers had reproduced failures that were similar to those experienced in the field.

An analysis of the fracture surface indicated that a defining characteristic of non-classical SCC is the occurrence of quasi-cleavage facets and the severity of the SCC is displayed by the amount of microvoid coalescence (MVC) and quasi-cleavage. Situations that exhibited severe SCC showed a high percentage of quasi-cleavage where as mild SCC showed substantial amounts of MVC. The crack path through the fracture surface showed a region of well-defined fracture features at the front of the crack and substantial corrosion along the remaining surface back to the edge of the specimen due to corrosion of the crack walls.

### 2.8.5 Role of Coatings

Field Observations

Field observations for pipeline SCC have shown that coatings play a vital role. Classical SCC cracking was associated with small invisible pinholes in the coatings that lead to a region adjacent to the pipe surface where the coating had disbonded from the pipe. It is believed that the pinhole allows the ground water and small amount of cathodic current to enter the disbonded region and prevents the escape of the alkaline water. The role of the pinhole is consistent with further observations that large holes were not associated with SCC cracking.

Field observations for non-classical SCC found that the majority (~70%) of the SCC occurs on polyethylene (PE) tape coated pipeline and the remaining occurs on asphalt coated lines. Not only is the propensity of SCC greater on taped lines, but also the severity of the SCC is also greater. For taped lines, the average number of SCC colonies detected at sites where SCC was found was almost twice the number detected at the asphalt coated sites with SCC and the depth of the cracks was greater at the tape coated sites. In the case of tape-coated failures, the tape was found to still be intact, but disbonded from the pipe, creating a sheltered region. The influence of the disbondment is best demonstrated by an example where tape coating was wrinkled due to an external stress and created long narrow disbonded regions. Within these regions, long narrow colonies of cracks formed that were predominantly aligned head to tail which links crack initiation and growth to coating disbondment. Typically on excavations of asphalt coated lines, the asphalt tended to be in generally good condition with little disbondment.

It is difficult to determine the role of fusion bonded epoxy (FBE) coatings in the SCC of pipelines due to their relatively short time that they have been used in the field. FBE coatings have had limited service time compared with asphalt or tape coatings and to declare FBE coated pipelines immune to SCC could be premature. Field observations showed that although asphalt coatings were far less likely to contain non-classical SCC sites and the severity of the SCC tended to be less, an asphalt coated pipeline placed in service in 1958 contained SCC that penetrated 22% of the wall thickness (severe). This shows the time dependence of non-classical SCC.

## Experimental Results

Pipelines use a combination of coatings and cathodic protection to provide external corrosion protection. The coating is the first defense for corrosion by providing high electrical resistance and thus impeding current flow. However, coatings can be damaged by soil stress or cathodic disbondment or contain imperfections known as holidays. In cases where the coating no longer provides protection, the cathodic protection system provides corrosion protection by maintaining the pipeline at a prescribed potential. Unfortunately coating damage does not always occur in such a manner where a low resistance path is created that provides adequate cathodic protection.

There are three types of coatings that are or were in common use: asphalt, PE tape and FBE. These products represent different stages of development of coatings with asphalt coatings being applied in the 1950's and 60's, taped coatings in the 60's, 70's and 80's and FBE or extruded polyethylene in the 80's and 90's. The influence of the taping process was believed to play an important role in near neutral SCC by creating a "tented" region adjacent to a weld as shown in Figure 2-6.

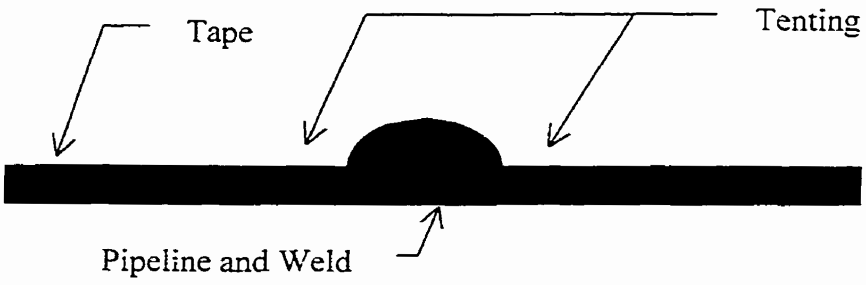

**Figure 2-6: Schematic of tenting caused by weld bead**

Tenting can also occur without the weld bead and this occurs during the successive wrapping of tape. Tape is applied by spirally wrapping the pipeline and the windings overlap one another to assure full coverage. This overlap forms a helical tent as described by Sutherby (1998).

The electrical properties of coatings play an important role in cathodic protection. Wilmott et al. (1998) investigated the role of the coatings in providing cathodic protection. Their investigation utilized a two-chambered testing cell that was separated by one of the coatings above. Using an initially porous membrane they found that the pH of the anode section decreased while it increases in the cathode chamber when a cathodic current was applied. This was expected as a cathodic hydrogen reduction reaction and anodic hydrogen oxidation reaction would alter pH. In place of the porous membrane, asphalt coating from the field, FBE and PE tape were used. The results showed that the asphalt allowed a greater amount of current to pass as the test proceeded, the FBE passed an increasing, yet small, current and the PE tape passes no measurable current. The passing of cathodic current in the asphalt and FBE cases caused the pH to increase in the cathode chamber.

Coating failures occur in four different types. Missing coatings (holidays) or shielding disbondment (tenting either by weld seams, helical tenting or some other form) were already discussed above. The two other forms are permeability increase that occurs with asphalt coatings and blistering as seen with FBE coatings. The relationship between cathodic current, coating, coating damage, corrosion and SCC is summarized in the following table:

**Table 2-4: Relationship between Coating Failure Mode and SCC** (based on Wilmott et al., 1998)

| Failure Mode | Coating Type | Does CP reach steel? | Corrosion | SCC |
|---|---|---|---|---|
| Missing Coating | all | Yes | Negligible | No |
| Shielding Disbondment | tape | No | Mild to severe | Near neutral pH |
| Permeable | Aged asphalt | Yes | Negligible to moderate | High pH SCC |
| Blisters, Pinholes | FBE | possible | Negligible | Not found |

The findings of the Wilmott et al. (1998) agree with earlier results (Beavers et al., 1993). Beavers et al. measured pore resistance in the high carbonate/bicarbonate solution and 3% NaCl solution and found that the tape coatings maintained high resistance whereas the FBE and a coal tar coating had decreasing resistance with testing time. Beavers et al. performed further testing on coating disbondment using the three different types of coatings and modified ASTM G-8 and G-42 standards. They found that tape coatings would readily disbond compared with the FBE and coal tar coatings; however, FBE coating disbondment was sensitive to the surface preparation with a mill-scale or corroded surface showing much higher disbondment whereas coal tar was relatively insensitive to surface finish.

SCC tests by Beavers et al. (1993) for classical SCC showed that SCC susceptibility is indeed related to the type of coating when the coating was degraded. Coatings with a small holiday were degraded by cathodic polarization and then a cyclic stress was applied with the specimen then polarized to the cracking potential. Results showed that tape would disbond and show extensive cracking as compared to the coal tar and FBE coatings.

### 2.8.6 Cathodic Protection

Field Observations

The correlation of non-classical SCC and pH is strong, based on over a thousand pH samples in disbonded regions and hundreds of pH samples above SCC colonies. The field observations clearly show that near-neutral-pH SCC occurs when the pH<7.5. This is significant since it implies that the region is getting less than 100 mV of cathodic protection (further discussed in the experimental results).

The soil type surrounding non-classical SCC also shows a relationship to cathodic protection. The majority of the failures associated with asphalt coatings occur in highly resistive soils. The implication is that the high soil resistance allows almost no cathodic protection to reach the pipeline.

Experimental Results

Cathodic protection plays a vital role in the generation of the cracking environments for both classical and non-classical SCC. Typical groundwater concentrations are normally near neutral and relatively dilute in terms of ions. The development of the classical SCC environment therefore requires an increase in the pH and a method of concentrating the ions. A combination of temperature and cathodic protection can produce this environment (Charles and Parkins, 1995).

Charles and Parkins investigated the role of cathodic protection in turning a $H_2CO_3$-$HCO_3^-$ groundwater (NS4 solution, the simulated groundwater that causes non-classical SCC) to a $HCO_3^-$-$CO_3^{-2}$ containing groundwater that causes classical SCC. Beginning with the NS4 solution, they found that with the application of cathodic current and closing the system (no additional $CO_2$ is provided) causes a rise in the pH from <6 to normally >9 with the pH remaining at 6.5 and 9.5 for long periods. The rise in pH was dependent on the initial pH and on the magnitude of the cathodic current with high cathodic currents decreasing the time required in converting to a high pH environment. Rather than using a closed system, if $CO_2$ is continuously provided the pH stabilized to a value dependent on the partial pressure of $CO_2$ and the applied cathodic potential.

The stabilization of the system around pH 6.5 and 9.5 was not surprising since the carbonate system is a buffer solution depending on the existence of $H_2CO_3$-$HCO_3^-$ or $HCO_3^-$-$CO_3^{-2}$ combinations. The carbonate system has a buffering range of pH=5.38 to 7.38 when $H_2CO_3$-$HCO_3^-$ exist and a buffering range of pH=9.32 to 11.32 when the solution is primarily $HCO_3^-$-$CO_3^{-2}$.

The role of cathodic protection in generating SCC conditions was thus:

- As long there is ample $CO_2$ and minimal cathodic protection, the NS4 maintains a pH of ~6.5 due to the buffering action of $H_2CO_3$-$HCO_3^-$.
- If there is sufficient generation of the hydroxide ion ($OH^-$) due to cathodic protection, the available $CO_2$ is consumed and there is a shift in the solution pH from 6.5 to ~9.5 due to a conversion to a $HCO_3^-$-$CO_3^{-2}$ system. The pH stabilizes at ~9.5 due to the buffering action of $HCO_3^-$-$CO_3^{-2}$.

The generation of the high pH is not a sufficient parameter for a classical SCC environment since Table 2-2 showed that there needs to be a concentration of the ionic species. Charles and Parkins (1995) showed that by raising the temperature of the NS4 solution and by applying a cathodic current, not only is a high pH solution created but a higher ionic solution is created due to increased evaporation. They assert that this might be an additional role of temperature in classical SCC and why classical SCC occurs near the discharge of compressor stations.

### 2.8.7 Applied Stress

Field Observations

Classical SCC service failures have occurred at stresses that range from 46 to 76 percent of specified minimum yield strength (SMYS). These were based on Barlow's formula and the original wall thickness.

Non-classical SCC shows a slightly different relationship with stress. There has been a large range of operating stresses that have caused SCC failures ranging from 70% to 20% of SMYS. Calculations based on the operating stress and crack dimensions give the stress intensity range between 9 to 21 MPa√m with an average of 15 MPa√m. The growth rates of the cracks within a colony have possibly two different growth rates. Surface growth of cracks extends the size of the crack along the axis of the pipe and field measurements averaged either $7.4 \times 10^{-9}$ mm/s or $9.4 \times 10^{-9}$ mm/s depending on the assumption of when cracking on the pipeline began (either immediately after installation or five years after installation). Surface growth rate for the longest crack of each colony was $1.05 \times 10^{-8}$ mm/s using the 5-year assumption. Growth of the crack through the wall thickness for the deepest crack of each colony was $1.68 \times 10^{-9}$ mm/s based on the assumption that the crack started 5 years after installation. The magnitude difference between the surface and depth growth rates exemplifies the effect of crack coalescence.

The effect of surface condition is difficult to determine in field observations. However, some non-classical SCC failures have been associated with deep scratches or occurring at the toe of a longitudinal seam weld.

## Experimental

Stress in a pipeline is either residual or applied. Residual stress occurs during the production and installation of the pipeline. Applied stress results from the gas pressure and earth movements in the form of localized shifting of the soil adjacent to the pipeline. The internal pressure causes hoop the given by Barlow's equation:

$$\sigma = {}^{PR}\!/_{t}$$

where $\sigma$ is the stress, P the pressure, R the radius and t the wall thickness.

Focusing on the operating pressure, the pressure generated from a compressor station has generally a mean component with an additional alternating component. These operating pressures thus impose a mean stress and a cyclic stress component on the pipeline and the role of the mean or cyclic component of the applied stress has been the subject of many investigations.

Wilmott and Sutherby (1998) investigated the role of the mean stress in propagating small shallow cracks, which represents propagation early in the non-classical SCC life cycle. Their experimental procedure stressed coupons to a maximum 40%, 70% and 100% SMYS with a cyclic component that gave a stress ratio (R) R=0.98. There was no correlation between the maximum applied stress and the average growth rate as well as the percentage of propagating cracks on each coupon. The investigation also found that the distribution of the crack growth rates for all the propagating cracks were nearly identical for the three stress levels. Thus for small shallow cracks there is no influence of load on the crack growth rate or number of propagating cracks.

Zhang et al. (1999) using a test method similar to Wilmott and Sutherby found that crack growth rate for non-classical SCC was not a function maximum stress intensity factor ($K_{max}$) and that crack velocity was not a function of frequency for a given $K_{max}$. However, they found that crack velocity was a function of the difference between the minimum and maximum stress intensity factor ($\Delta K$) and was also a function of frequency when $\Delta K$ parameter was used. Their conclusion was that higher crack growth rates were observed at lower frequencies for a given $\Delta K$ because of a longer exposure time to the environment for each cycle.

Parkins et al. (1994) found that crack growth rates were not a function of frequency for non-classical SCC, which also agrees with Beavers et al. (1998). Parkins et al. (1994) also found that the average crack velocity and the density of cracks increased with maximum stress. Parkins et al. (1994) results of crack velocity increasing with either an increasing maximum stress or maximum $K_I$ seem contradictory to Wilmott and Sutherby (1998) and Zhang et al. (1999) who found no such correlation.

From the above presentation of research, it is difficult to determine the influence of cyclic stress on non-classical SCC. The evidence regarding the relationship between frequency and $K_{max}$ with crack velocity is contradictory. It is also interesting that the role of frequency was a function of which parameter was used as shown by Zhang et al. (1999) with crack velocity being a function of frequency for a given $\Delta K$ but not a given $K_{max}$. The role of dynamic straining is somewhat more in question since Zhang et al. (1999) found propagation occurred under static loading. Zhang et al. also found crack propagation in static loaded precracked specimens whereas Beavers et al (1998) found limited propagation. The contradictory results of the role of dynamic straining indicate that it requires further investigation.

The role of cyclic stress in classical SCC has also been investigated extensively. Pilkey et al. (1995) applied cyclic loads at different frequencies using a cantilever style loading frame on notched X-60 line pipe steel held at –650 $mV_{SCE}$ in 1 N $Na_2CO_3$ + 1 N $NaHCO_3$. The results showed that there are two stages of crack growth based on the crack growth rate and $K_{max}$. The first stage is where there is a rapid increase in growth rate when $K_{ISCC}$ (determined to be 25 MPa√m) is exceeded and the second stage is where the increase in crack growth rate decreases with increasing $K_{max}$. The second stage growth showed a modest increase in the crack growth rate leading the investigators to suggest that there was an upper bound to the growth rate, which supports the film rupture mechanism for classical SCC. However, the upper bound conclusion appeared to be based on a limited amount of data.

Cyclic stress has been shown to be deleterious to classical SCC by Parkins et al. (1993). Cyclic loading caused a decrease in the threshold stress for a variety of different steels in a concentrated carbonate/bicarbonate solution. The effect of stress magnitude was also investigated. It was found that higher stresses nucleate more cracks in shorter time periods compared to stressing the specimens just above the threshold stress. Finally the nucleation of cracks and the growth rate of the largest cracks were found to increase with increasing exposure time.

### 2.8.8 Microstructural Aspects

#### Field Observations

The majority (~95%) of non-classical failure occurs within the body of the pipe with a small percentage of the failures occurring along the weld bead. Microstructural correlations of field failures concerning initiation is difficult due to mill scale and due to the fact that the chances of finding SCC in the early initiation stage is remote.

#### Experimental

Environmental induced cracking is a multistage process that goes from generation of the environment to initiation of the cracks and finally to crack propagation until failure. Depending on the system, one of these stages can be the rate limiting process and in the case of near-neutral-pH SCC, it appears that either the generation of the environment or the initiation of the cracks is the rate limiting process.

Wang et al. (1998) investigated the role of initiation of near-neutral SCC and related crack initiation to microstructure features. The testing procedure utilized a four point bending system to apply a cyclic stress to X-65 linepipe steel in a NS4 solution. They found that there was macroscopically general corrosion and pitting was found to correlate with mainly aluminate inclusions that may contain substantial amounts of calcium and sulphur. The composition of the inclusion played a role in the morphology of the pit with a low sulphur pit having the corrosion attack focused on the base metal around the pit and as the sulphur content of the inclusion increased, there was more dissolution of the inclusion. Also, a "halo" was found around the pits which was less corroded than the rest of the surface and the diameter of the less corroded area was a function of the central pit diameter as shown in the following schematic:

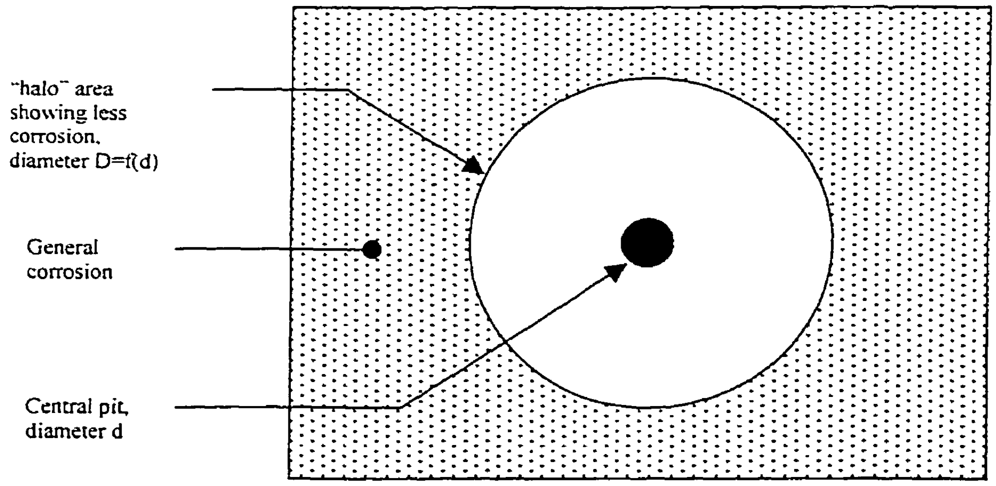

**Figure 2-7: Schematic of the "halo" region as described by Wang et al. (1998)**

If several inclusions were aligned close enough together, the "halo" area would reflect this distribution by becoming more elongated. The investigators attribute this "halo" region to galvanic effects.

Wang et al. identified two types of cracks in their investigation:

Type I: "Pit cracks" are initiated from a pit and were scattered throughout the specimen being separated normally by 100 times the average crack length and are associated with non-metallic inclusions. These cracks form before type II cracks and cracks that form early grow in size and normally become dormant. Type I crack that form latter in the crack initiation stage normally continue to grow and become the dominant cracks.

Type II: "Non-pit crack" are initiated not at a pit and the average distance between the cracks is less than the average crack length. Non-pit cracks were found to initiated at the boundary of tape coatings, around the edge of the "halo" region, at micro-hardness indentations that simulate surface discontinuities and possibly along certain crystallographic planes. A substantial amount of exposure is required to form these cracks.

The fact that inclusions play an important role in crack initiation is significant but as the investigators point out, eliminating inclusions will not make the steel immune to SCC since type II cracks exist.

Other microstructural aspects for non-classical SCC were observed by Parkins et al. (1994). They noted that secondary cracks not connected to the outer surface of the specimen were usually nucleated on bands of pearlitic material. Also Zhang et al. (1999) found that MnS influenced crack propagation either producing bifurcation or halting of a propagating cracks. The influence of MnS on the fracture surface was also observed to produce more cleavage like fracture adjacent to the inclusion prompting Zhang et al. to stress the importance of MnS as a hydrogen trap. The final microstructural aspect for non-classical SCC was reported by Beavers et al. (1998). They observed that a coarse grain heat affected zone (CGHAZ) microstructure of X-65 linepipe steel sustained greater crack velocity than the as-received microstructure. The result is intriguing but they failed to indicate what the CGHAZ microstructure was and heat input in a welding process will greatly vary the resulting microstructures.

### 2.8.9 Mechanisms of Pipeline SCC

Wang et al. (1998) have proposed a mechanism for non-classical SCC where cyclic loading and hydrogen-induced plasticity promotes localized plasticity. This exposes slip planes to the environment that are preferentially corroded and advance the crack front. They proposed this mechanism based on fractography and corrosion surfaces features.

These investigators found facets on general corrosion surfaces, corrosion pit bottoms and crack walls that were substantially corroded during SCC testing. This feature was neither dependant on stressing condition nor the acidity of the NS4 solution and hence is a dissolution feature in this general environment. The facets are due to preferential corrosion along certain crystallographic planes.

The aspect of localized plasticity in their mechanism is based on crack initiation of both crack types, I and II. They found that a certain number of load cycles were required to initiate non-pit cracks and that pit-cracks initiated after a period of loading after the pit was formed. These observations lead the investigators to believe that a period of micro-deformation occurs where an accumulation of deformation along slip planes produces slip that expose slip planes to the environment. As discussed above, these newly exposed slip planes are preferentially corroded and this is the process of crack advance.

Wang et al. further supported the plasticity aspect by referring to three factors. First, researchers found in the past that a constant load does not cause near-neutral-pH SCC and there is a requirement of dynamic stressing. Cyclic loading promotes plasticity at stresses below those for monotonic loading and so under cyclic loading, deformation occurs and accumulates along slip planes at low stress levels. Second, surface discontinuities such as pits or crystallographic planes act as local stress raisers and promote localized plasticity and this demonstrates why corrosion pits initiate cracks before non-pit cracks form. Finally, corrosion in the NS4 environment produces hydrogen that can promote localized plasticity. The localized plasticity factor of this mechanism also introduces a concept that agrees with earlier results. Researchers have not been able to identify a threshold stress for near-neutral-pH SCC and Wang et al. propose that possibly a minimum strain requirement is more plausible.

Gu et al. (1999) proposed a second mechanism for non-classical SCC that is also an anodic type mechanism. The mechanism is titled Hydrogen-Facilitated Anodic Dissolution and is based on hydrogen and other factors greatly increasing the dissolution rate of the crack tip. Their mechanism is based on Faraday's law where crack velocity (CV) is:

$$\mathrm{CV} = \frac{\mathrm{iM}}{\mathrm{ZF}\rho}$$

Specimens that were left in an NS4 solution for 72 hours were analyzed for the distribution of hydrogen using secondary ion mass spectrometry (SIMS). Two high concentrations of hydrogen were found, one at the crack tip and another at approximately the region of highest triaxial stress. They also performed potentiodynamic corrosion tests on specimens that were pre-charged with hydrogen and found that the corrosion rate increased. Based on this and SSRT they proposed a modified version of Faraday's law:

$$CV = k_H k_\sigma k_{H\sigma} \frac{iM}{ZF\rho}$$

where $k_H$ is a coefficient relating to the effect of hydrogen on the corrosion current, $k_\sigma$ is a coefficient of the effect of stress on the corrosion current and $k_{H\sigma}$ is a coefficient of the effect of the combination of both stress and hydrogen on the corrosion current. Using thermodynamic analysis, estimations were made for the coefficients and the total multiplication factor ($k_H k_\sigma k_{H\sigma}$) would be 7.1.

Gu et al.'s comparison of the model to actual crack velocities was based on velocities determined from slow strain rate tests, which is not a good test method for determining crack velocities since the velocity is a function of the strain rate and only one of their thermodynamically determined coefficients was shown to affect SCC failures. The model still needs further verification of the coefficients and confirmation based on test methods that are suited for determining crack velocities.

The mechanism for classical SCC was determined to be film rupture (Parkins, 1974). The cracking characteristics of carbon steels in carbonate solutions was researched earlier (Sutcliffe et al., 1972) and the relationship between the formation of a $FeCO_3$ protective film and intergranular SCC was found using

SSRT and potentiodynamic scans with varying scan rates. Parkins (1974) conclusions were that the requirements for cracking were localized dissolution at the crack tip coupled with relative inactivity of all exposed surfaces due to passive film formation and that plastic deformation was required to expose metal for the dissolution process. Consensus has agreed with this conclusion that film rupture was indeed the mechanism.

Although near-neutral-pH SCC has received a considerable amount of research on how stress, environment composition, temperature and potential affect its severity, little research has been conducted on the effect of microstructure.

# Chapter 3 Experimental Procedure

## *3.1 Material*

There were three materials selected for this study; an American Petroleum Institute (API) X-70 pipeline, and American Iron and Steel Institute (AISI) 1018 and 1045 carbon steels. The X-70 pipeline steel is a microalloyed steel with an approximate composition shown in Table 3-1. The steel had a low carbon content and was alloyed with copper, nickel, titanium, chromium and other elements all group into the others category in Table 3-1. The steel was taken from a pipeline that had a diameter of 914.4mm and thickness 14.3mm and its material properties are shown in and Table 3-2.

**Table 3-1: Chemical Composition of X-70 Pipeline Steel**

| Element | Weight Percent (wt%) |
|---|---|
| C | 0.04 |
| Mn | 1.46 |
| S | 0.003 |
| P | 0.008 |
| Others | 0.67 |

Table 3-2: Mechanical Properties of X-70 Pipeline Steel

| YS (MPa) | UTS (MPa) | El (%) |
|---|---|---|
| 545 | 642 | 41 |

The typical chemical composition for AISI 1018 and 1045 are shown in Table 3-3.

Table 3-3: Nominal composition of AISI 1018 and 1045 steel

| Steel | Weight Percent (wt%) | | | |
|---|---|---|---|---|
| | C | Mn | P | S |
| 1018 | 0.18 | 0.85 | 0.04 max | 0.05 max |
| 1045 | 0.4 | 0.75 | 0.04 max | 0.05 max |

### 3.1.1 Heat Treatments

Heat treatments were performed to obtain a variety of microstructures with the same composition. A Lindberg/Blue M furnace was used to heat the specimens, water was used as the quenching medium, normalizing was performed in still air and annealing was accomplished by shutting off the furnace and leaving the material inside. The following tables show the heat treatments and corresponding reference name used throughout this thesis.

**Table 3-4: Heat treatments for X-70 pipeline steel**

| Reference Name | Heat Treatment |
|---|---|
| Quenched X-70 | • Austenized for 1 hour at 950°C<br>• Water quenched |
| Q+T X-70 | • Austenized for 1 hour at 950°C<br>• Water quenched<br>• Tempered for 2 hours at 650°C |
| Normalized X-70 | • Austenized for 1 hour at 950°C<br>• Cooled in still air |
| Annealed X-70 | • Austenized for 1 hour at 950°C<br>• Furnace shut-off, cooled in furnace |

**Table 3-5: Heat treatments for AISI 1018 and 1045 steel**

| Reference Name | Heat Treatment |
|---|---|
| Annealed 1018 | • Austenized for 1 hour at 890°C<br>• Furnace shut-off, cooled in furnace |
| Annealed 1045 | • Austenized for 1 hour at 830°C<br>• Furnace shut-off, cooled in furnace |
| Q+T425 1018 | • Austenized for 1 hour at 890°C<br>• Water quenched<br>• Tempered for 2 hours at 425°C |
| Q+T540 1018 | • Austenized for 1 hour at 890°C<br>• Water quenched<br>• Tempered for 2 hours at 540°C |
| Q+T540 1045 | • Austenized for 1 hour at 830°C<br>• Water quenched<br>• Tempered for 2 hours at 540°C |

### 3.1.2 Cold Worked

To investigate the effect of cold work on the corrosion rate, as-received X-70 was cold rolled using 0.25mm reductions to attain total reductions of 10% - 40% based on:

$$\%\ \text{cold work} = \frac{\text{initial thickness - final thickness}}{\text{initial thickness}} \times 100$$

### *3.2 Slow Strain Rate Specimens*

Dimensions for the slow strain rate test (SSRT) specimen are shown in Figure 3-1.

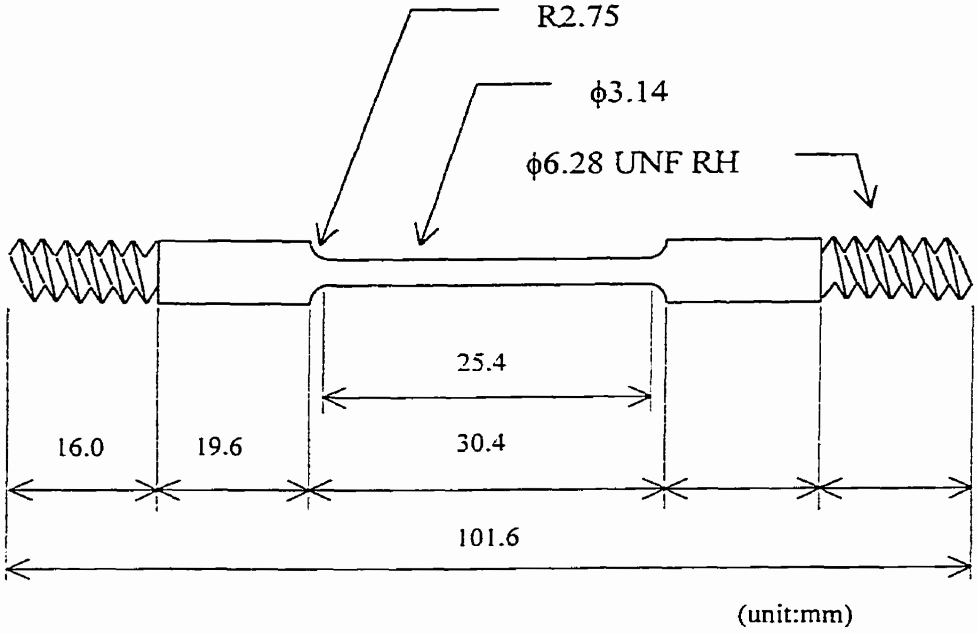

**Figure 3-1: SSRT specimen**

The 914.4mm diameter pipeline is a spiral-welded pipeline using skelp that was approximately 2.25m in width and a thickness of 14.3mm. Specimens were taken from two locations, namely, adjacent to the spiral weld and the midpoint between two spiral-welds. These locations are referred to as edge and centre throughout the rest of the thesis, and their locations are shown schematically in Figure 3-2 in the transverse (to the pipe axis) orientation. Specimens were also taken in the longitudinal direction to compare the orientation effect.

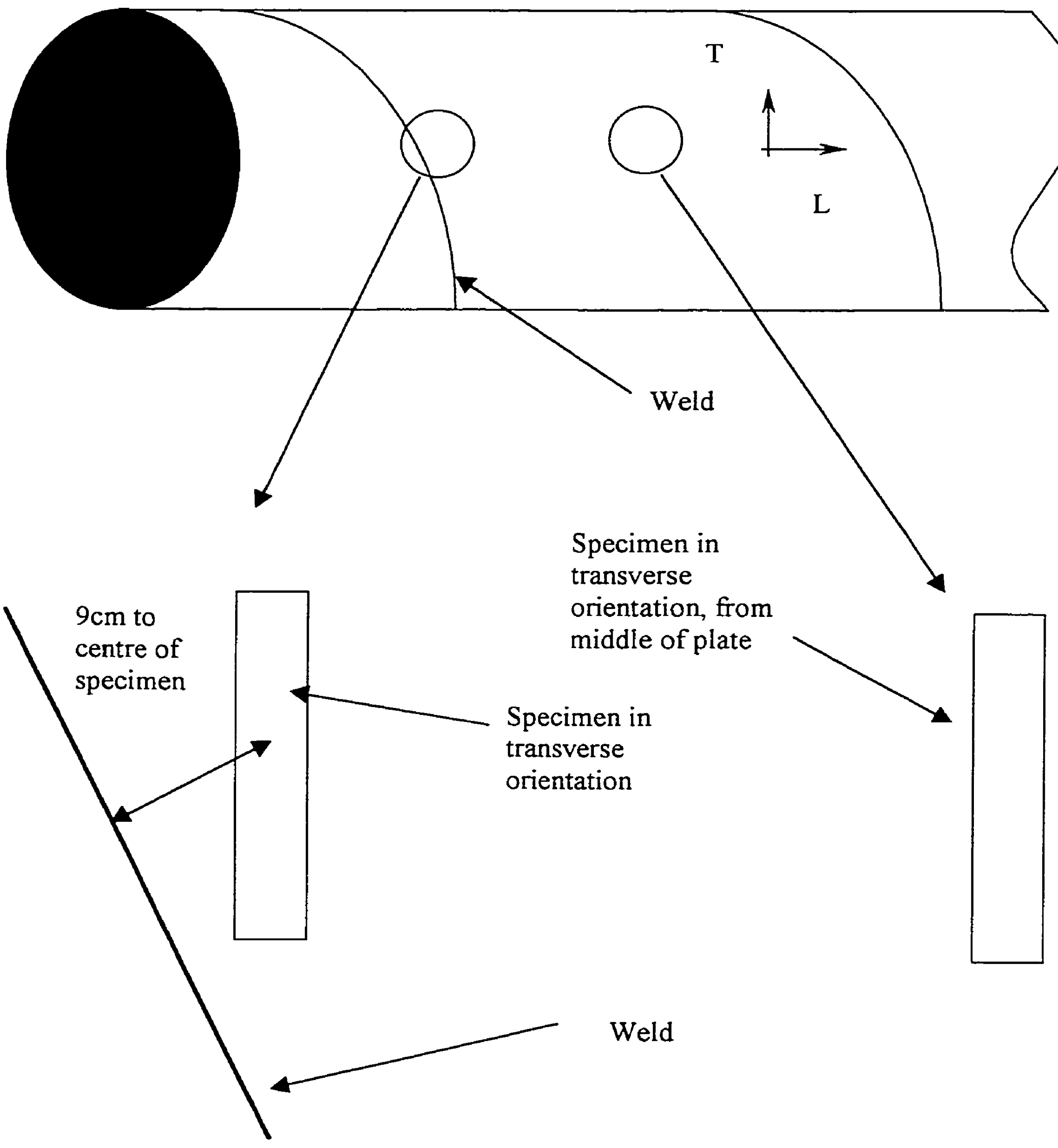

**Figure 3-2: Schematic showing location and orientation of X-70 pipeline steel**

## *3.3 Testing Solution*

The NS4 solution is representative of groundwater found around pipelines that have failed due to near-neutral-pH SCC. The composition of NS4 is shown in Table 3-6.

**Table 3-6: Composition of NS4 solution**

| Compound | $NaHCO_3$ | KCl | $CaCl_2$ | $MgSO_4$ |
|---|---|---|---|---|
| Concentration (g/l) | 0.483 | 0.122 | 0.137 | 0.131 |

The pH of the environment for near-neutral-pH SCC failures in the field ranges from 5.5-7.5 and is anaerobic. To achieve these conditions, a 95% $N_2$/5% $CO_2$ gas mixture is purged through the testing cell. The purge gas composition was based on experimentation that showed that pH was a function of purge gas composition with the pH being below 6 for a composition of 20% $N_2$/5% $CO_2$ and greater than 8 for 100% $N_2$.

## *3.4 Testing Apparatus*

### 3.4.1 SSRT

SSRT were conducted in a MTS Tensile Testing Machine operated by Instron Series IX software. The MTS was operated with a crosshead speed of 0.0005mm/min for the slow strain rate testing and the specimen was pulled to fracture.

### 3.4.2 Potentiostat

A Gamry electrochemical measurement system was used for all electrochemical tests. The Framework software uses Gamrys DC105 software for the open circuit potential, polarization resistance, potentiodynamic, potentiostatic tests and the EIS300 software to run the electrochemical impedance spectroscopy.

## *3.5 Experimental Procedure*

### 3.5.1 SSRT

The SSRT setup is shown schematically in Figure 3-3.

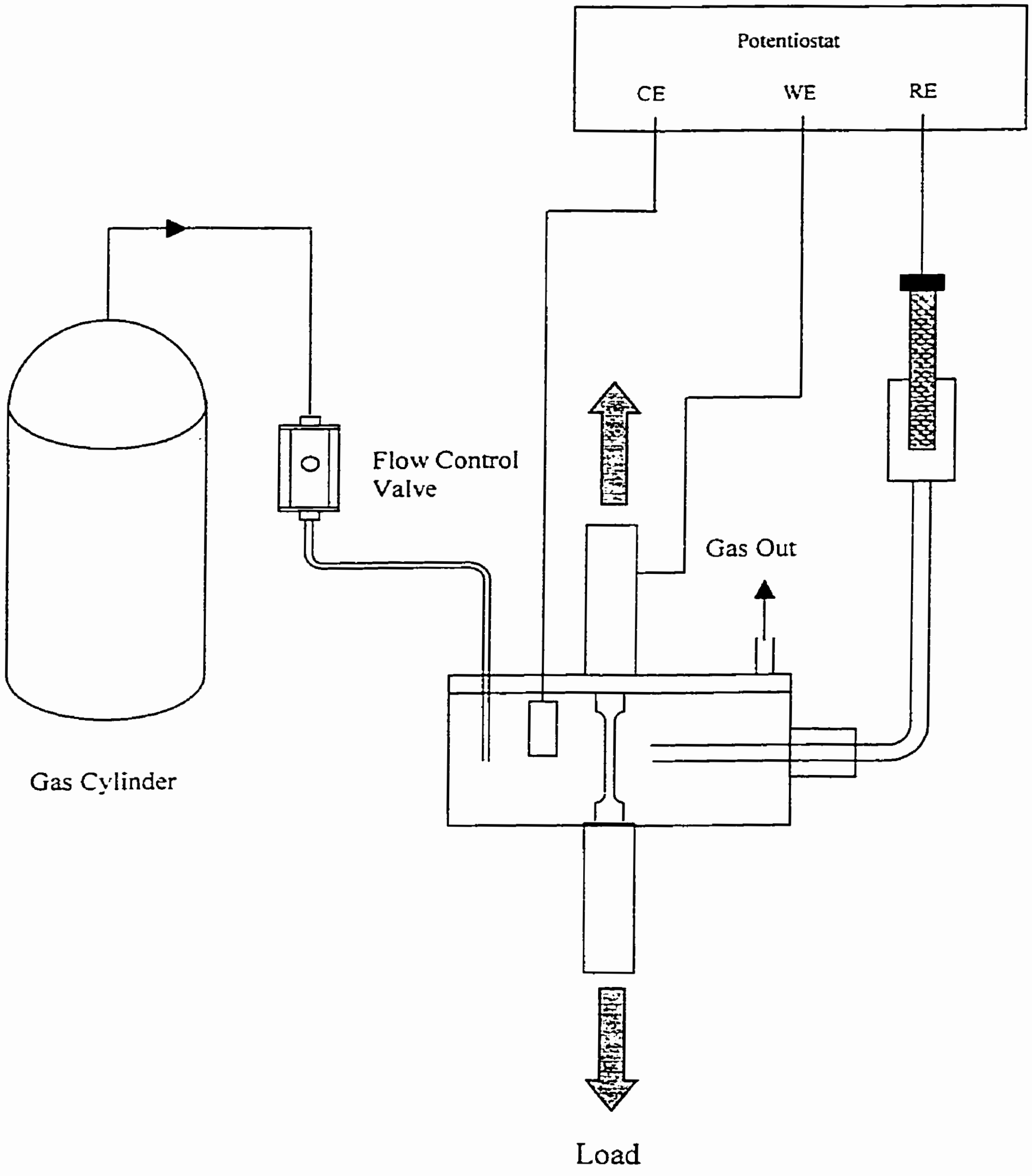

Figure 3-3: Schematic of the corrosion cell and purge gas system for the SSRT

The SSRT specimen shown in Figure 3-1 was placed in a corrosion cell and purged with a 95% $N_2$/5% $CO_2$ for 45 minutes at a flow rate of 5.5 stdml/min. 250ml of NS4 were then added to the corrosion cell and the specimen was held unstressed for a further 6 hours to establish the desired pH of 6.7. The SSRT was then begun at normally a crosshead speed of 0.0005mm/min, an initial strain rate of $3.33\times10^{-7}$ for these specimens, and the specimen was pulled to fracture. After the test was complete, the fractured specimen was immediately removed, ultrasonically cleaned and placed in a dessicator for storage until examination.

To determine the severity of SCC, a comparison is made between a specimen fractured in air and one fractured in the NS4 solution. In both cases, the reduction of area (%RA) was determined and a ratio $RA_{SCC}/RA_{Air}$ determined the severity with the severity increasing with a decreasing value of $RA_{SCC}/RA_{Air}$.

### 3.5.2 Electrochemical Tests

A series of tests were run to determine the corrosion behaviour of the various X-70 microstructures, the carbon steel samples and the cold worked samples. A corrosion specimen was placed in a corrosion cell and held for six hours to allow the pH to reach 6.7. Polarization resistance tests were run at a scan rate of 0.125mV/s from –10mV to 10mV about the corrosion potential ($E_{corr}$). Electrochemical impedance spectroscopy (EIS) tests were run from 100kHz to 2mHz with an amplitude of 10mVAC about $E_{corr}$. Potentiodynamic polarization tests used a scan rate of 0.17mV/s from –1.1 $V_{SCE}$ to –0.4 $V_{SCE}$.

# Chapter 4 Microstructure Results and Discussion

The purpose of this chapter is to present microstructural differences that lead to varying corrosion and/or SCC characteristic. There were two main groupings of materials, the API X-70 pipeline steel and the AISI 1018 and 1045 carbon steel. The majority of the chapter presents the X-70 linepipe with a concentration on the differences between the edge and centre as-received X-70. The presentation of the carbon steel microstructure is brief since the microstructures of carbon steel are well documented.

## *4.1 As-Received API X-70 Pipeline Steel*

An extensive metallographic investigation on this X-70 linepipe classified the microstructure as acicular ferrite with five different types of precipitates being either titanium nitrides, titanium carbonitrides or niobium carbides (Sharma, 2000). Figure 4-1 shows the as-received microstructure with the elongated grains indicating the rolling direction.

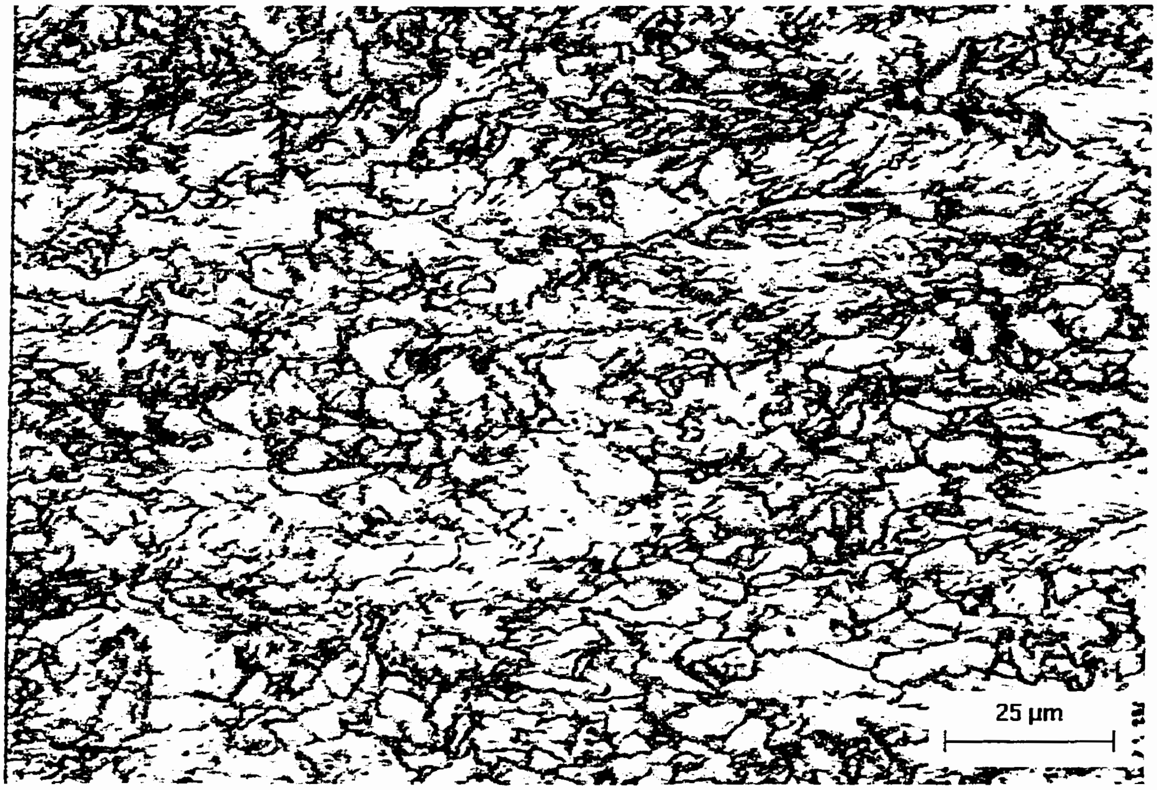

**Figure 4-1: Typcial microstructure of X-70 linepipe**

Sharma (2000) investigation did not examine the change in the microstructure across the width (from one weld seam of the pipeline to the other), which was important in the study of the SCC properties of the pipeline. Sections 4.1.1 to 4.1.3 will discuss the differences across the width of the as-received X-70 linepipe.

### 4.1.1 Grain Size

The ASTM standard for determining grain size is designed to find the average grain size of a microstructure with equiaxed grain size. This X-70 linepipe has an elongated microstructure due its forming process and hence the standard method of determining grain size is not applicable. In order to compare grain size of different locations, a grid with 10 horizontal and 10 vertical lines was used on micrographs taken at a magnification of 2000. The intersection of the lines with grain boundaries was recorded in both the horizontal and vertical directions and the average number of intersections per unit length of line gives a method to compare grain size. Figure 4-2 shows the grid applied to a micrograph with markings applied on two of the lines to indicate how all the lines would be used to determine grain size. A quantification of the grain size was performed at four different locations. In the rolling direction, along the edge and the centre, and viewed at the surface (the O.D. of the pipe) and the middle of the thickness of the pipe (referred to as mid-thickness).

Table 4-1 displays the grain size data in terms of the average distance between intercepts (intercept length), which is the inverse of the number of intercepts per unit length. The elongated grain structure is identified by the horizontal intercept length being greater than the vertical intercept length showing the elongation in the rolling direction as expected. Comparing the surface to the mid-thickness intercept length for both the edge and the centre locations, the grain size increases towards mid-thickness. The increasing grain size towards mid-thickness is expected since the surface of thé skelp would have a greater cooling rate than mid-thickness. Comparison of the grain size along the edge with the centre locations reveals that the grain size at the centre is smaller than at the edge. This is also reflected in the hardness measurements with the centre X-70 having a hardness of HRB 94 and edge X-70 having a hardness of HRB 88.

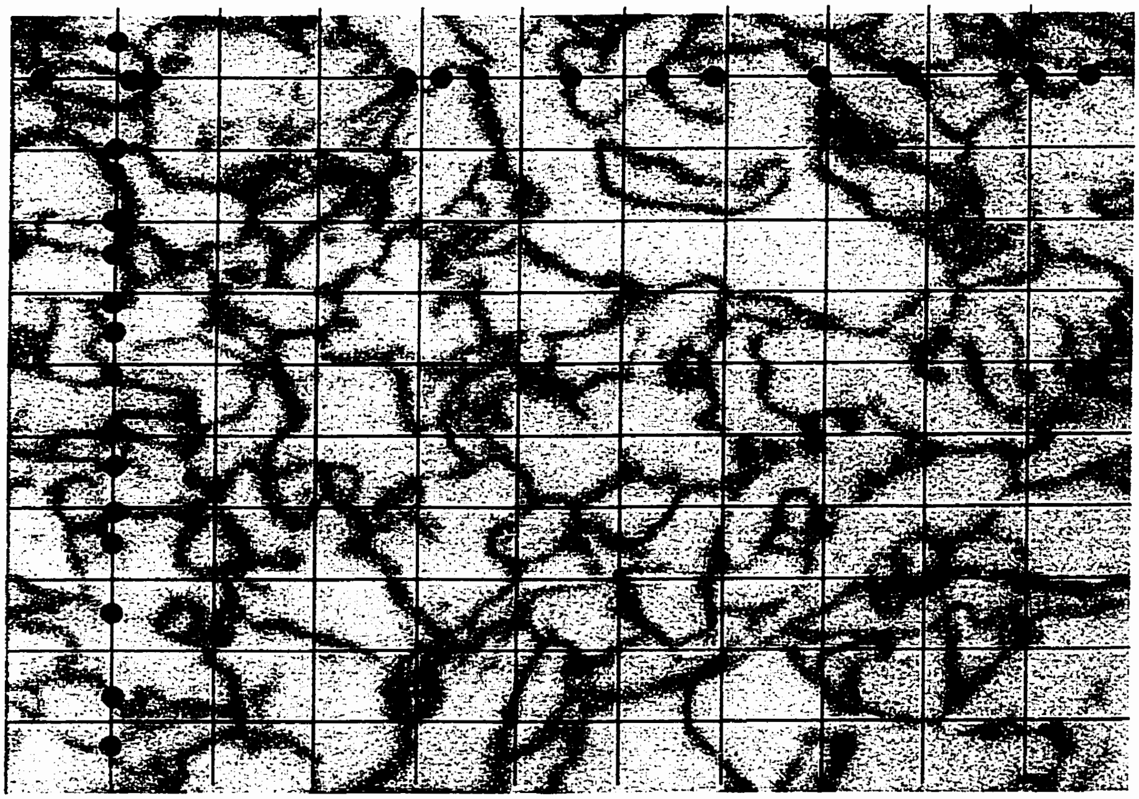

**Figure 4-2: Grid used to determine grain size in the X-70 linepipe steel**

**Table 4-1: Comparison of the grain size in the X-70 linepipe steel**

| Location | Horizontal Average Length (μm) | Vertical Average Length (μm) |
|---|---|---|
| Edge, Surface | 7.61 | 4.25 |
| Edge, Mid-thickness | 10.70 | 6.94 |
| Centre, Surface | 6.38 | 3.91 |
| Centre, Mid-thickness | 7.59 | 5.32 |

The transition of the grain size from the surface to mid-thickness is rapid as shown in Figure 4-3. The grain size increases from the small grain size at the surface and reaches full grain size (full grain size meaning the grain size measured at mid-thickness) approximately 100μm from the surface. This impacts the interpretation of the data presented in Table 4-1. The surface micrographs used in determining the grain size for both edge and centre were centred approximately 20μm below the surface and so represent a small percentage of the overall microstructure (~2%). Therefore the mid-thickness grain size is the best representation of the grain size (representing the grain size of ~98% of the thickness). The same conclusion is still reached when comparing the edge and centre microstructure, the centre has a smaller grain size.

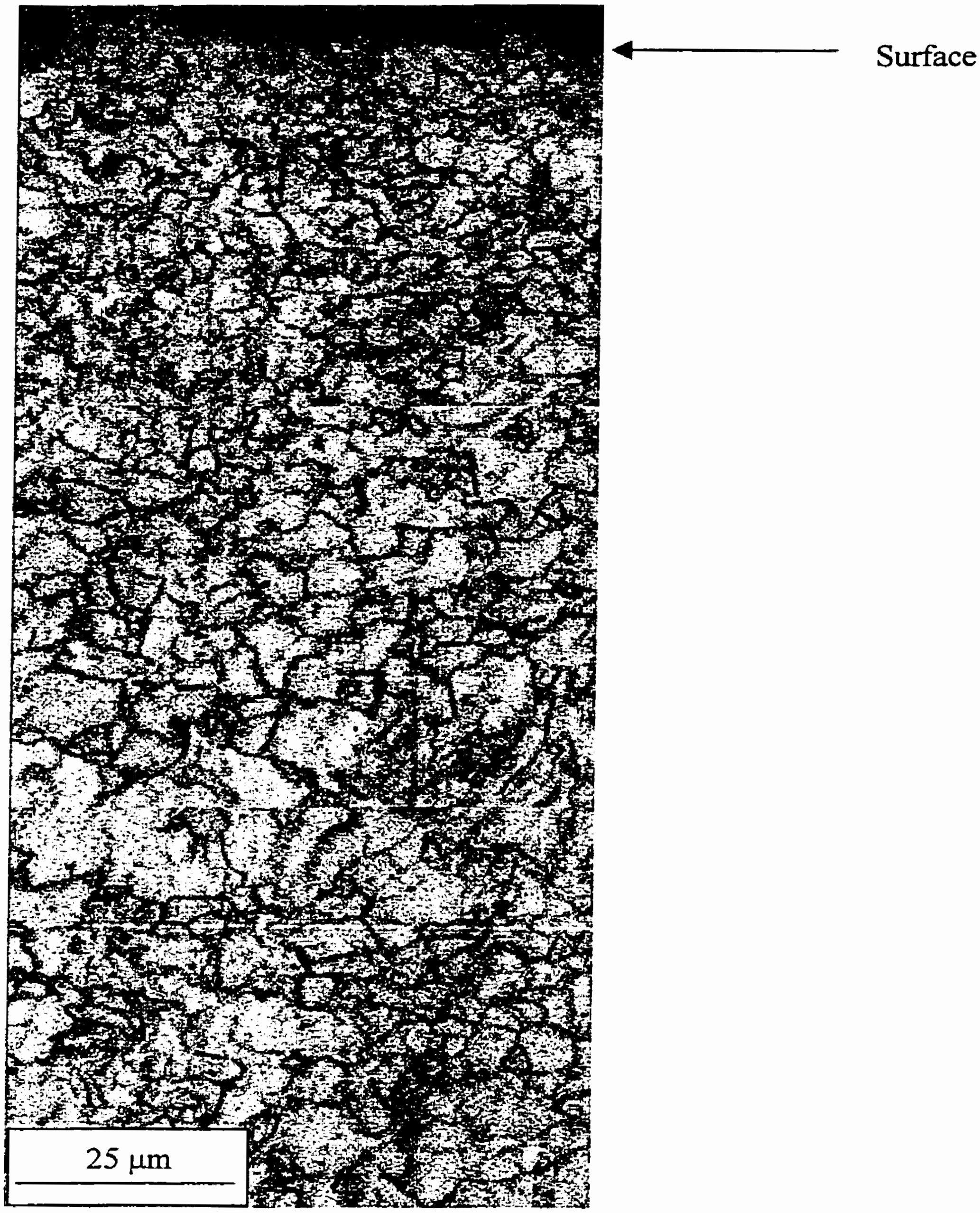

**Figure 4-3: Transition of the grain size from the surface towards mid-thickness**

### 4.1.2 Retained Austenite

Retained austenite was identified by using a modified Le Pera's etch. The modified etch etches ferrite tan, bainite and pearlite black and martensite and austenite white and therefore the amounts of each phase are easily identifiable. In this work, the retained austenite was the main focus since it was already identified as being present in the steel (Sharma, 2000).

An example of a microstructure etched using the modified etch is shown in Figure 4-4. This is taken from the centre at mid-thickness and the retained austenite shows clearly as the white phase (the morphology of the white regions that are visible are basically round and do not represent the expected morphology of lath martensite that would be found at these low carbon contents). A titanium nitride is visible in the bottom middle of Figure 4-4 as identified by the square morphology and its copper colour. This titanium nitride is formed on a calcium sulphide inclusion identifiable as the dark circular region in the middle of the copper coloured square.

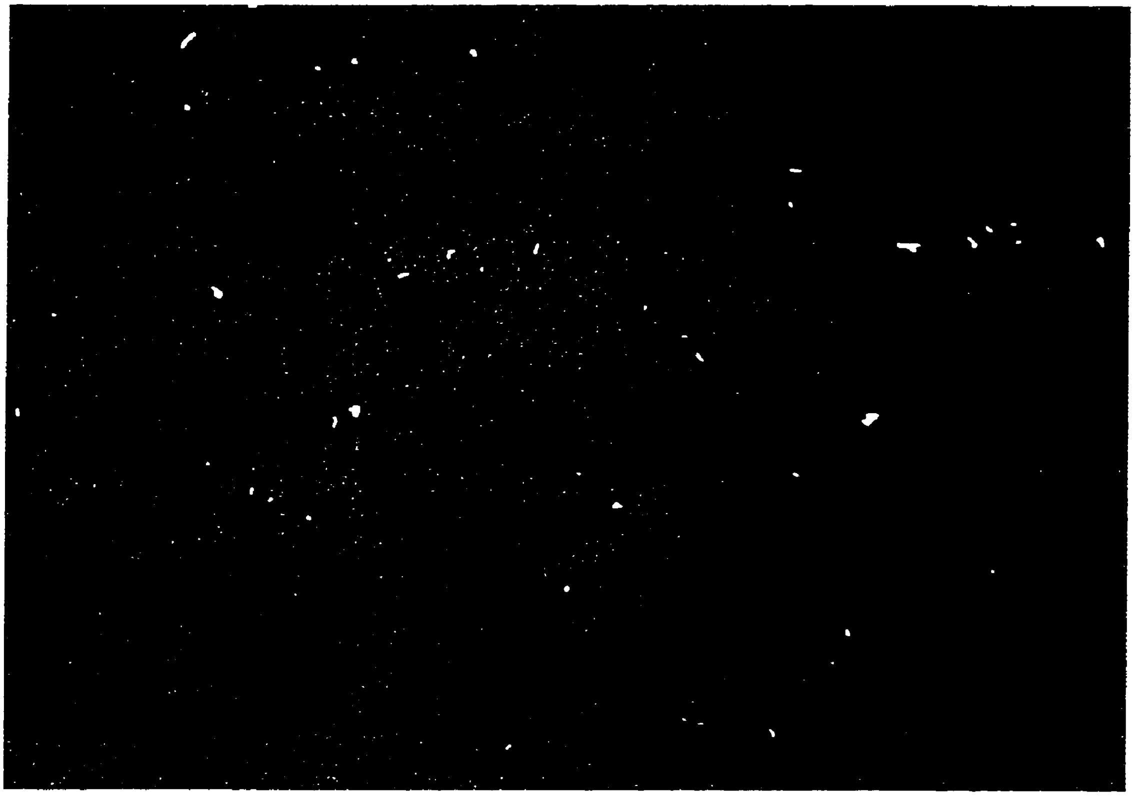

**Figure 4-4: X-70 linepipe etched with a modified Le Pera's etch used to identify retained austenite, 1000x**

Figure 4-5 displays the qualitative data for the retained austenite in terms of an area percentage. The most notable aspect of the data is the low percentage of retained austenite present with the maximum being <0.2%. Looking at the general trend in the data, the retained austenite increases towards the mid-thickness and the centre contains almost twice the amount of retained austenite.

It was observed that the increase in the amount of retained austenite towards mid-thickness was uniform. Quantifying this gradual change would be extremely time consuming since it would require a large number of views and hence was not done.

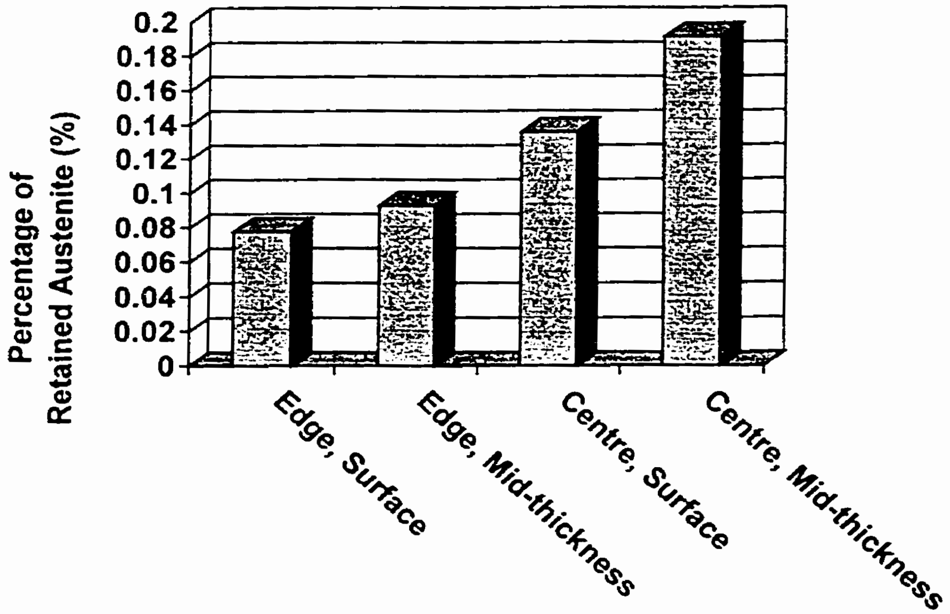

**Figure 4-5: Percent retained austenite in different locations**

### 4.1.3 Inclusions

This X-70 linepipe is calcium treated to reduce the amount of sulfur in the material as well as control the inclusion shape by forming spherical calcium sulfides. Calcium sulfide is a highly water-soluble compound and therefore is nearly impossible to find when a metallography sample is etched with a normal etchant such as 2% Nytol. By minimizing the grinding and polishing times and thereby minimizing the contact time of water to the metallographic sample, the number or amount of inclusions was quantified.

A typical example of the inclusions found in the X-70 steel is shown in Figure 4-6. The inclusions are round and remain round when viewed in the two other orientations (the L-S orientation is shown here) leading to the conclusion that they are indeed spherical. EDX analysis displayed in Figure 4-7 shows that the inclusions are primarily composed of calcium and sulfur.

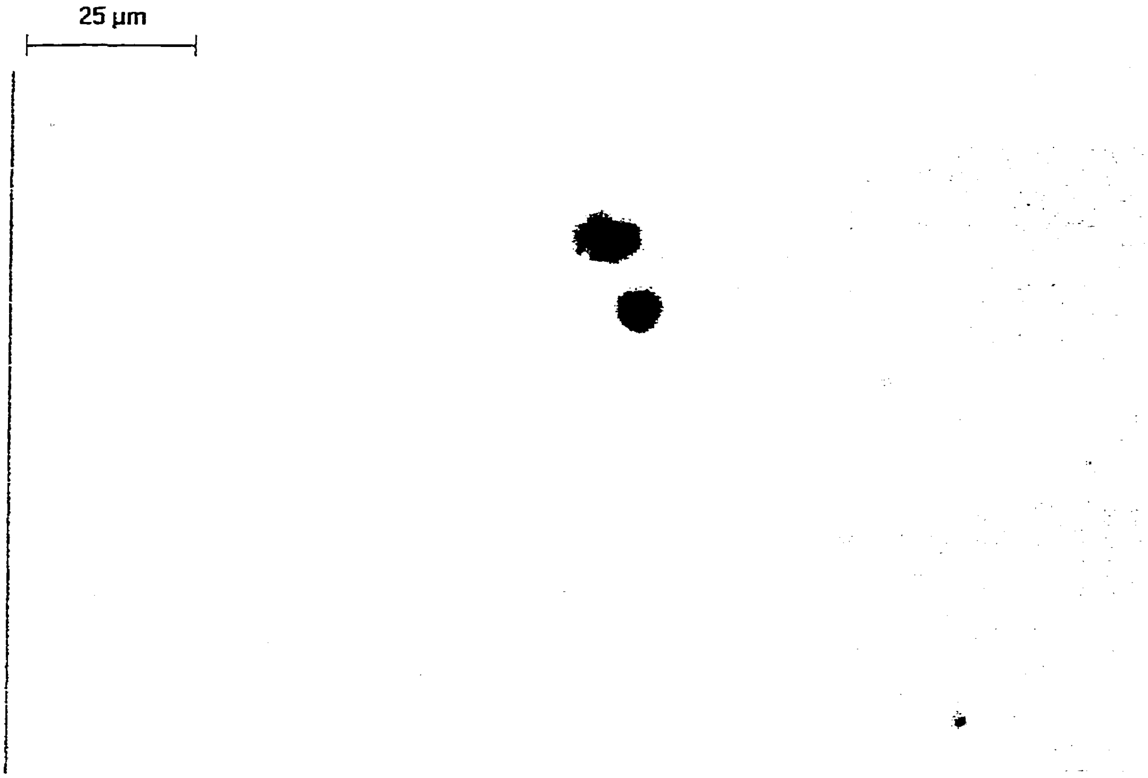

**Figure 4-6: Inclusions found in X-70 linepipe steel, 1000x**

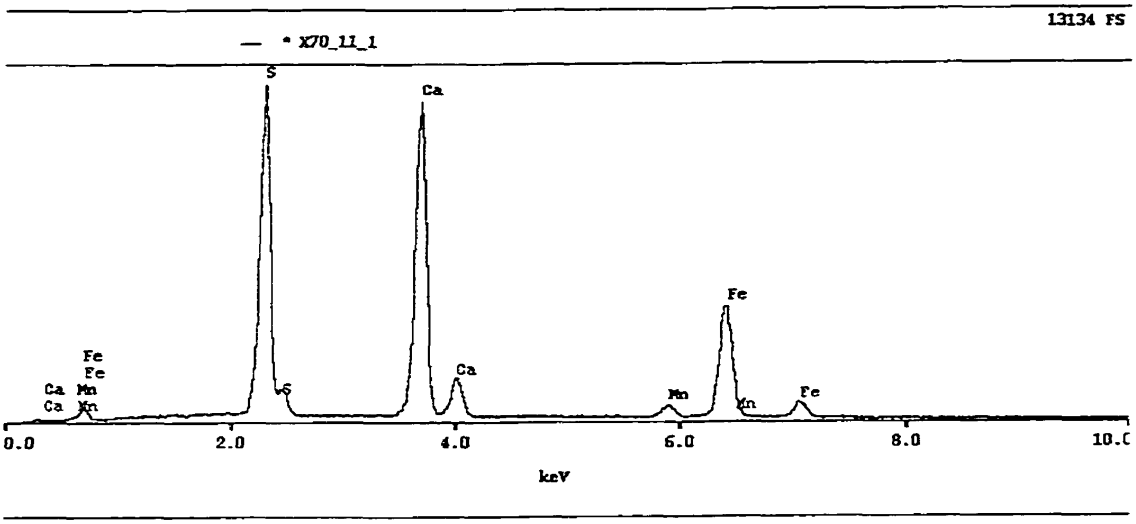

Figure 4-7: Typical composition of the inclusions found in X-70

A quantification of the shape and distribution of the inclusions was performed at four different locations, namely at the outer surface and mid-thickness of the edge and centre samples. The quantification was performed at 1000x magnification.

Information on the inclusions taken from the centre is summarized in Table 4-2 and Figure 4-8. The information in Table 4-2 was found by viewing 120 images (total viewing area is 2.5 mm$^2$) and includes several different calculations. The total number of inclusions found is displayed along with the average area of all those inclusions. The roundness measurement is a calculation that compares the average diameter to the perimeter of an object. As this number deviates from unity as the inclusion goes from spherical to elongated. Figure 4-8 displays the frequency of inclusions based on a nominal size (this nominal size includes areas ±0.5 μm$^2$ of the stated area, i.e.: the 2 μm$^2$ data includes all inclusions between the areas 1.5 μm$^2$ and 2.49 μm$^2$). Hence all the inclusions for the centre surface location (546) along with the mid-thickness inclusions (281) were separated based on their area to give Figure 4-8.

**Table 4-2: Average values for inclusions found samples taken from the centre**

| Location | Total Number of Inclusions | Average Area ($\mu m^2$) | Roundness |
|---|---|---|---|
| Surface | 546 | 6.81 | 1.12 |
| Mid-thickness | 281 | 28.92 | 1.16 |

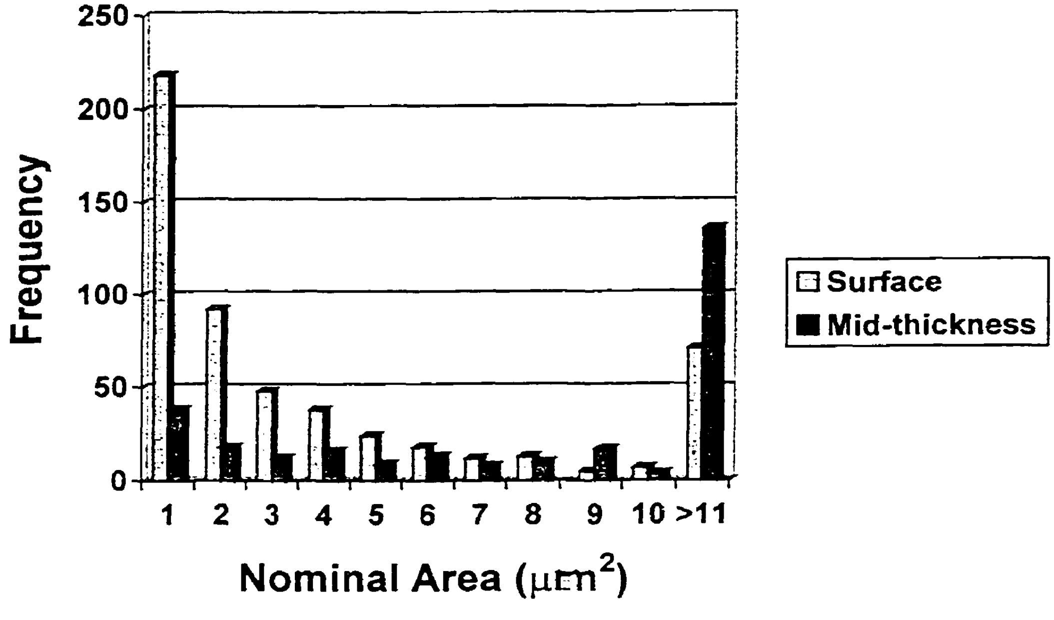

**Figure 4-8: Frequency of inclusions found in centre**

Table 4-2 shows that the number of inclusions found at the surface is approximately twice the amount that is found at mid-thickness but the average inclusion size is much smaller. According to Figure 4-8, the number of small inclusions of area 0.5 $\mu m^2$ to 1.5 $\mu m^2$ accounts for half of the inclusions and large inclusions with area greater than 10.5 $\mu m^2$ accounts for approximately half the inclusions at mid-thickness. The shape of the inclusions at both the surface and mid-thickness is spherical as inferred by the near unity value of roundness calculation.

The data, gathered in the exact same procedure used for the centre X-70, for the as-received edge material is shown in Table 4-3 and Figure 4-9. The number of inclusions adjacent to the surface is greater than the number at mid-thickness with the mid-thickness inclusions being much greater in size. The distribution shows that the surface contains smaller inclusion with approximately half the inclusions being between 0.5 μm$^2$ to 1.5 μm$^2$ whereas the centre has more than half of the inclusions > 11 μm$^2$. This distribution is similar to the inclusion distribution found in the centre. Comparing to the data in Table 4-2 and Table 4-3, there are more inclusions at the centre than at the edge and this is clearly displayed in terms of area fractions in Figure 4-10.

**Table 4-3: Average values for inclusions found samples taken from the edge**

| Location | Total Number of Inclusions | Average Area (μm$^2$) | Roundness |
|---|---|---|---|
| Surface | 300 | 9.69 | 1.10 |
| Mid-thickness | 230 | 24.27 | 1.10 |

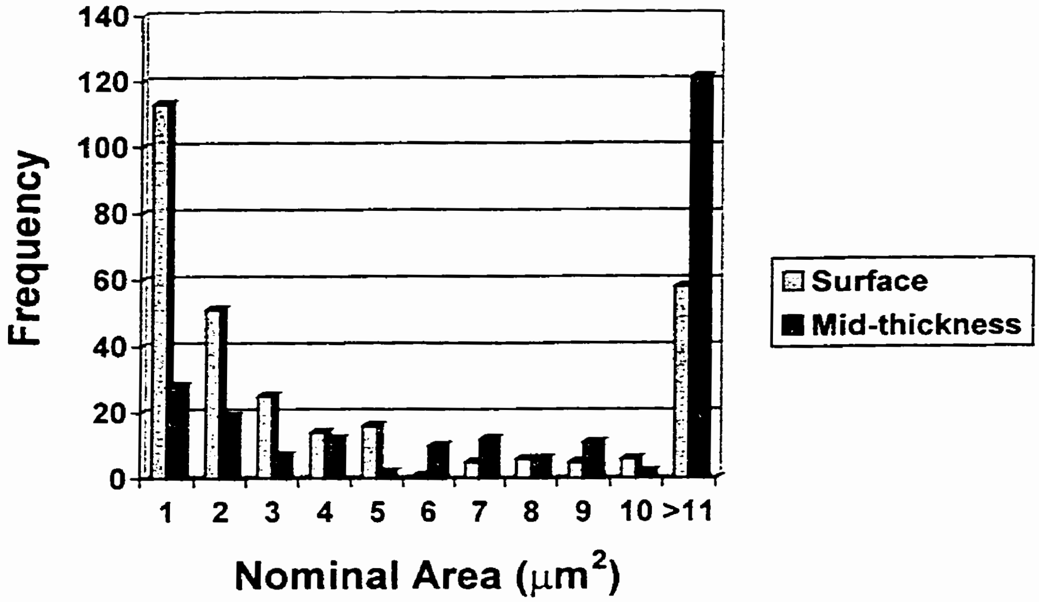

Figure 4-9: Frequency of inclusions found in edge X-70

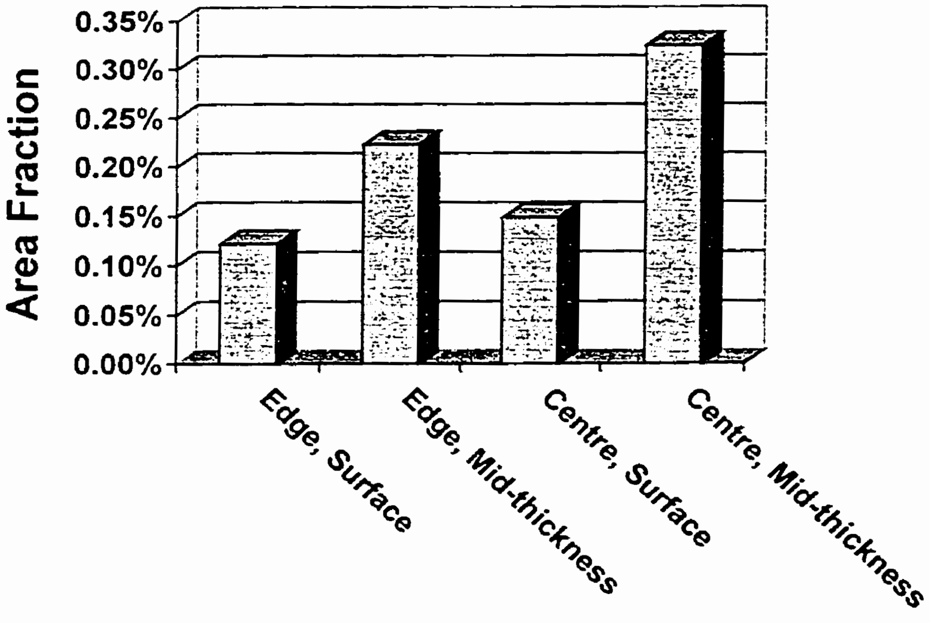

Figure 4-10: Area fraction of inclusions in X-70 linepipe

The distributions of the inclusions are fairly uniform throughout the regions of both the centre and edge material, however some banding of the inclusions was found at the mid-thickness and displayed in Figure 4-11. This banding of inclusions was rare, but in this case stretched across the whole width of the specimen or approximately 15 mm. In another specimen the banding was intermittent across the width with the sections being approximately 1 mm in length.

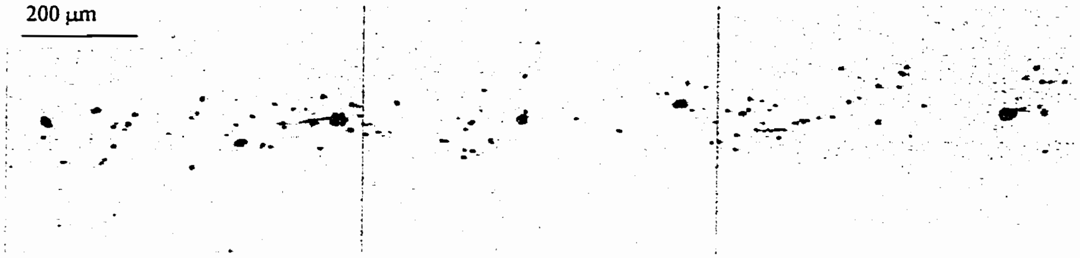

**Figure 4-11: A band of inclusions found at mid-thickness at centre**

A qualitative observation of the inclusions distribution was the gradual increase in the area fraction of inclusions towards mid-thickness. As with the retained austenite, this observation was not quantified.

## 4.2 *Heat Treated X-70 Linepipe*

The heat treatments of X-70 linepipe were performed on material taken from the centre of the pipeline and followed the treatment outlined in section 3.1.1.

### 4.2.1 Annealed

The annealed microstructure was a ferritic/pearlitic microstructure shown in Figure 4-12. The analysis of the annealed microstructure is shown in Table 4-4.

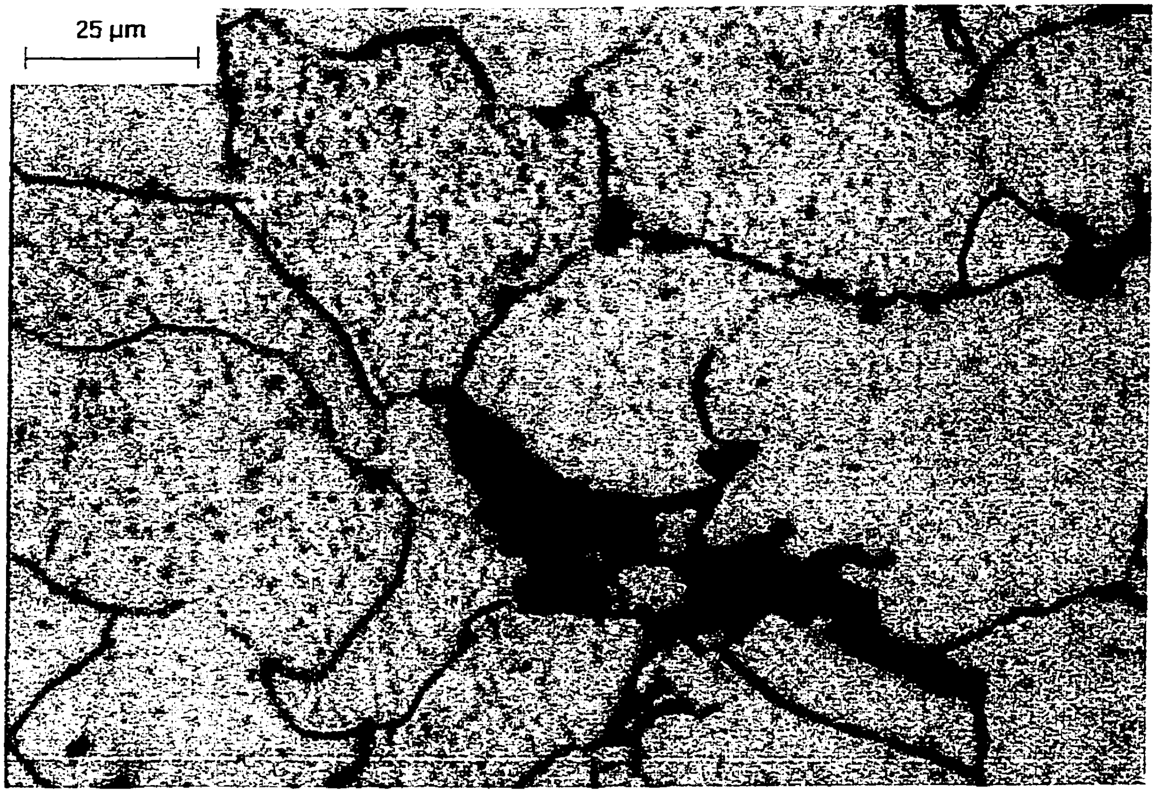

**Figure 4-12: Annealed X-70 microstructure**

**Table 4-4: Characteristics of annealed X-70**

| | Microstructure | % Pearlite | ASTM Grain Size | Hardness |
|---|---|---|---|---|
| Annealed X-70 | Ferritic/Pearlitic | 4.5 | 7.88 | HRB 68 |

The pearlite is not lamellar but is classified as degenerate pearlite since the cementite occurs randomly. Using oil immersion optical microscopy and the SEM, the random orientation (non-lamellar) of the cementite is shown in Figure

4-13. These images were typical of the degenerate pearlite with the pearlite extending from a grain boundary into the ferrite grain boundary.

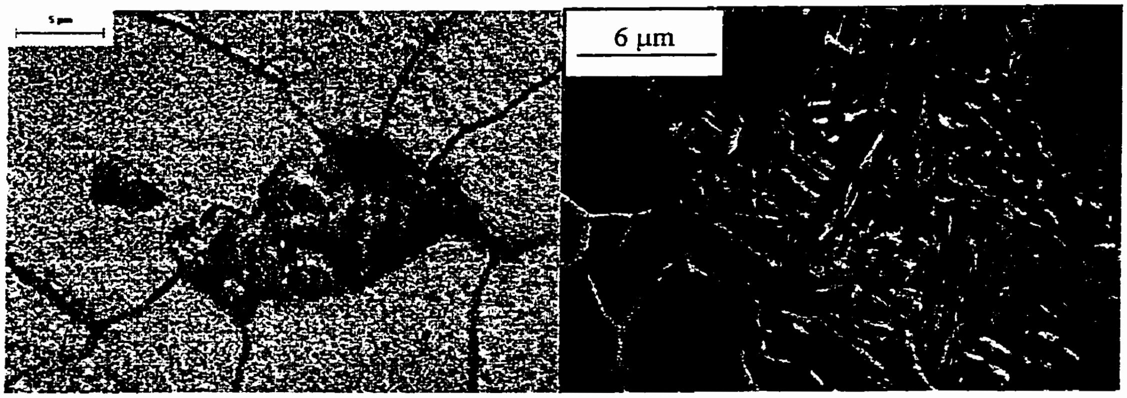

**Figure 4-13: Images of the pearlite found in the annealed microstructure (a) optical image (b) SEM image**

### 4.2.2 Normalized

The normalized microstructure was a ferritic/pearlitic microstructure as shown in Figure 4-14. The analysis of the microstructure is shown in Table 4-5. The normalized microstructure is similar to the annealed microstructure in that it is a ferritic/pearlitic microstructure. The difference is the grain size, ASTM grain size of 9.16 compared to 7.88.

**Figure 4-14: Normalized microstructure of X-70 linepipe**

**Table 4-5: Characteristics of normalized X-70**

| | Microstructure | % Pearlite | ASTM Grain Size | Hardness |
|---|---|---|---|---|
| Normalized X-70 | Ferritic/Pearlitic | 4.17 | 9.16 | HRB 74 |

### 4.2.3 Quenched

The quenching process was the most rapid cooling process used in the heat treatment processes. A standard by IIW (1988) was used to classify the microstructure since this microstructure was similar to microstructures found in autogenous welds. Examples of the microstructure are shown in Figure 4-15 with a low magnification image showing the general structure and then a high magnification image showing mostly acicular ferrite and some ferrite with an aligned second phase.

The results of the microstructure analysis are presented in Table 4-6 with the quenched microstructure being primarily polygonal and acicular ferrite and the hardness value of HRB 97 reflects the high amount of acicular ferrite.

**Table 4-6: Microstructural analysis of quenched X-70 linepipe**

| Constituent | Grain boundary ferrite | Polygonal Ferrite | Acicular Ferrite | Ferrite with an aligned second phase | Ferrite with a non-aligned second phase |
|---|---|---|---|---|---|
| Amount | 14% | 37% | 32% | 16% | 2% |

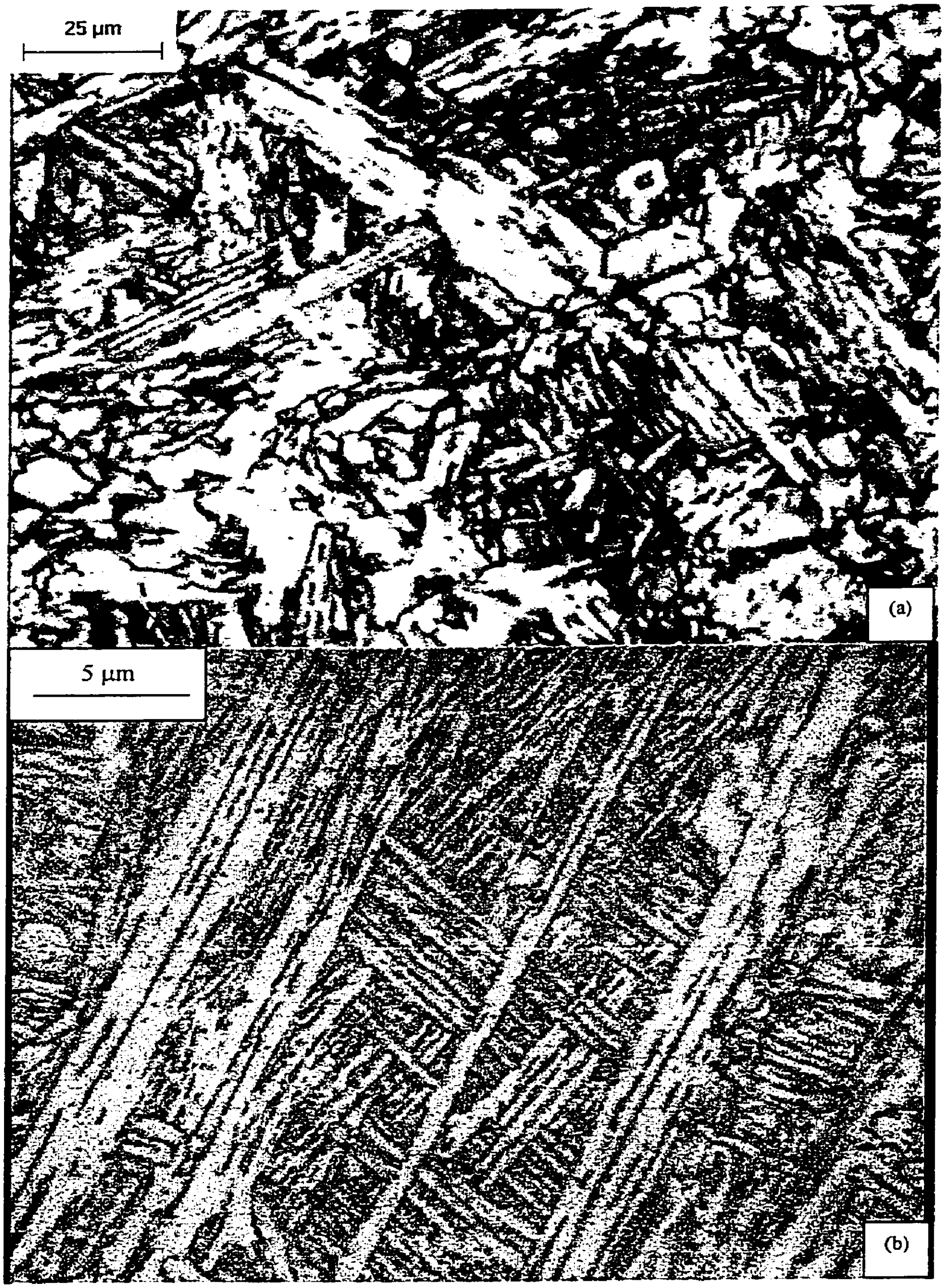

Figure 4-15: Quenched X-70 microstructure, (a) a low magnification image showing the general microstructure, (b) a high magnification image showing mostly acicular ferrite

### 4.2.4 Quenched and Tempered

The tempering of the quenched microstructure leads to coarsening of the quenched microstructure and formation of some polygonal ferrite that is much larger than what is present in the quenched structure. Associated with the change in the microstructure is a drop in the hardness to HRB 94, which is the same hardness as the centre X-70. Classifying the microstructure using the IIW standard as was done with the quenched X-70 was not applicable since the system is not designed for reheated zones. Instead, several images are presented to represent the general quenched and tempered microstructure. The four images shown in Figure 4-16 show that there is a general breakdown of the acicular ferrite that existed in the quenched microstructure and the formation of small equiaxed grains at some of the grain boundaries. There is a combination of grain size but there are generally small grains throughout the structure either due to the original quenched structure or recrystalization without much grain growth during the tempering process.

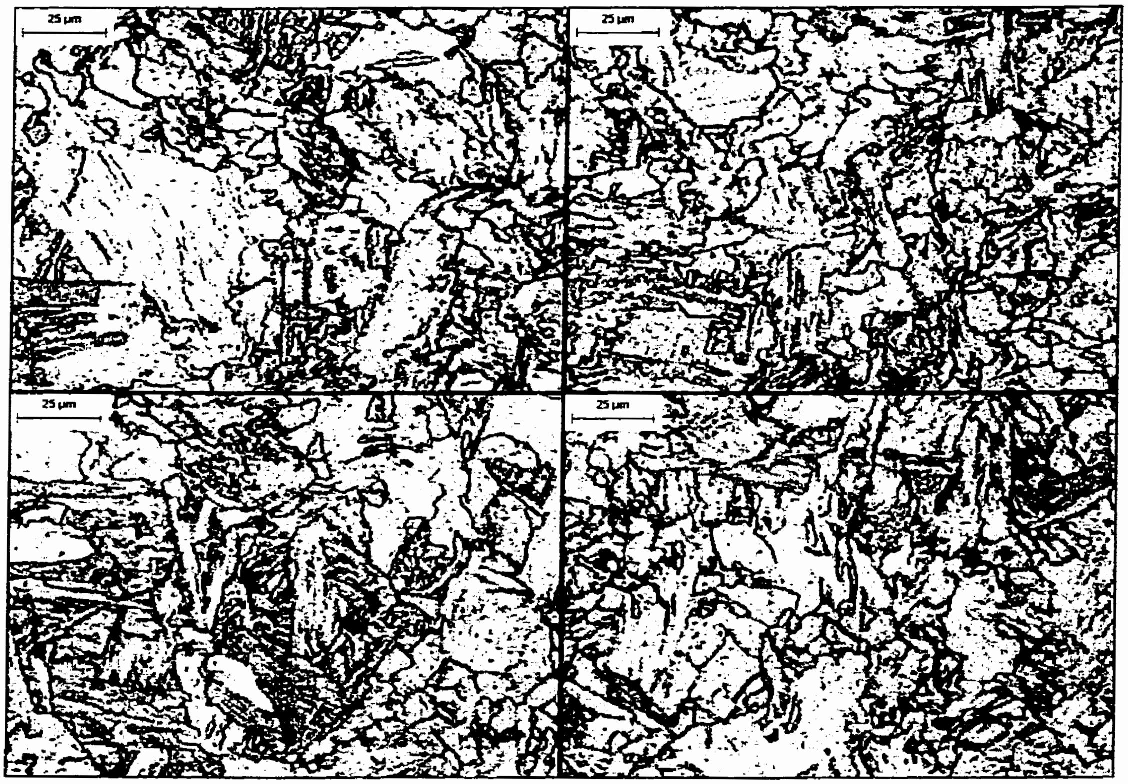

**Figure 4-16: Four different images of the Q+T X-70 microstructure**

## *4.3 Carbon Steel*

The carbon steels were subjected to the heat treatments listed in section 3.1.1. The heat treatments produced a variety of microstructures that were used in both the corrosion and SCC testing. Additional heat treatments were used in only the corrosion tests and are described in this section. The microstructures are only briefly presented since the microstructures of carbon steel are well documented.

### 4.3.1 AISI 1018

The heat treatments used for the 1018 steel were annealing, Q+T425, and Q+T540. In addition to these heat treatments, the 1018 steel was:

- Normalized: austenized at 890°C for 1 hour, cooled in still air;
- Quenched: austenized at 890°C for 1 hour, quenched in still water;
- Q+T675°C: austenized at 890°C for 1 hour, quenched in still water, tempered at 675°C for two hours (referred to as Q+T675 1018 throughout the rest of thesis);
- High temperature anneal: austenized at 1200°C for 1 hour, furnace cooled to 850°C and held for one hour, furnace cooled to 690°C and held for 1 hour, furnace cooled.

Figure 4-17 shows the 1018 microstructures starting with the high temperature anneal, annealed, normalized, quenched and then moving through the tempered microstructures.

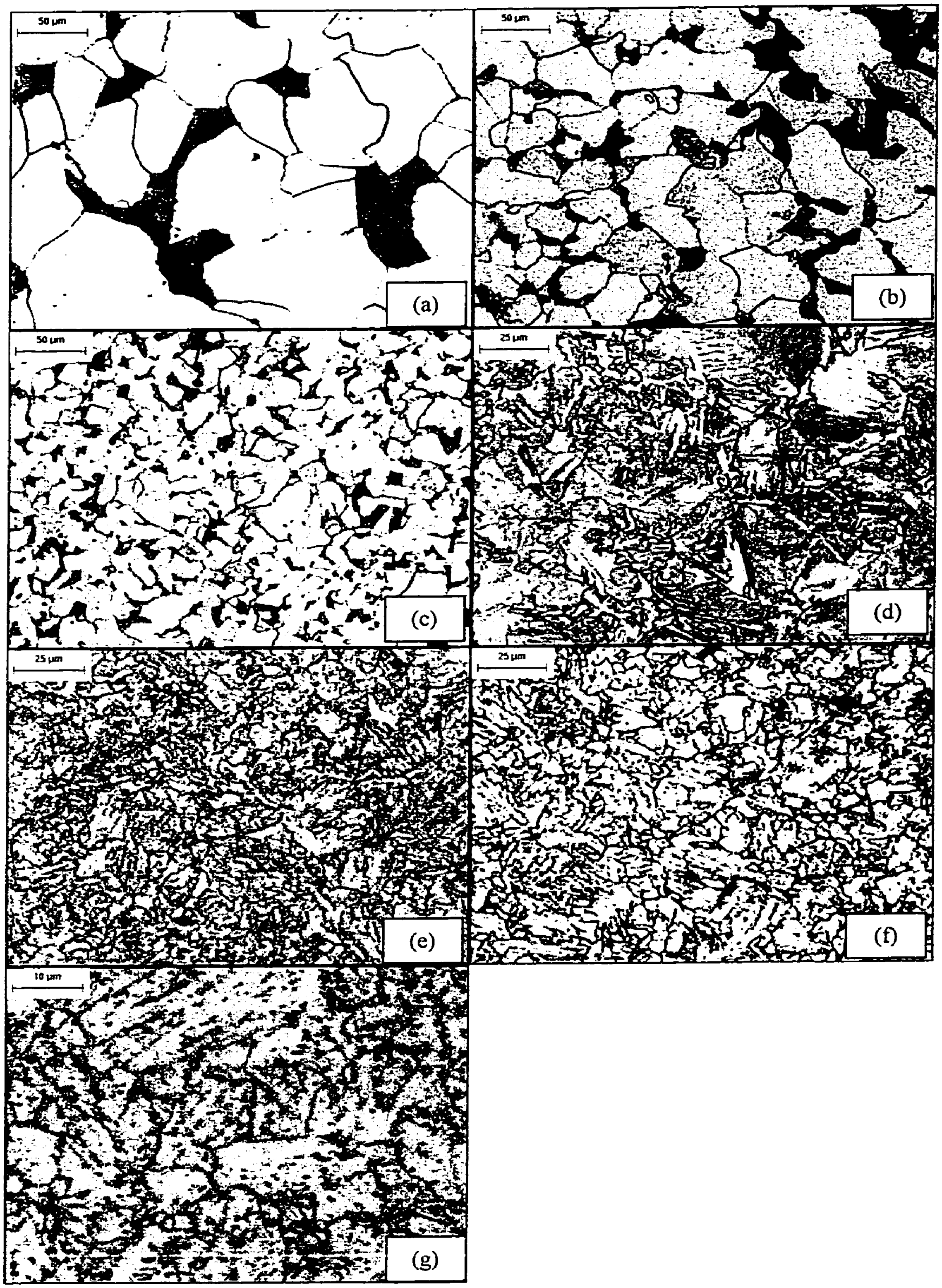

**Figure 4-17: Microstructures of 1018 steel, (a) high temperature annealed, (b) annealed, (c) normalized, (d) quenched, (e) Q+T425°C, (f) Q+T540°C, (g) Q+T675°C**

The effect of the cooling rate is immediately noticeable on the two annealed and the normalized heat treatments. All three contain equiaxed ferrite and pearlite grains but the grain size decreases with an increasing cooling rate. The grain size and hardness are shown in Table 4-7.

**Table 4-7: Characteristics of annealed and normalized 1018**

| Microstructure | ASTM Grain Size | Hardness |
|---|---|---|
| High temperature anneal | 5.72 | HRB 68 |
| Annealed | 7.63 | HRB 74 |
| Normalized | 9.14 | HRB 82 |

The tempering of low to medium carbon martensite has several stages as shown in Table 4-8.

**Table 4-8: The tempering process on low to medium carbon steels**

| Temperature | Event |
|---|---|
| <200°C | • <0.2% C, carbon segregation at dislocations<br>• >0.2%C, carbon segregation at dislocations and formation of ε-carbide |
| 200-325°C | • Segregated carbon forms fine rod shaped carbides |
| 325-600°C | • Formation and recovery of ferrite |
| 400-600°C | • Dissolution of ε-carbide and formation of spherical $Fe_3C$ |
| >600°C | • Recrystallization of ferrite to equiaxed ferrite and growth of $Fe_3C$ |

Figure 4-17 shows that the quenched microstructure is a lath microstructure and the tempering process transforms this into tempered martensite resulting in the breakdown of the martensite that is visible for Q+T425°C. The higher tempering temperature of 540°C gives more acicular shaped to ferrite but the further precipitation of $Fe_3C$ is difficult to see optically. The high temperature temper produced spheroidite with large equiaxed ferrite grains and coarse cementite. The hardness of the martensitic and tempered martensite microstructures are shown in Table 4-9.

**Table 4-9: Hardness of quenched and quenched and tempered 1018 microstructures**

| Microstructure | Hardness |
|---|---|
| Quenched | HRC 34 |
| Q+T425°C | HRC 28 |
| Q+T540°C | HRB 97 |
| Q+T675°C | HRB 82 |

### 4.3.2 AISI 1045 Microstructure

Only the annealed and Q+T540°C heat treatments described in the section 3.1.1 were used for the 1045 steel and the resulting microstructures are shown in Figure 4-18. The annealed 1045 was a pearlitic/ferritic structure with 73% pearlite. The microstructure showed equiaxed grains with an ASTM grain size 10.85 and hardness HRB 88. The tempering process of the 1045 steel follows closely the events given in Table 4-8 with the microstructure showing extensive carbide precipitation in acicular shaped ferrite. The hardness of Q+T540°C was HRC 29.

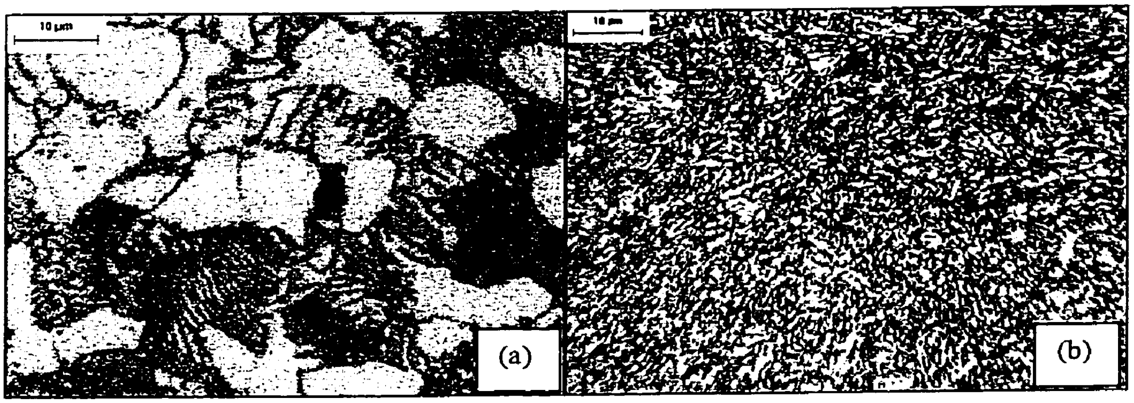

Figure 4-18: Microstructures of 1045 steel, (a) annealed, (b) Q+T540°C

# Chapter 5 Corrosion Results and Discussion

The chapter investigates the corrosion behaviour of microstructures used in the SCC testing. To provide further insight to these behaviours other microstructures, such as the high temperature anneal and the Q+T675 1018, and conditions, cold worked samples, were tested. The chapter first presents the corrosion results of X-70 linepipe used in the SCC testing and then discusses features that were found on the corroded surface. The chapter then presents the carbon steels used in the SCC testing and also examines their corroded surfaces. Several sections discuss the results of various microstructural effects such as grain size and tempering in order to explain the differences of the original tests. Finally sections on the effects of plastic deformation, surface roughness and hydrogen are presented.

The corrosion behaviour of the microstructures was characterized using three main types of tests: polarization resistance (PR), potentiodynamic scans (PD) and electrochemical impedance spectroscopy (EIS). The operating parameters used for each case were discussed previously in the section 3.5.2. Measuring the potential of the platinum counter electrode versus the saturated calomel electrode was also performed to see if the environment is deaerated with a solution considered deaerated if the potential is less than $-100$ $mV_{SCE}$ (Stafford et al., 1980). The potential of the platinum electrode was normally about $-450$ $mV_{SCE}$ indicating a deaerated solution.

## *5.1 Corrosion Results for Materials used in the SCC Testing*

### 5.1.1 X-70 Linepipe Steel

Typical results for the as-received centre material are shown in the following figures. Figure 5-1 presents the PR test data with a linear interpolated line of best fit with the slope of the line being the polarization resistance. The goodness of fit of the interpolation is reflected in the goodness of fit value, $R^2$, approaching unity and this was consistent throughout all of the PR tests. Polarization resistance is actually the slope at $E_{corr}$, $R=dV/di|_{Ecorr}$, and is approximated by taking the slope over a limited range about $E_{corr}$, $R=(V_2-V_1)/(i_2-i_1)$. The high $R^2$ value means that the voltage range, -10 mV to +10 mV about $E_{corr}$, was the proper range since too large of a range will deviate from being linear and make the approximation incorrect.

Figure 5-2 presents the PD data with the slopes of the interpolated lines giving the Tafel constants for the system and a line showing $E_{corr}$. Again there is a high $R^2$ value for the regression reflecting the high goodness of fit of the interpolation, which was consistent throughout all of the tests on the microstructures.

The existence of only an active behaviour in the PD scans as opposed to a active/passive behaviour is consistent with other researchers (Liu et al., 1993 and Beavers et al., 1998). Liu et al. tested X-80 linepipe in bicarbonate solutions varying in concentration from 0.005 M to 1 M as well as an NS4 solution. The steel in the high concentration bicarbonate solutions had an active/passive behaviour and the Flade potential decreased with decreasing concentration. When sodium chloride (NaCl) was added to the dilute solutions or when NS4 was used there was only an active region. These researchers attribute the decrease in the passive region to decreasing stability of the $FeCO_3$ and that the salt additions lead to a further decrease in stability.

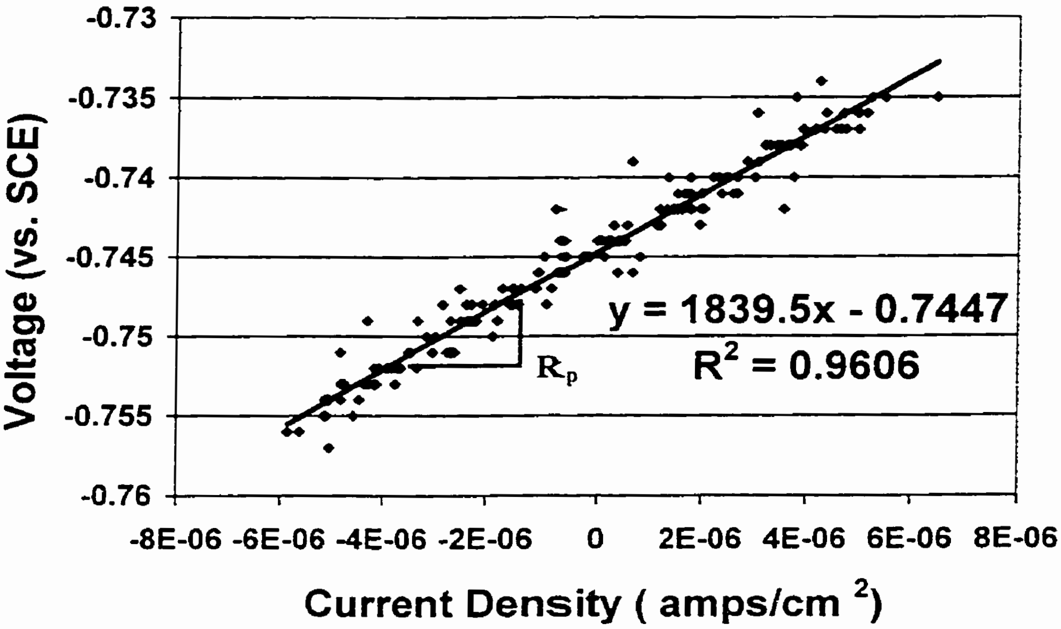

**Figure 5-1: A typical polarization resistance result for centre X-70 linepipe steel**

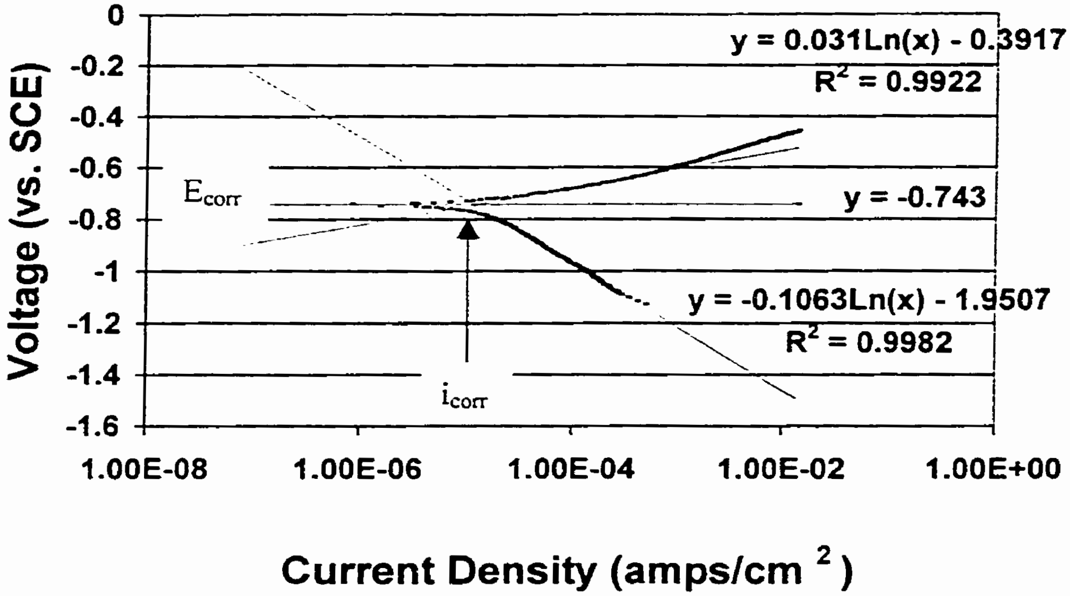

Figure 5-2: A typcial potentiodynamic scan for centre X-70 linepipe steel

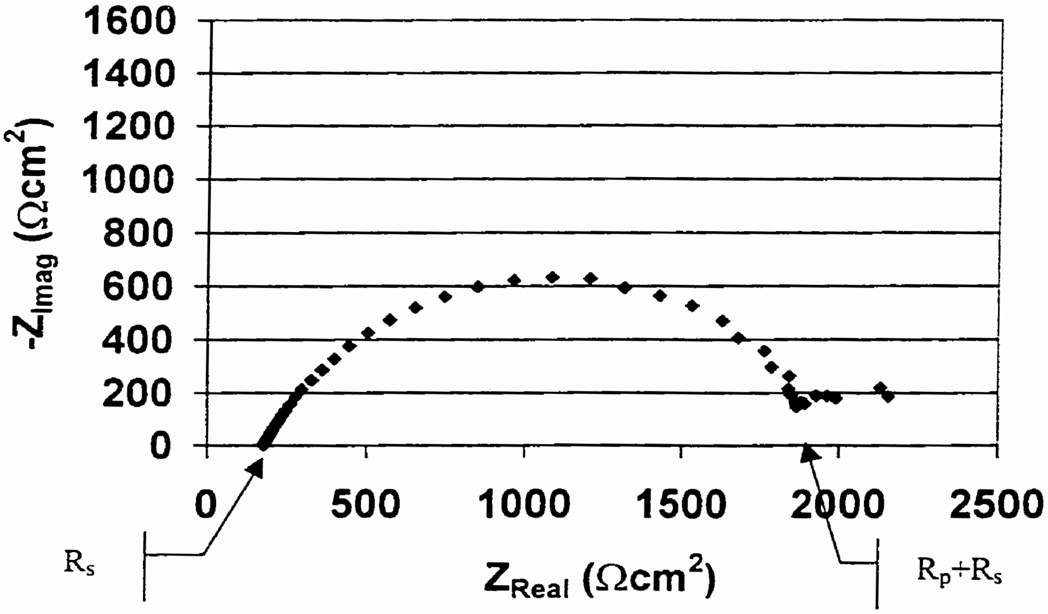

Figure 5-3: A typical EIS plot for centre X-70 linepipe

The typical EIS data is shown in Figure 5-3 in the form of a Nyquist plot. Through EIS theory, the data from a corroding system forms a semi-circle and in this case the semi-circle is depressed with the mid-point below the x-axis. Also prevalent is the low frequency scatter on the right hand side of the data due to a surface process such as carbonic acid (and hydrogen ion) reduction or a change in the surface such as a deposition (Cottis and Turgoose, 1999). Alternatively, some of the systems had the beginning of a second semi-circle in the low frequency range. The presence of a low frequency loop in an environment that passivates aluminum is due the protective oxide layer that forms (Cottis and Turgoose, 1999). In this system there is no protective layer but there is a $FeCO_3$ corrosion product that forms on the surface that could be the cause of the low frequency loop.

The high $R^2$ values and repeatability of the various tests is not only a reflection of the use of proper testing parameters, but also stability of the environment. Once the NS4 environment attained a stable pH, the corrosion potential of any tested steel varied by less than 1 mV over a time period of at least six hours. The repeatability of the tests is reflected in the corrosion potential variation between a single microstructure, prepared and tested on four different days with $E_{corr}$ attaining the values –742.0, -742.5, -742.6 and –743.4 $mV_{SCE}$.

The PR comparison of the average polarization resistances between the different microstructures for X-70 is shown in Figure 5-4. The annealed microstructure has the largest resistance and the quenched and the centre microstructure having the lowest resistance. The as-received material from the different locations within the pipe has a relatively large difference and this difference will be discussed in depth later in this chapter.

Although there is very little difference between the Q+T, normalized and edge microstructures' polarization resistance, the actual corrosion current depends on the Tafel constants determined from PD scans. Using the Tafel constants found from PD scans; the corrosion current based on polarization resistance is shown in Figure 5-5 (a useful relationship is that 10 $\mu$amp/cm$^2$ is approximately equal to a corrosion rate of 0.12 mm/year for steel). There is a slight difference in the corrosion current between the three microstructures with similar resistances and the difference is clearly shown by plotting the difference in the corrosion current compared with the annealed microstructure, Figure 5-6. The data shows that the three intermediate microstructures have corrosion currents 5% to 10% greater than the annealed microstructure whereas the quenched and the centre microstructures have corrosion currents that are about 25% greater.

The minimum and maximum polarization resistances attained for each microstructure are also shown in Figure 5-4. The experimental range of the polarization resistances for all microstructures was maximum ±4.5% of the mean (the edge X-70 had the largest range in data). The overlapping range in data reinforced the conclusion that the intermediate microstructures' resistances are not different. However the small range in data (less than ±4.5% of the mean) reinforces the conclusion that the other microstructures have resistances that are indeed different since the difference in the averages is much greater than 4.5%.

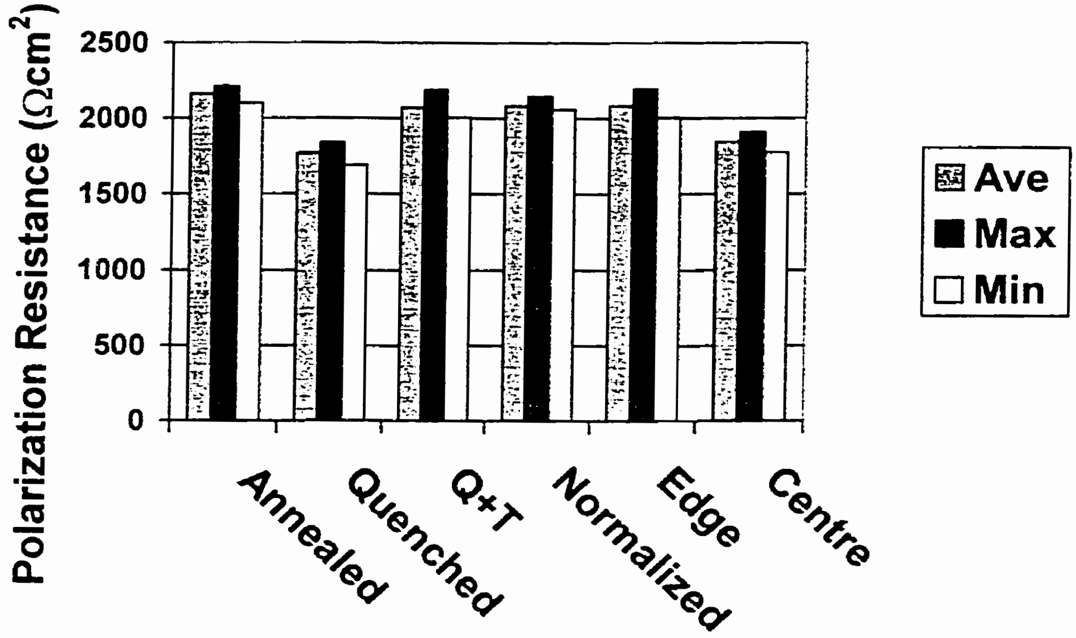

Figure 5-4: Polarization resistance for various X-70 microstructures

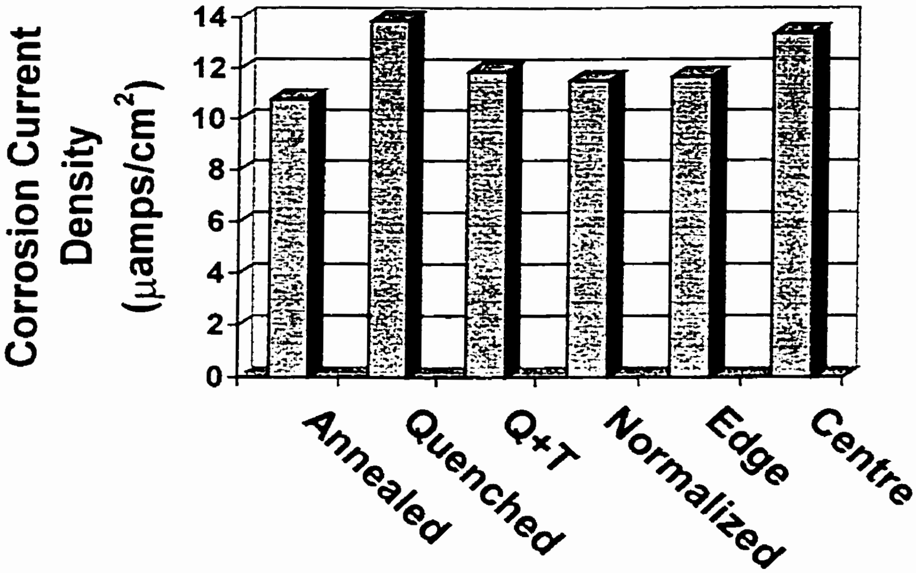

Figure 5-5: Corrosion current of various X-70 microstructures as determined from the polarization resistance

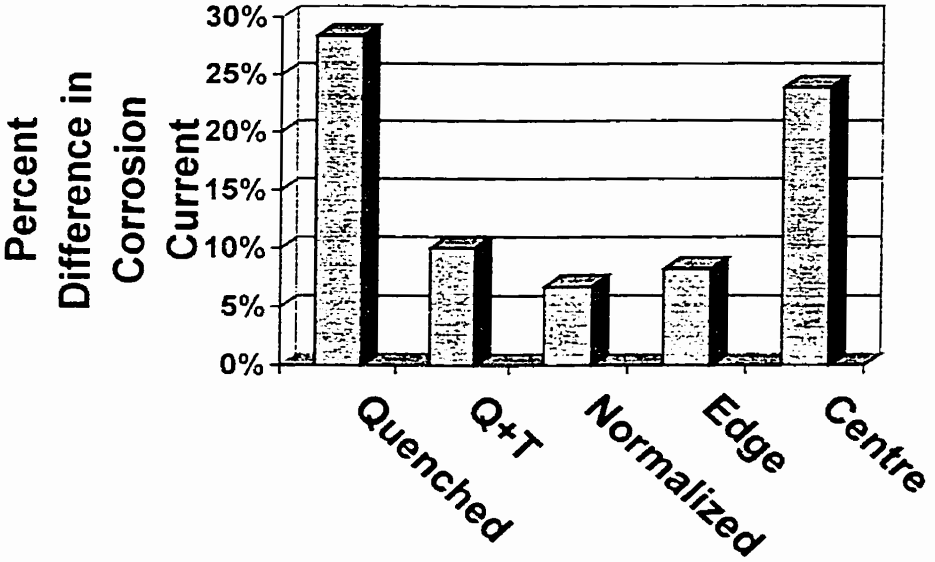

Figure 5-6: Percent difference in corrosion rate of various X-70 microstructures compared to the annealed microstructure determined from polarization resistance tests

A second method used to classify the corrosion characteristics of the different X-70 microstructures was PD scans. The corrosion current was determined using the intercept of the interpolated cathodic Tafel line with $E_{corr}$ and are displayed in Figure 5-7. The results are similar to the results from the PR testing with the annealed microstructure having the lowest corrosion current and the quenched and centre microstructure having the highest corrosion currents. The other microstructures have intermediate corrosion rates that differ slightly from one another similar to the results of Figure 5-5.

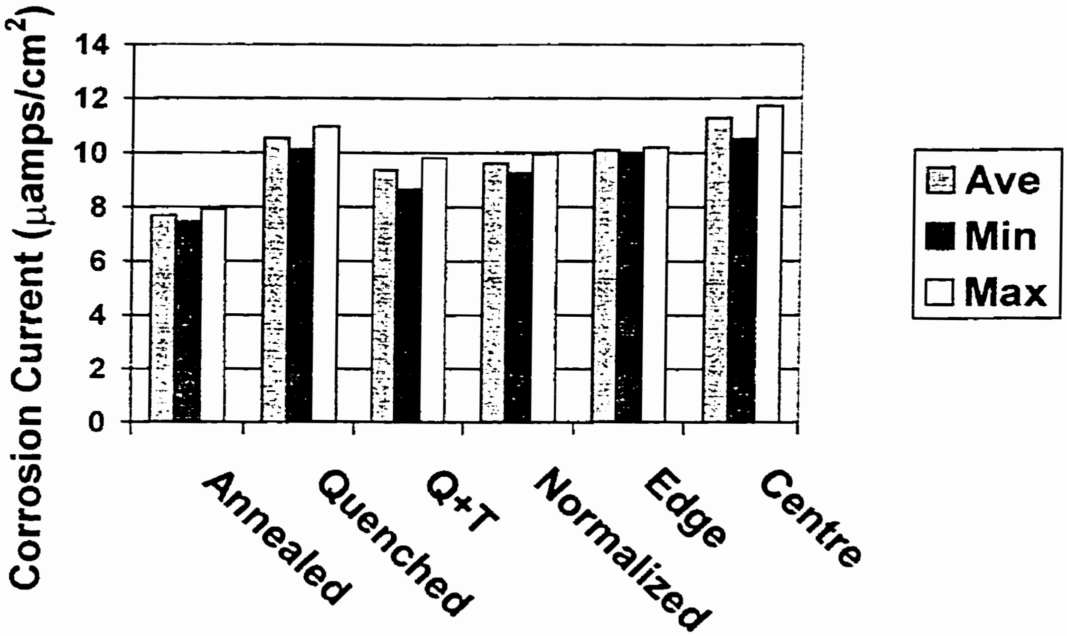

**Figure 5-7: Corrosion current determined from potentiodynamic scans**

Examining the small differences between minimum and maximum currents attained for each microstructure in Figure 5-7 demonstrates the stability of the PD testing procedure that was observed with the PR testing. In this case the edge microstructure corrosion currents were slightly higher than the other microstructures with intermediate corrosion current with its minimum value being greater than the others maximum value.

A clearer comparison of the results from the PD scans is shown in Figure 5-8, which compares the corrosion rate of the other microstructures to annealed X-70. The differences obtained from the PD scans are larger than those obtained from the PR testing with the quenched and the centre X-70 being about 35% to 45% greater than the annealed microstructure due to a different test method, but the general trend between the microstructures is still the same as in the PR testing.

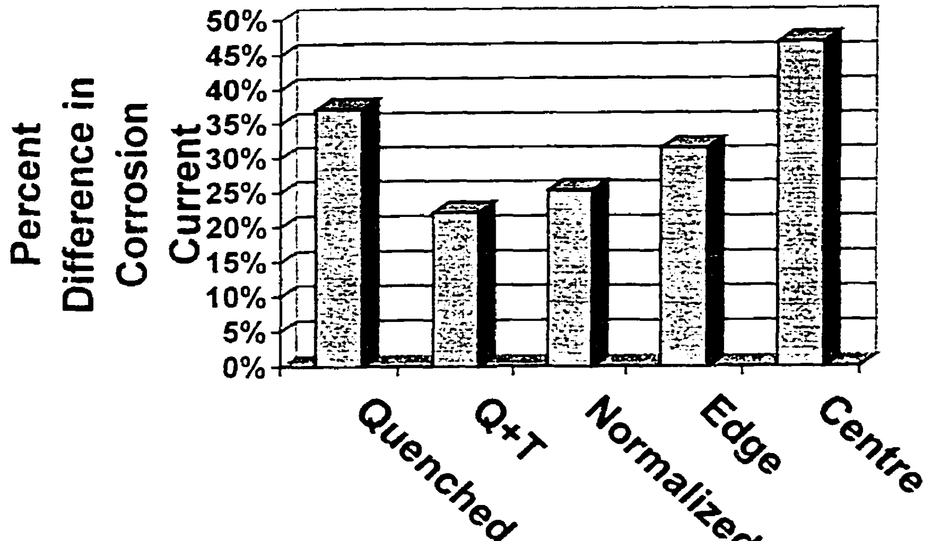

**Figure 5-8: Percent difference in corrosion current of various X-70 microstructures compared to annealed microstructure determined from potentiodynamic tests**

A comparison of the corrosion rate from the EIS testing is shown in Figure 5-9 without the low frequency data. The polarization resistance is the intercept of the semi-circle low frequency data with the real axis minus the solution resistance, which is the intercept at the high frequency end. Since the solution resistance was nearly identical for all the tests (variation of less than 10 $\Omega cm^2$), the comparison is simplified to only the intercept value at the low frequency end of the diagram. The annealed microstructure again has the highest polarization resistance whereas the quenched and centre material have the lowest resistance. Again the difference between the three other microstructures is relatively small with their values being intermediate to the other microstructures.

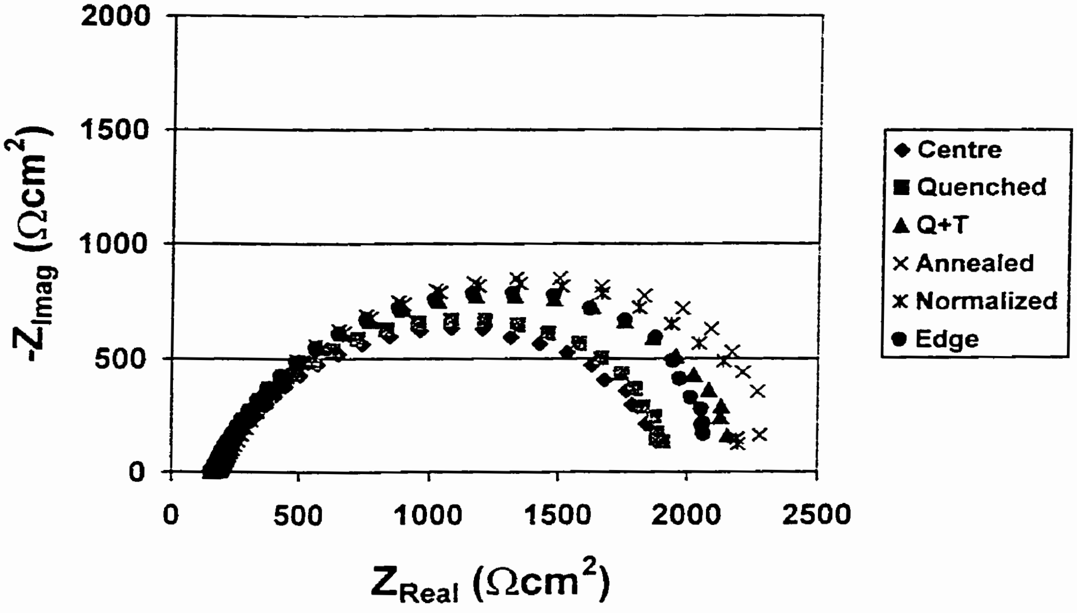

**Figure 5-9: Comparison of the various X-70 microstructures using EIS without the low frequency data**

The three corrosion test methods all showed the same general trend that annealed X-70 has the lowest corrosion rate and quenched and centre X-70 have the highest corrosion rates. The other microstructures had intermediate corrosion rates that varied slightly but generally showed that the edge material had a slightly higher corrosion rate than the Q+T and normalized microstructures. The conclusion drawn from this series of tests is that microstructure does affect the corrosion rate of X-70 linepipe in NS4. Although this conclusion has not been previously reported for this system, the microstructure affecting corrosion rates in other systems has been documented (Huang et al., 1994).

$E_{corr}$ was not a reliable indicator of the corrosion rate since the general trend was not closely followed, Figure 5-10. Although the quenched X-70 had the most positive potential and the annealed the most negative potential, the other microstructures had potentials that did not reflect their relative corrosion rates. An example is that the edge and centre X-70 had the same corrosion potential and yet their corrosion rates were different. A second case in point is that the normalized microstructure has a corrosion potential that is between the annealed and Q+T corrosion potential, yet the corrosion rate is close to the corrosion rate of Q+T. Therefore $E_{corr}$ should not be used as a discriminator for corrosion rates.

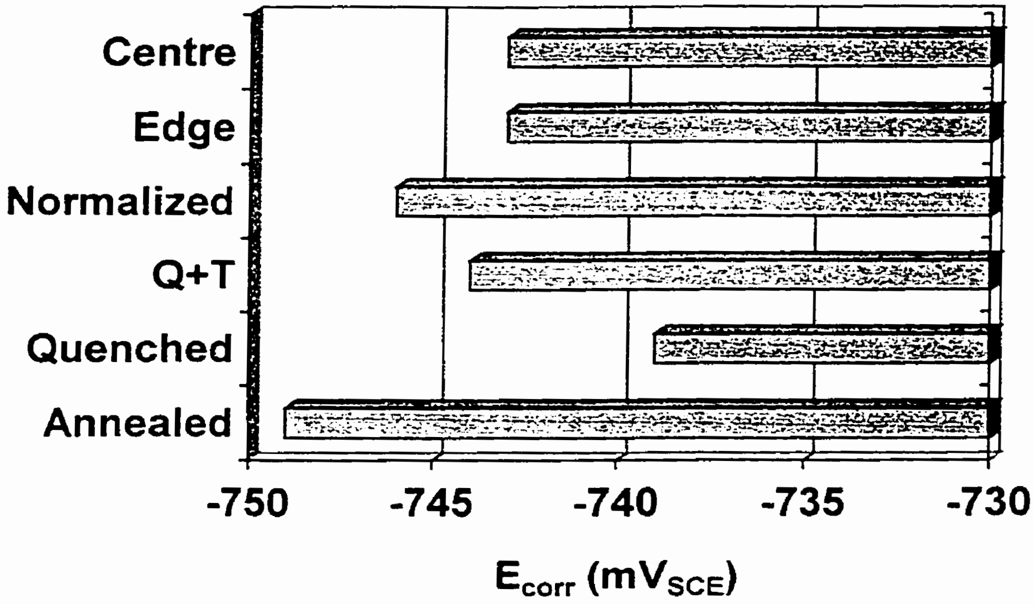

**Figure 5-10: $E_{corr}$ of the various X-70 microstructures**

### 5.1.2 Examination of the X-70 Corrosion Surface

Figure 5-11 is the corroded surface of X-70 linepipe that was immersed for 7 days in NS4 and is characterized by the light circular regions on a dark surface. This image was taken from the same specimen that showed segregation along the mid-thickness. This segregation appears to influence the appearance of the corrosion damage since the centre of Figure 5-11 is lighter in colour than the rest of the image (this effect also appears in the SEM image of Figure 5-19). An examination of one of these light regions showed that a scratch from specimen preparation remained clearly visible in the light region indicating that no corrosion has occurred and that these are cathodic regions. Also, these cathodic regions almost always had a centrally located titanium nitride (titanium nitride identified by its morphology and distinctive colour).

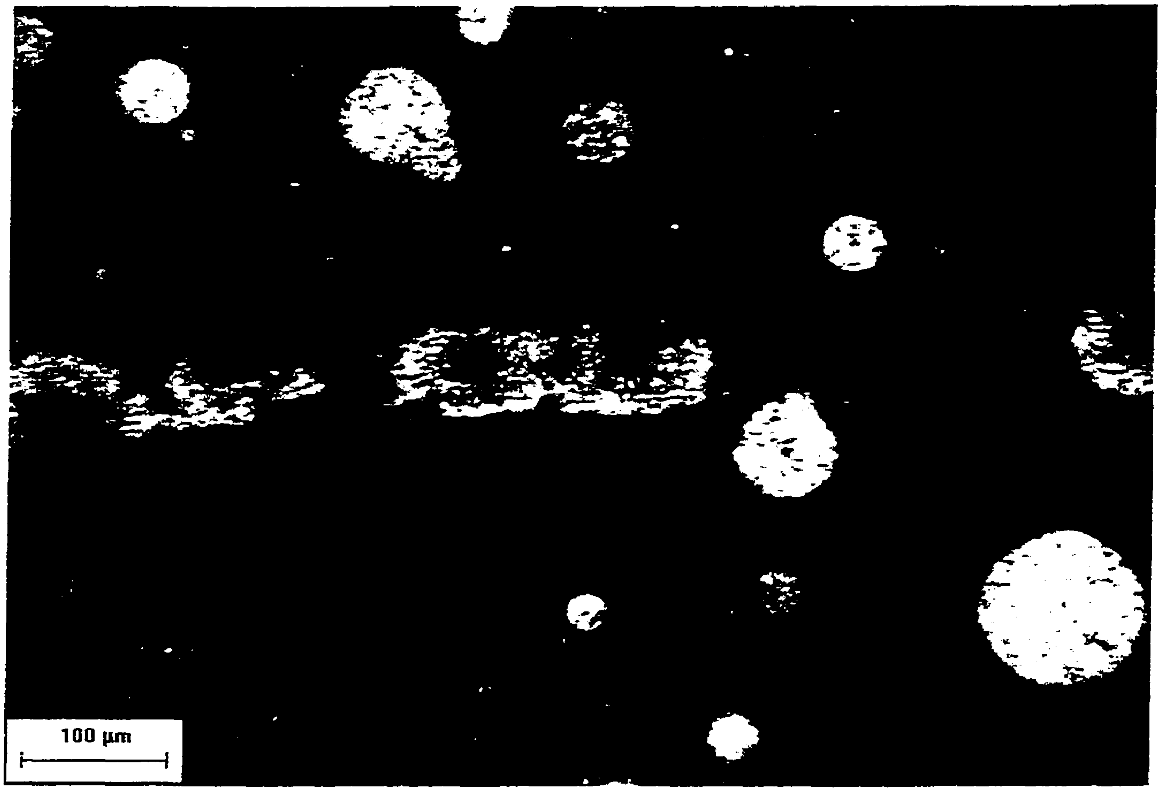

**Figure 5-11: X-70 corrosion surface after being exposed to NS4 for 7 days**

Figure 5-12 shows one of these cathodic regions as imaged in SEM. The dark spot located in the middle shows corrosion product formed on its surface (the white object) and an EDX analysis, Figure 5-13, showed that the dark spot is a titanium nitride that formed adjacent to or around a calcium sulphide inclusion. The second dark spot in the lower left hand side of the cathodic region had the same composition as the matrix and is a possible location of a previously existing calcium sulphide.

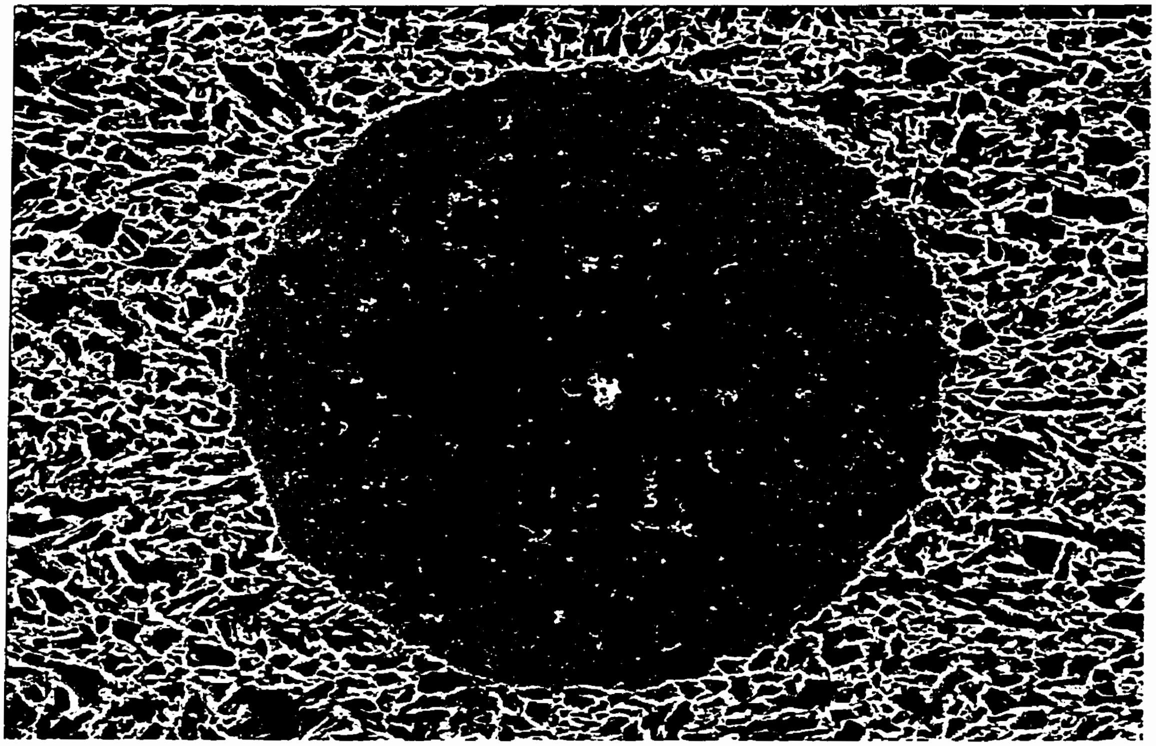

Figure 5-12: Cathodic region in X-70

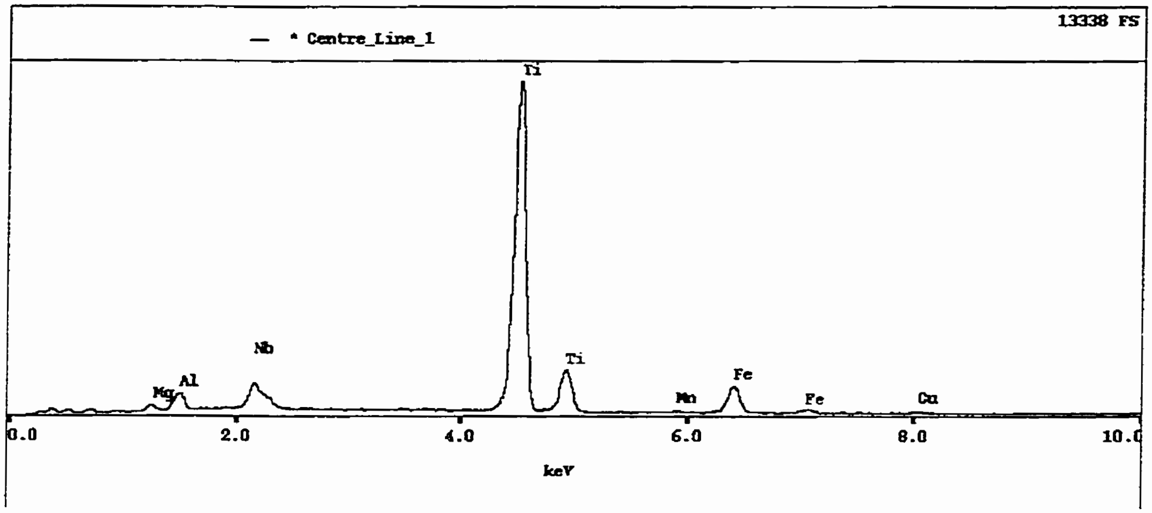

Figure 5-13: EDX analysis of the central precipitate in the previous figure

EDX analysis of many of the cathodic areas showed a titanium nitride at is centre. The influence of the titanium nitride on the cathodic region was consistent in all heat treatments and agrees with the observation made with the optical microscope that the cathodic regions almost always contained a centrally located titanium nitride.

Two hypotheses were made to explain these cathodic regions with the central titanium nitride. The first hypothesis was based on the use of minor amounts of some noble elements in alloys for corrosion protection. In these alloys, the matrix is slowly corroded away leaving a surface that is eventually rich in these noble elements and hence the surface stops corroding. The first hypothesis for the cathodic regions has two versions; there is either a fine distribution of titanium nitrides or there is a distribution of titanium that protects the surface.

To test the hypothesis of a fine distribution of titanium nitrides, an x-ray map of the region shown in Figure 5-14 was performed and is shown in Figure 5-15. The centrally located precipitate was indeed a titanium nitride nucleated on a calcium sulphide and the lower dark spot is a very small titanium nitride. However, no other titanium nitrides were detected and hence the hypothesis of a distribution of nitrides is not likely (the resolution of this method is approximately 1 micron so any nitride under this dimension would not be resolved).

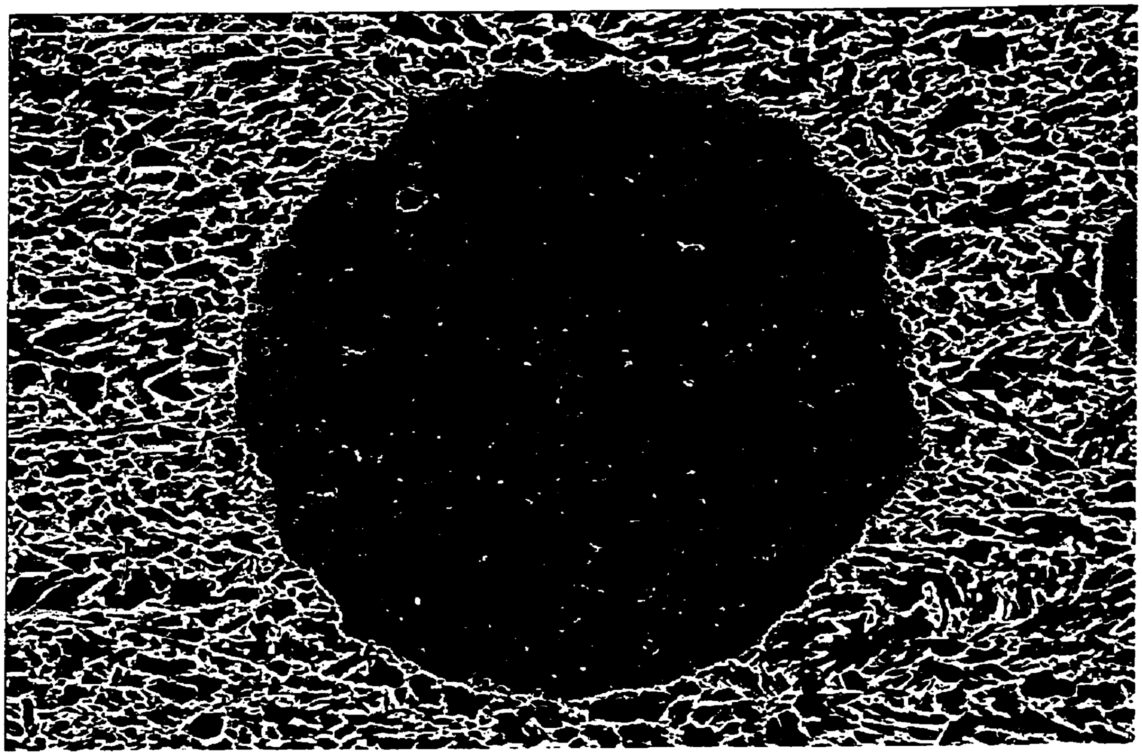

Figure 5-14: Cathodic region in X-70 used in an x-ray map

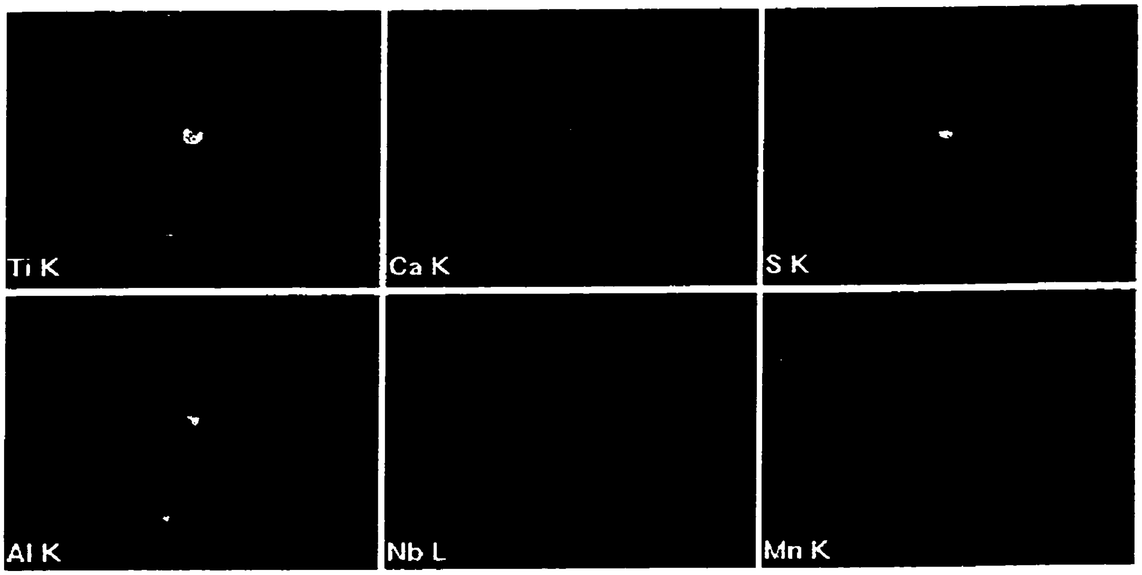

Figure 5-15: X-ray map of the region shown in the above figure

The second version of the first hypothesis is that there may be a concentration gradient of titanium around the titanium nitride and this titanium provides corrosion protection. This hypothesis was not tested and is recommended for future research.

The second hypothesis is based on a galvanic effect normally associated with sulphides. The preferential corrosion of the matrix surrounding a manganese sulphide (MnS) inclusion has also been documented (Wranglen, 1974). MnS is noble to iron, has relatively low conductivity, has low hydrogen overpotentials and is slightly soluble in most solutions creating sulphide ions that can depolarize both anodic and cathodic reactions. In terms of composition, a matrix surrounding the MnS inclusion is contaminated with sulphur and submicroscopic MnS inclusions. When corrosion tests, specifically a micro-corrosion test (MCT), are performed on steel containing MnS inclusions, the main MnS inclusion is a cathodic site for hydrogen reduction, the surrounding sulphur containing matrix is a highly active anodic site and is severely corroded and the main cathodic reaction, the reduction of oxygen occurs on the matrix not containing sulphur. The reasons that the surrounding matrix is highly corroded are:

- MnS is noble to iron so there is a galvanic effect;
- The fine dispersion of submicroscopic MnS inclusions increases the surface area between the cathode and anode; and
- A submicroscopic MnS inclusion has higher solubility creating sulphide ions that polarize the cathodic and anodic reactions.

There is a different effect for highly soluble sulphides such as calcium sulphides (CaS) (Eklund, 1970) (remember that the X-70 linepipe is calcium treated and contains CaS and not MnS). Eklund found that since CaS is easily soluble, the matrix surrounding the CaS is attacked which provides cathodic protection to the matrix around neighbouring MnS inclusions. The cathodic protection suuplied to the MnS inclusions obscures the MnS activity found in steels without the CaS inclusions. There has been no research on the effect of CaS on the corrosion behaviour of a steel that contains only CaS.

To see whether the titanium nitride was corroding or if the matrix surrounding the nitride was corroding, a X-70 steel specimen with a 600 grit surface finish was corroded for 48 hours and viewed in the SEM with its surface inclined to the beam axis. Figure 5-16 shows that there is preferential corrosion of the base metal surrounding the nitride.

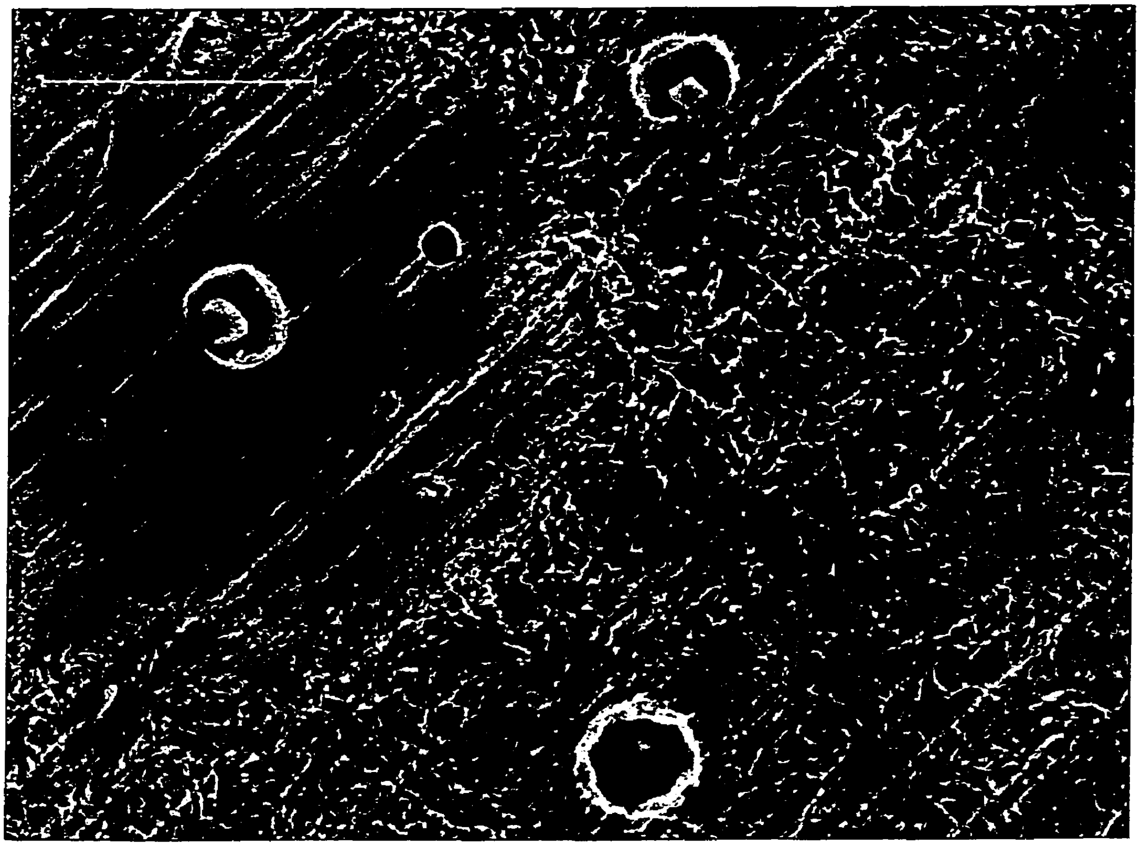

Figure 5-16: X-70 linepipe steel showing preferential corrosion of the base metal around some titanium nitrides

Wang et al. (1998) observed a phenomenon on X-65 cyclically loaded in NS4 of a circular cathodic region except that there would be a centrally located aluminate sometimes combined with calcium and sulphur. The size of the "halo" region, as they termed it, was a function of the diameter of the central pit. Their observations showed that if the inclusions composition was low in sulphur, preferential corrosion occurred in the base metal surrounding the inclusion. Inclusions with high sulphur composition showed corrosive attack on the base metal and inclusion.

There are similarities between the corroded surface of the X-65 steel in the research by Wang et al. (1998) and the corroded surface of this X-70. The major difference is that, in the X-70 steel, the centrally located precipitate is a titanium nitride rather than an aluminate. This difference is likely due to the composition with the X-65 being a ferritic/pearlitic microstructure with limited titanium nitrides due to a small amount of titanium whereas the X-70 has a large number of the titanium nitrides. Wang et al. attributed their cathodic regions to a galvanic effect and that is likely responsible for the cathodic regions of the X-70 steel as evidenced by the preferential corrosion shown in Figure 5-16. The effect can be verified in future research by investigating the corrosion characteristics of titanium nitrides and by completing the previously mentioned recommendation for the first hypothesis of measuring the titanium distribution in these cathodic regions

The circular shape of the cathodic region around the titanium nitride becomes more apparent when several titanium nitrides are adjacent to one another as shown in Figure 5-17. Here there is an overlap of the cathodic regions and a large region is protected due the close proximity of several nitrides. The higher magnification images show that there is no corrosion in any of the regions and in fact there is a faint surface preparation scratch running from the middle of the left hand side to the upper right corner of Figure 5-17d showing that there is no corrosion.

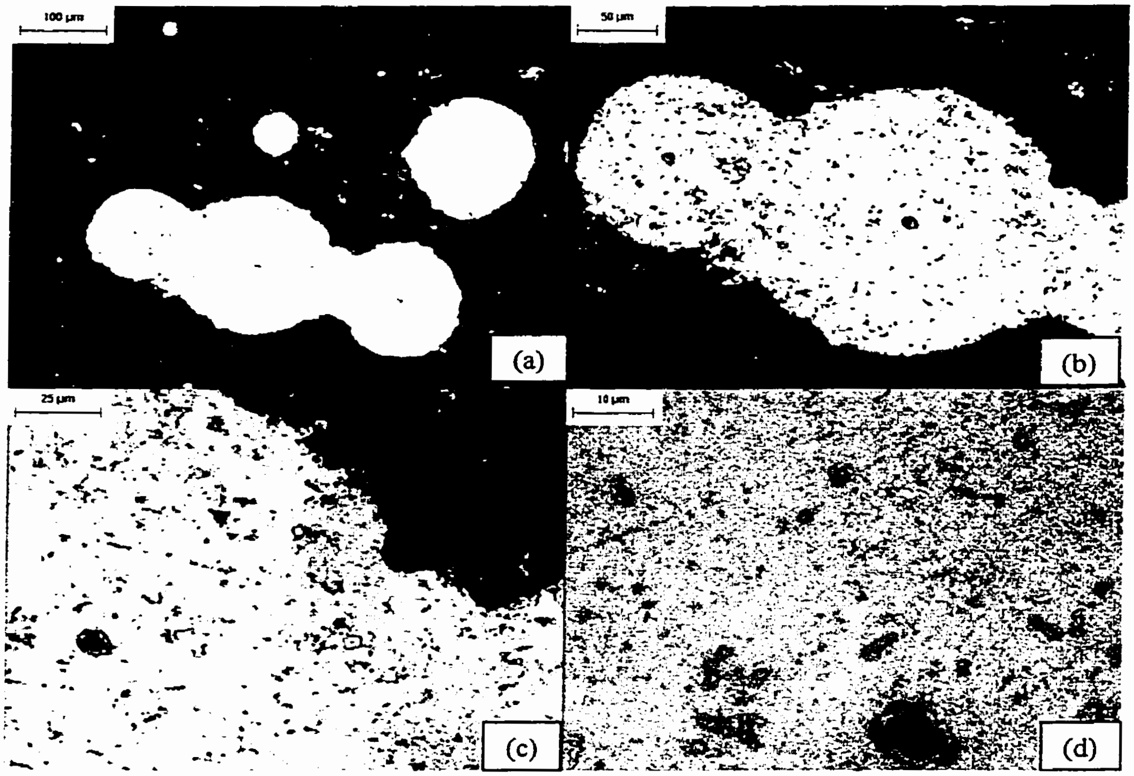

**Figure 5-17: Irregular shaped cathodic area, (a) 200x, (b) 400x, (c) 800x, (d) 2000x**

The influence of numerous nitrides on the overall cathodic region is also shown in Figure 5-14. The central titanium nitride is much larger as shown in Figure 5-15 and hence the cathodic area is much larger and appears to actually encompass the cathodic region of the smaller titanium nitride. Both this effect where a cathodic region is encompassed in another cathodic region and the overlapping of the cathodic regions to produce a non-circular region are schematically presented in Figure 5-18. This illustrates that the circular regions still exist around the nitrides, but the size and location influences the overall structure of the cathodic region.

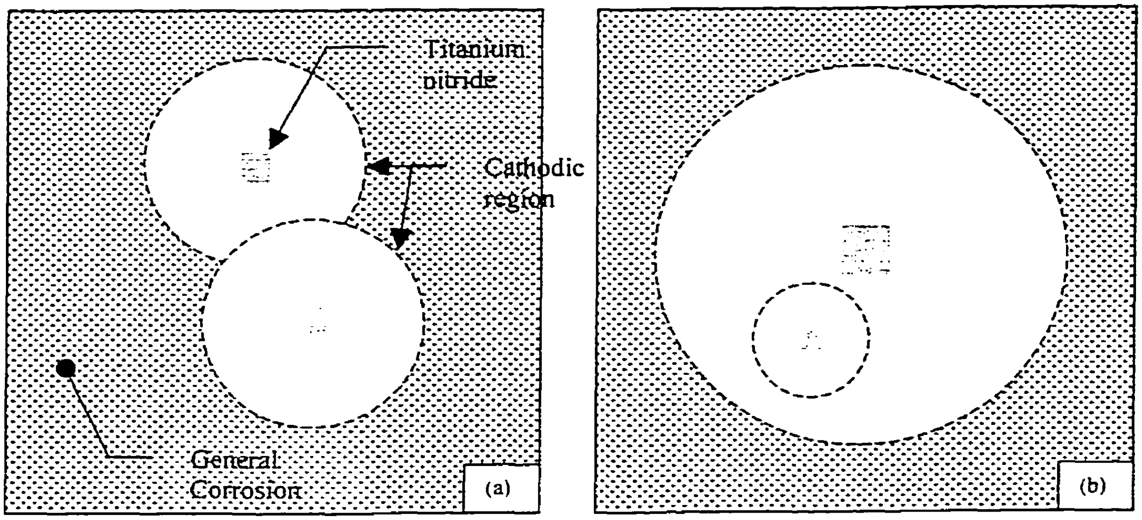

**Figure 5-18: Schematic of the interaction of numerous cathodic areas from titanium nitrides**

There was no apparent influence of the CaS inclusions on the cathodic regions as shown optically and with the SEM in Figure 5-19. These images are from the same sample that showed segregation of inclusion at the mid-thickness and these images are taken along the mid-thickness. In Figure 5-19a the inclusions are only barely visible as four dark spots across the middle of the image since CaS is highly soluble and dissolves leaving a pit on the surface. Figure 5-19b clearly shows the original sites of the inclusions. There was a calcium sulphide on the edge of a cathodic region on the right hand side of the image and this inclusion did not extend the cathodic region but rather disrupts the normal circular shape. The influence of the sulphide appears to be on the precipitation of the $FeCO_3$ corrosion product. Figure 5-19b shows that the original location of the sulphides has a different morphology for the corrosion product compared to the region where no sulphides existed (the top and bottom of the image).

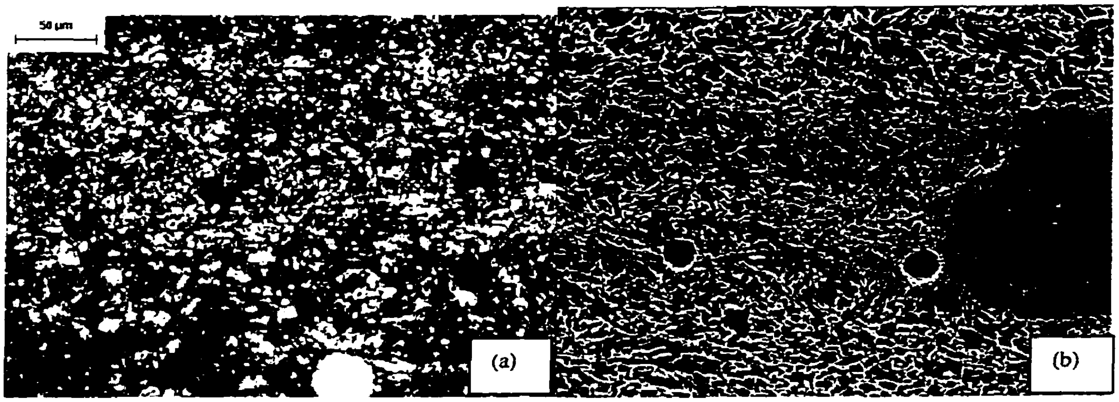

**Figure 5-19: Influence of the calcium sulphide inclusion on the corrosion surface (a) optical microscope view, the four dark spots across the middle are the original locations of inclusions (b) SEM view and the dark spots are the original location of the inclusions**

### 5.1.3 Carbon Steel

The characterization of corrosion properties of AISI 1018 and 1045 steels was performed using the same techniques as was used for the X-70 linepipe steel. The tests on the carbon steel showed the same general features as the X-70 microstructures. All of the steels demonstrated only an active behaviour and high $R^2$ values were obtained when linear regression analysis was used to determine the corrosion parameters. The tests were reproducible as demonstrated by the small difference between the maximum and minimum values attained during testing.

The polarization resistance of the carbon steel microstructure used in SCC testing is shown in Figure 5-20. Figure 5-21 uses the polarization resistance to calculate the corrosion current of the carbon steel microstructures and it is apparent that there is some difference in the corrosion rates. A discussion of these results is presented in the next sections since more results are required to draw any conclusions from these results.

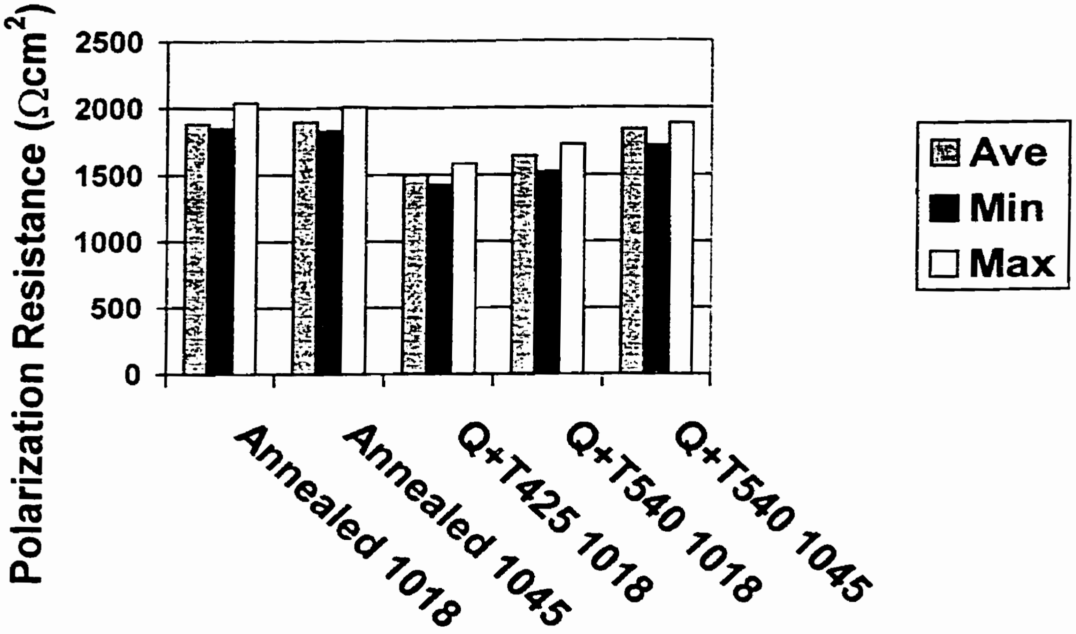

Figure 5-20: Polarization resistance for various carbon steel microstructures

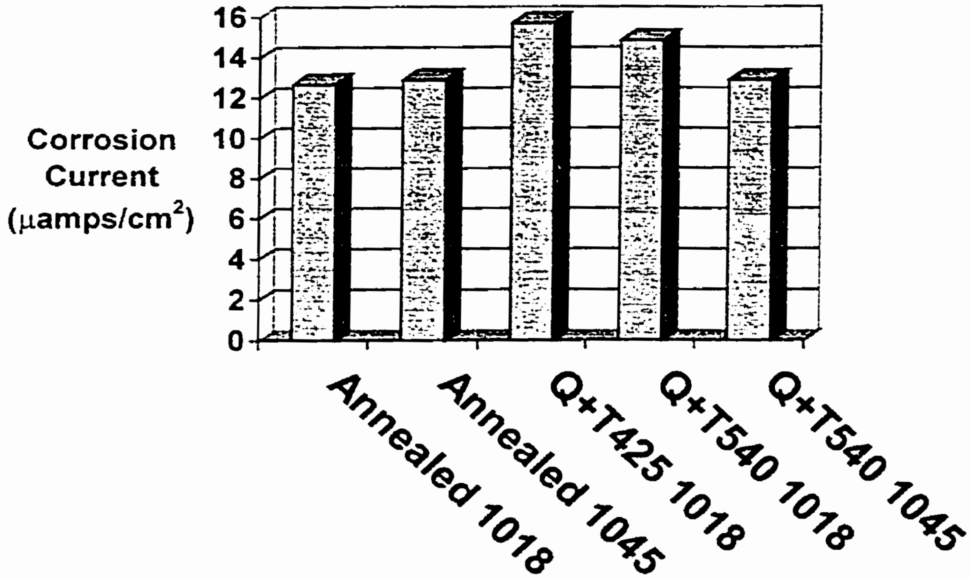

Figure 5-21:Corrosion current from polarization resistance test for various carbon steel microstructures

### 5.1.4 Corrosion Surfaces of Carbon Steel

The corrosion surfaces of the carbon steel microstructures showed similar features to the X-70 linepipe steel. Figure 5-22a shows a typical corrosion surface of carbon steel that was immersed for 7 days in the NS4 solution. There is a distinctive circular region with a central dark spot and Figure 5-22(b) shows the same feature at a higher magnification. Figure 5-22(b) shows that there is corrosion of the area outside the circular region and no corrosion inside the region. This is best exemplified by a grain boundary exposed due to corrosion found to the right of the bottom middle of Figure 5-22b, but vanishes in the circular region. The scanning electron micrographs of Figure 5-23 also show that the circular regions remain flat throughout the exposure to the corrosive environment, showing that the circular region is a cathodic region free of significant corrosion. The centralized dark spot is likely a combination of calcium aluminate, silicon oxide and calcium sulphide as deduced from the EDX analysis shown in Figure 5-24. Both the X-70 steel and the carbon steel both showed circular cathodic regions with a centralized precipitate that was a titanium nitride for the X-70 steel and a calcium aluminate/sulphide for the carbon steel. The carbon steel corrosion surface with the cathodic region is very similar to the results of Wang et al. (1998), discussed earlier, with both cases having a central aluminate/sulphide inclusion.

Figure 5-23 also has another interesting feature, that is, pearlite is distinctly visible on the corroded surface. $FeCO_3$ can form a protective barrier to corrosion and forms preferentially on cementite (Manuel, 1984). The distinct pearlite feature on the corroded surface is due to preferential corrosion of the cementite within the pearlite that creates a high concentration of $Fe^{2+}$ ions above the cementite and subsequent formation of $FeCO_3$ on the cementite protecting it from the corrosive environment.

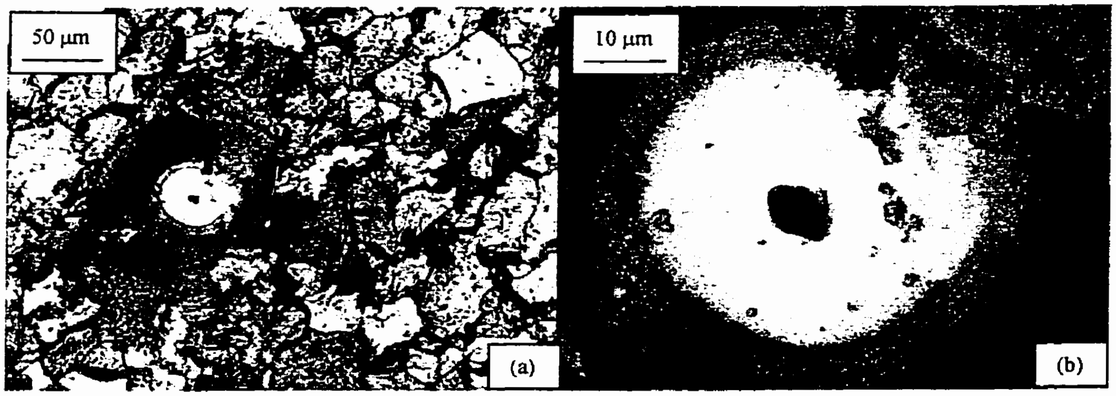

**Figure 5-22: Image of the corrosion surface of annealed 1018 carbon steel after being immersed in NS4 for 7 days**

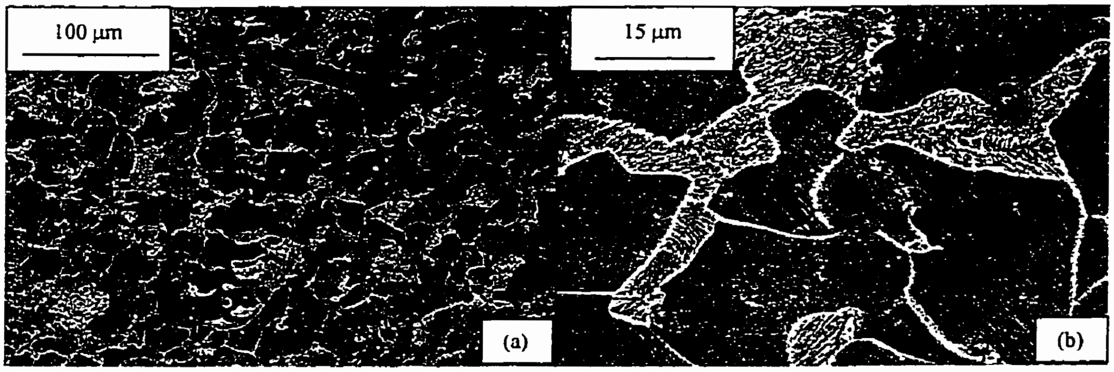

**Figure 5-23: SEM image of corrosion surface of 1018 carbon steel immersed in NS4 for 7 days**

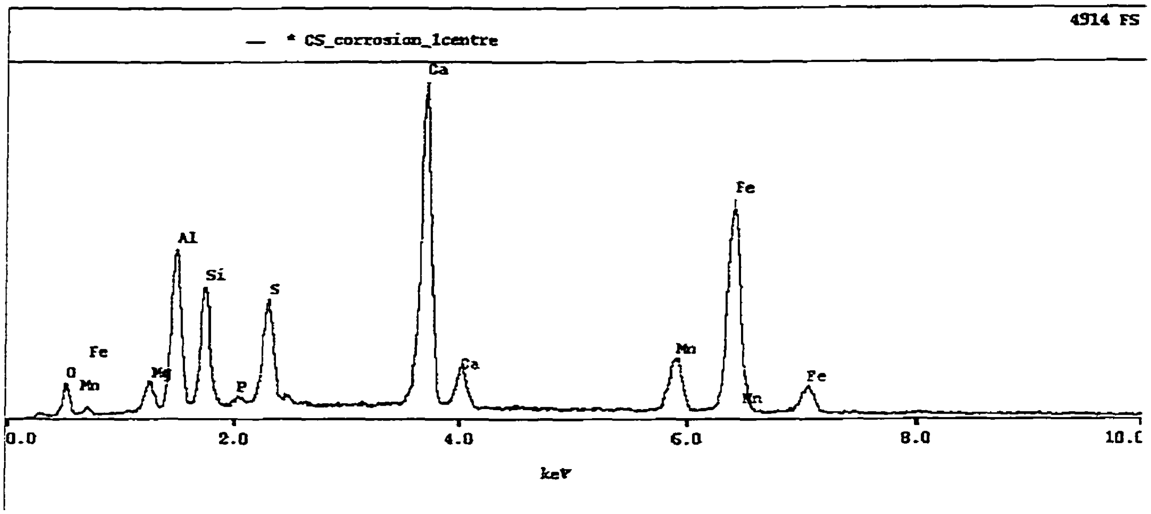

**Figure 5-24: Composition of inclusion in the previous figure**

### 5.1.5 Effect of tempering on the corrosion of carbon steel

To understand the results presented in Figure 5-20, the effect of tempering was investigated by testing 1018 steel tempered at increasing temperatures. As shown in Figure 5-25, the quenched 1018 microstructure had the lowest polarization resistance and its polarization resistance increased with the tempering temperature. The minimum and maximum values are not included in Figure 5-25 and in the remaining results to avoid clustering the data. The range in the results for the individual microstructures was small compared to the differences between the microstructures. The difference between the Q+T425°C and Q+T540°C resistance was small since the microstructures differed only slightly with the Q+T540°C having more ferrite and carbides than the 425°C temper. There is a further increase in polarization resistance in the 675°C tempered microstructure due to the formation of equiaxed ferrite and substantial grain growth.

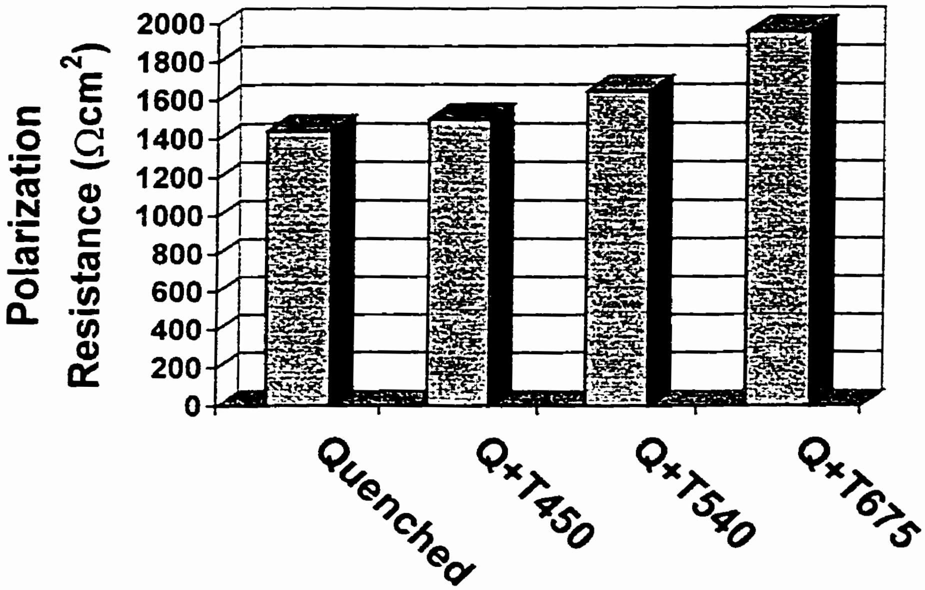

Figure 5-25: Polarization as a function of tempering temperature for 1018 carbon steel

To see the effect of the carbide distribution, it is useful to compare the 1018 steel with the 1045 steel, both quenched and tempered at 540°C. From Figure 5-20, the 1045 steel has a polarization resistance that is about 8% greater than the 1018 steel. If we assume that the tempering temperature controls the carbide size, then an increase in the carbon content should result in a greater distribution of these equally sized carbides, resulting in an increase in polarization resistance. However, that assumption of the microstructure requires a detailed investigation for validity.

Although the 1018 carbon steel microstructures covered in Figure 5-20 show that microstructure does influence the corrosion rate, the two 1045 steel microstructures do not support this conclusion since their polarization resistances are basically the same. This peculiar result can be clarified by noting that the Q+T675°C and annealed 1018 steel microstructures have the same polarization resistance while the other 1018 steels tempered at other temperatures have different polarization resistances. Hence, it is likely that the 1045 steel also has corrosion rates that are a function of the microstructure and this would have been shown if a tempering temperature other than 540°C were used (i.e.: like 425°C or 675°C that was used for the 1018 steel).

## *5.2 Effect of Microstructure on Corrosion in NS4*

### 5.2.1 Grain Size

Referring to the X-70 pipeline steel corrosion results of section 5.1.1, there was a difference in the corrosion rate of the annealed and normalized X-70 in which the large grained annealed microstructure had a lower corrosion rate than the smaller grained normalized microstructure. To test the grain size trend, the X-70 steel was austenized at a higher temperature and furnace cooled but the grain size did not increase substantially likely due to the titanium nitride restricting austenite grain size. Attempts were also made to air cool the X-70 steel at a higher rate (using forced air) to produce a microstructure with a grain size smaller than the normalized, but the resulting microstructure had substantial quasi-polygonal ferrite and some acicular ferrite, which is a different microstructure compared to the equiaxed normalized and annealed microstructures.

Although the X-70 steel could not produce a microstructure with varying grain size, heat treating 1018 carbon steel produced a ferritic/pearlitic microstructure with varying grain size as shown in Table 4-7. The effect of the grain size on the corrosion resistance is shown in Figure 5-26 with an increase in the grain size increasing the polarization resistance. Thus both the carbon steel and X-70 steel show that increasing the grain size decreases the corrosion rate. This might have played a role in the high polarization resistance of the Q+T675 1018 since the ferrite grain size was larger than the lower tempering temperatures.

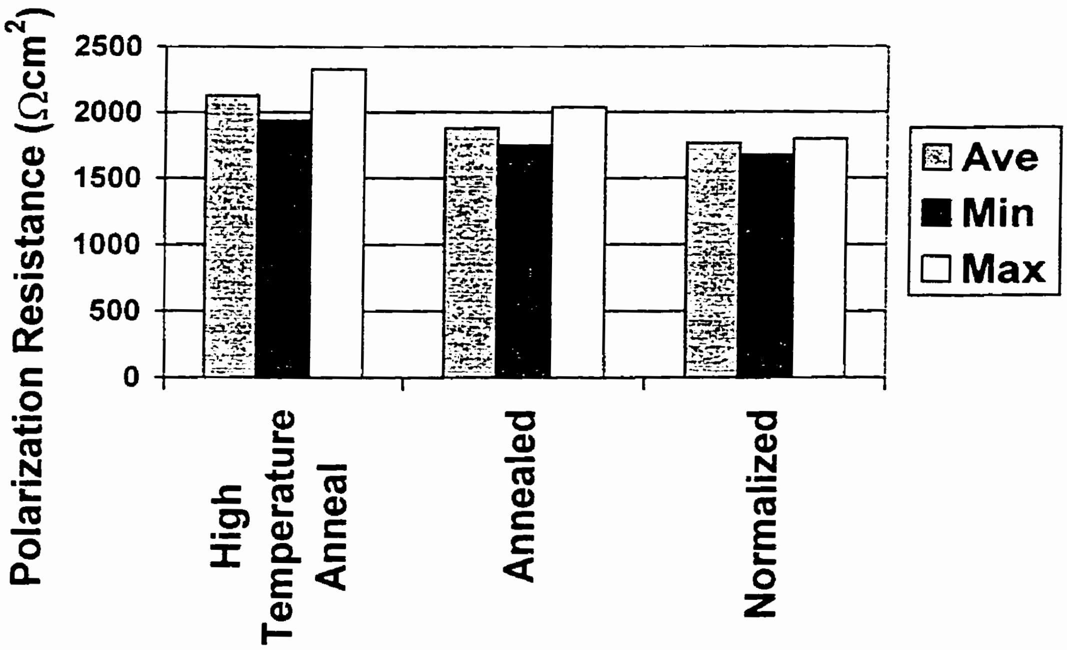

**Figure 5-26: Effect of grain size on the polarization resistance of 1018 carbon steel**

### 5.2.2 Inclusions and Retained Austenite

The distribution of the retained austenite and inclusions in X-70 linepipe steel increased gradually towards the mid-thickness of the sample whereas the grain size reached its full size relatively close to the surface. By sectioning a centre X-70 sample close to the surface (but far enough from the surface that the grains were at full size) and at mid-thickness, Figure 5-27, corrosion samples were made that had the same grain size but different amounts of inclusions and retained austenite. Microstructural evaluation of the samples showed that the surface mid-thickness specimen contained more retained austenite and inclusions while the grain size was basically identical.

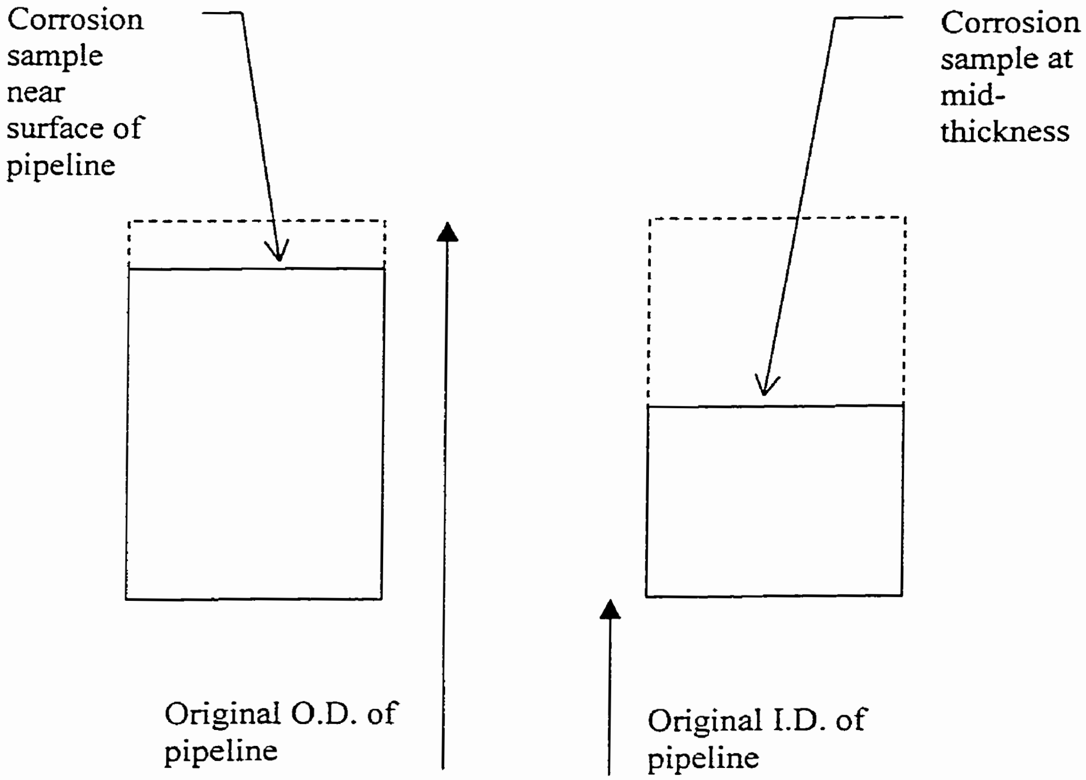

**Figure 5-27: Schematic showing the sectioning of the pipeline to get samples with varying amounts of retained austenite and inclusions**

There was an appreciable difference in the corrosion rate due to the inclusions and the retained austenite (Figure 5-28), with the mid-thickness sample showing a corrosion rate that was about 10% greater. The individual influence of the inclusions or the retained austenite was not investigated.

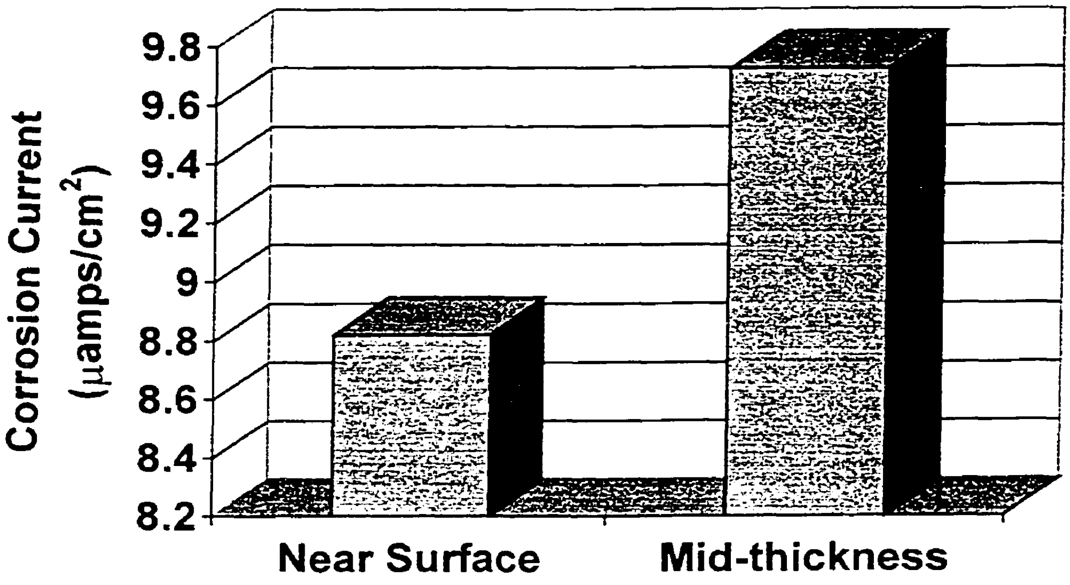

**Figure 5-28:** Affect of inclusions and retained austenite on the corrosion current

The difference in the corrosion rate between the centre and edge X-70 linepipe (Figure 5-4) can now be related to the above results of other tests. The difference between the microstructures of the edge and centre X-70 was the centre X-70 has a smaller grain size, more inclusions and more retained austenite. From section 5.2.1, if the polarization resistance is a function of the grain size, with a decreasing grain size having a decreasing polarization resistance, the centre X-70 should have a lower polarization based on its smaller grain size. However, the difference in grain size is small and likely does not account for the total difference between the two microstructures. The other part of the difference in the polarization resistance between the two locations is due to the greater proportion of inclusions and retained austenite in the centre X-70. As was shown in this section, an increasing amount of inclusions and retained austenite will cause a decrease in the polarization resistance.

The increased corrosion resistance of pearlite was shown early in Figure 5-23 with the pearlite being less corroded than the surrounding ferrite grains. The effect of grain size can also be used to explain the role of pearlite in NS4. Figure 5-20 showed that annealed 1018 and 1045 steels had the same polarization resistance. Based on grain size, it was expected that the 1045 should have had a lower resistance since its grain size was appreciably smaller and this is detrimental to the resistance. Therefore it can be concluded that the additional amount of pearlite in the 1045 steel increases the corrosion resistance and compensates for the smaller grain size.

### 5.2.3 Cold Work

The role of cold work on the corrosion rate is dependent on the material environment combination as shown by France (1970) and also proposed by Huang and Shaw (1992). Before an investigation of the effect of cold work on the corrosion rate, the relative amount of plastic strain existing in the pipeline had to be gauged to determine how much plastic strain would have to be added to see a noticeable effect. The centre X-70 material was stress relieved at three different temperatures for various time periods and subsequent hardness tests were performed to see if a drop in hardness occurred. As shown in Figure 5-29, there was no drop in the hardness, indicating that the material is essentially in a low stress state. These results were in agreement with Wiskel (1999) who estimated the plastic strain to be approximately 1% based on the small plastic strains measured on small diameter pipeline subjected to a much greater deformation process.

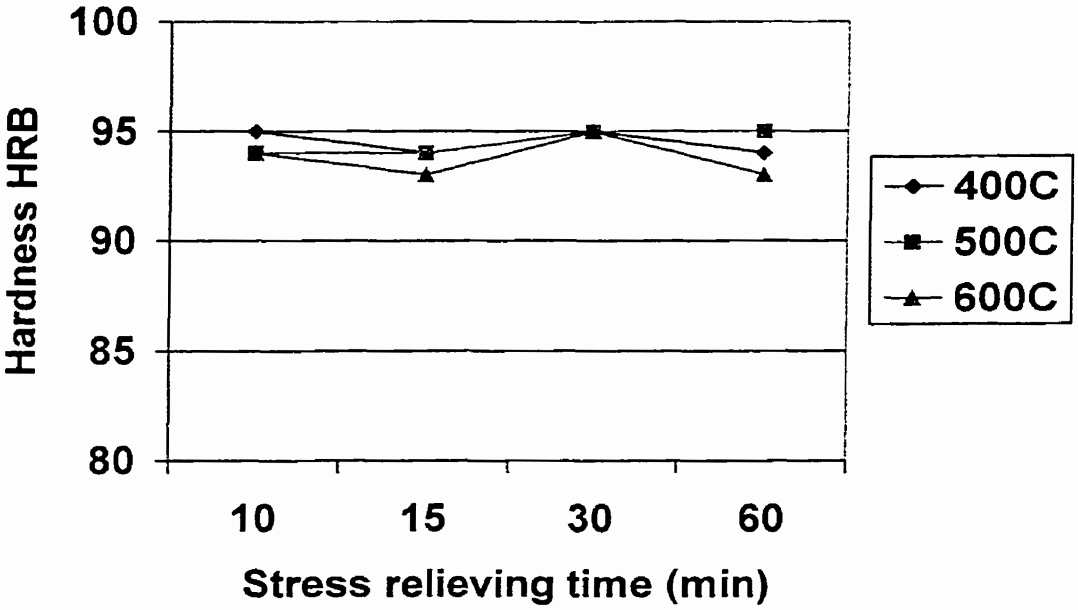

Figure 5-29: Effect of stress relieving temperature and time

Polarization resistance increased with an increasing amount of cold work as shown in Figure 5-30. To check this result, annealed X-70 was also cold rolled using the same procedure and the polarization resistance also increased with an increasing amount of cold work (Figure 5-31). Another test was performed to check the validity of the original cold work result by stress relieving the 40% cold worked samples for 30 minutes at 500°C. As shown in Figure 5-23, the stress relief lowered the polarization resistance to a value approximately the same as the original material.

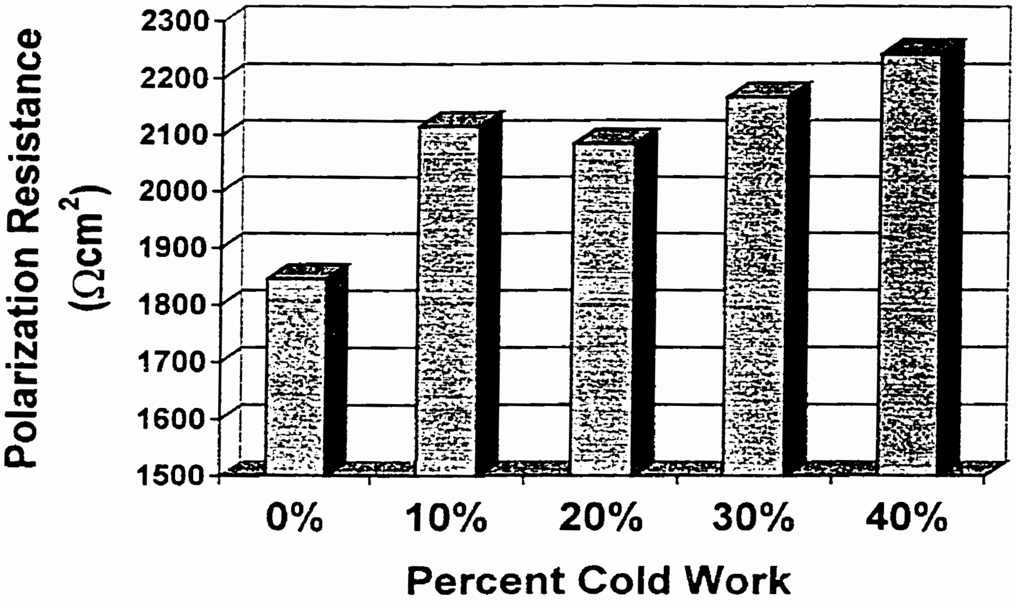

Figure 5-30: Effect of cold work on the corrosion current of centre X-70 linepipe

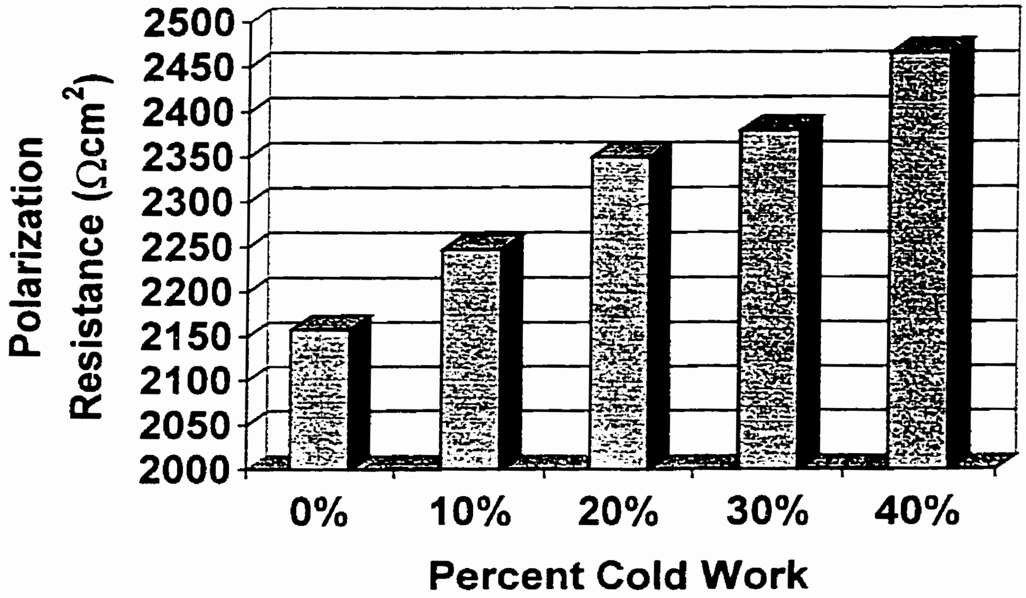

Figure 5-31: Effect of cold work on the polarization resistance of annealed X-70 linepipe

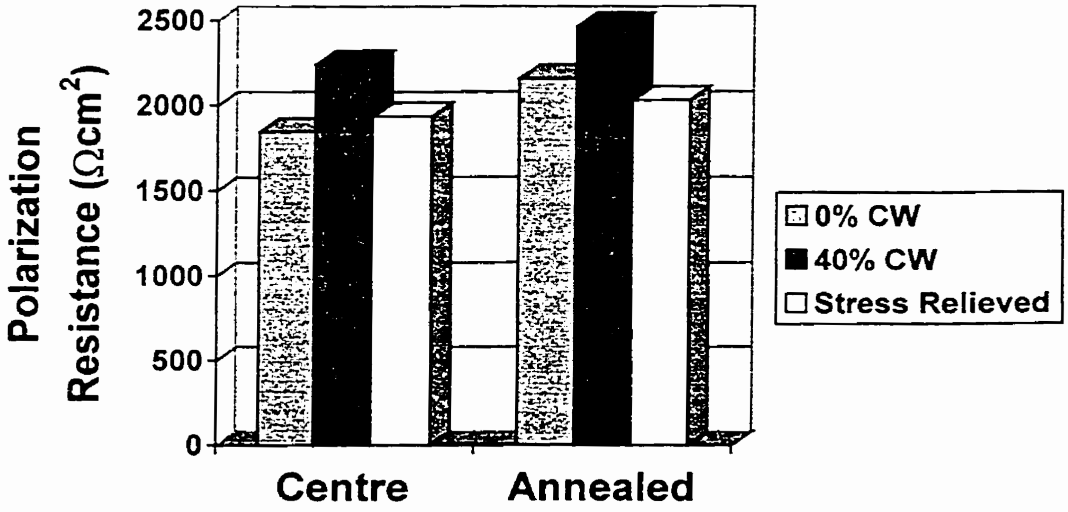

Figure 5-32: Effect of stress relieving a 40% cold rolled X-70 linepipe

An increase in the corrosion rate with increasing cold work is normally attributed to an increase in the amount of strain energy allowing easier dissolution or lower hydrogen overvoltage on specific sites generated during the deformation process. Conversely, a decrease in the corrosion rate as a result of cold working is more difficult to explain but may affect the work function or the adsorption process, which both affect the exchange current for hydrogen, $i_o(H^+/H_2)$ (Tomlinson and Smith, 1983). The exchange current density for the data found in this investigation was found by interpolating the cathodic Tafel line to the equilibrium potential of $H^+/H_2$. The effect suggested by Tomlinson and Smith was not found for X-70 steel in NS4 with $i_o$ fluctuating around $2.3\text{x}10^{-6}$amps/cm$^2$ for centre X-70. However, there was a slight increase in the cathodic Tafel constant from 0.244 for the as-received to 0.252 for the 40% CW sample. Recalling that $\beta_c=2.3RT/\alpha nF$, it appears that cold working may affect the $\alpha$ factor, which fractions the forward and reverse ionization reactions.

In terms of the corrosion results already attained, there was an influence in the amount of pearlite increasing the corrosion resistance of annealed 1045 compared with normalized 1018. The cementite in the pearlite was seen in Figure 5-23 to remain un-attacked by the corrosive environment due to the formation of a protective $FeCO_3$ layer. It is possible that the cold worked surface provides more sites for the precipitation of the $FeCO_3$, thus impeding the corrosion process. This is partially supported by the EIS data from the corrosion testing shown in Figure 5-33. Here the low frequency data for the as-received material shows some scattering then a drop in the data towards the real axis (the scatter is similar to that shown in Figure 5-3). The 40% cold worked and the stress relieved X-70 steel have a definite beginning of a second loop indicating a slightly different surface condition. The EIS data is far from conclusive and this effect requires more investigation.

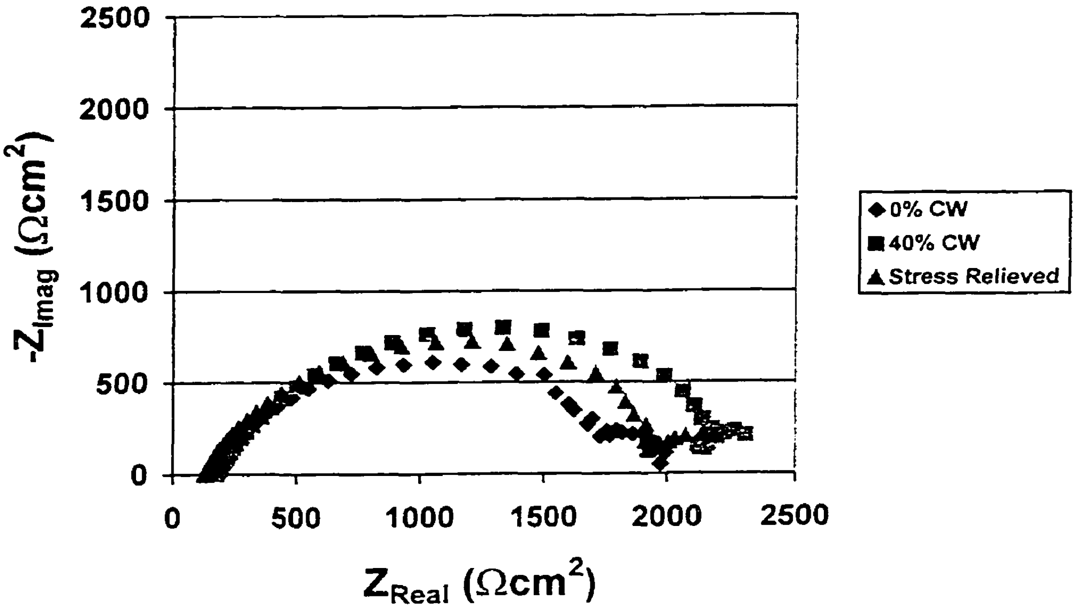

Figure 5-33: Comparison of the EIS for 0% and 40% cold worked and a stress relieved 40% cold work centre X-70 linepipe

The reason that cold work decreases the corrosion rate remains uncertain. Cold rolling can induce a variable state of strain throughout the specimen thickness (this decreases with an increasing amount of cold work) which may influence the results. A recommendation will be made to study the effect of cold work induced by tensile straining, which will provide a uniform state of strain.

### *5.3 Surface Roughness*

Based on Figure 5-16, it is suspected that the surface finish of the corrosion sample plays a role in the corrosion process. The titanium nitride in the upper middle portion of Figure 5-16 has a small amount of corrosion initiating in this generally un-corroded region. The corrosion appears to be initiated by the ridges that were left behind during the surface preparation.

Figure 5-34 shows that the polarization is a function of the surface finish with an increase in the surface roughness decreasing the polarization resistance. Based on the observation discussed above where the corrosion initiated on a surface discontinuity, these results were expected since the 240 grit final surface preparation will contain far more severe discontinuities than the other surface finishes. Reinforcing the conclusion that the corrosion potential is not a reliable method of determining the relative corrosion rate, the corrosion potential of the 240 grit surface finish was approximately the same as the 600 grit surface finish.

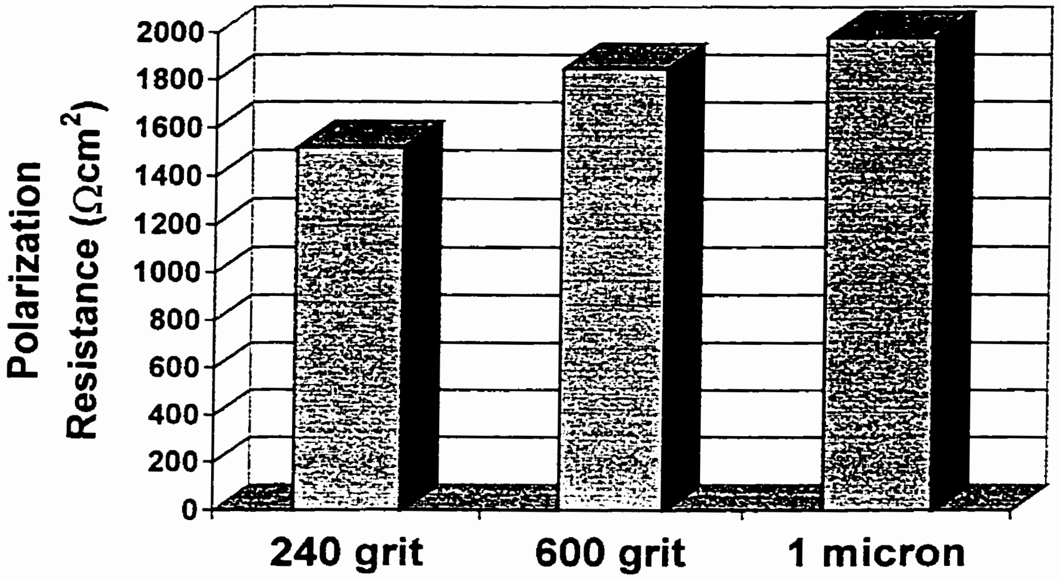

**Figure 5-34: Effect of surface finish on the polarization resistance of centre X-70**

### *5.4 Hydrogen*

There are different roles of hydrogen in the corrosion process other than being a possible product of the cathodic reaction. Absorbed hydrogen can also lead to the breakdown of passive films on stainless steels (Yang et al.. 1999) or accelerate corrosion processes (Gu et al., 1999). Although the production of hydrogen during a corrosion process is small, hydrogen can accumulate at the tip of a crack and possibly increase the local hydrogen concentration to a harmful level. As mentioned in section 2.8.9, Gu et al. (1999) suspected that the corrosion rate would be increased due to several factors including the interaction between stress and hydrogen. This hypothesis was not tested, however. Rather than test a stressed sample, this investigation tested the interaction of strain and hydrogen on the corrosion process by performing corrosion tests on as-received and 40% cold worked X-70 steel that were charged with hydrogen.

The difference in the effect of hydrogen on centre X-70 linepipe and a 40% cold worked centre X-70 specimen was investigated by holding the sample for 24 hours at a potential of $-1.1$ $V_{SCE}$ (about 450 mV cathodic to the open circuit potential) and then a fast potentiodynamic scan was used to find the corrosion rate. During the charging there is a generation of hydroxide ion ($OH^-$) that increases the pH and in order to maintain the proper pH the purge gas composition was increased to 20% $CO_2$/80% $N_2$ and the flowrate adjusted.

Figure 5-35 shows that hydrogen increased the corrosion rate for both specimens. However the percent increase for the 0% cold worked X-70 was only about 10% while the 40% cold worked X-70 increased by 20%. The cold work will affect the absorbed hydrogen in two ways (Xie and Hirth, 1982): 1) the diffusivity decreases, 2) the number of hydrogen traps increases. The effect are inter-related since the cold work increases the number of dislocations, which trap hydrogen, and as a result of increased trapping the diffusivity of hydrogen decreases. Here in the cold work specimen, the hydrogen charging of the specimen caused approximately the same amount of hydrogen to be generated on the surface since the total charge during the charging time was approximately the same, but the increased dislocation density trapped more hydrogen near the surface and increased the corrosion rate. To fully examine the effect of the hydrogen, a detailed investigation that examines the amount of cold work, the diffusivity, the charging current and the trap density which is recommended.

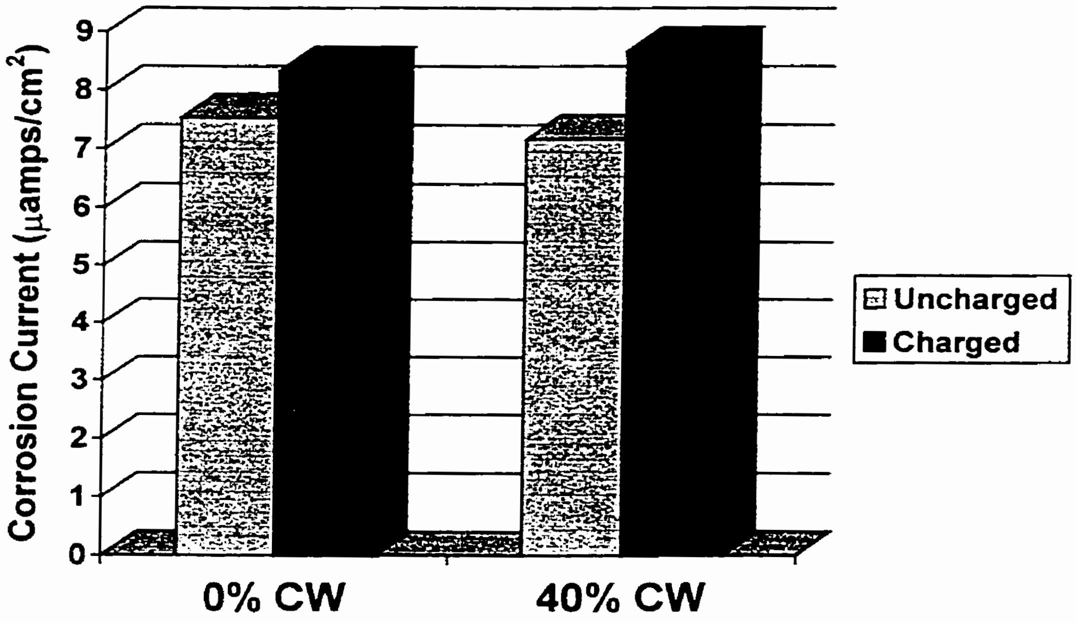

Figure 5-35: Effect of hydrogen on an as-received and cold worked X-70

# Chapter 6 SCC Results and Discussion

The slow strain rate test is a rapid method of analyzing different variables that affect SCC. Tensile specimens are pulled to failure in both air and in a SCC causing environment and then a ratio is used to compare the severity of the SCC. For instance, if the yield strength is decreased due to SCC, the ratio of the yield strength in the SCC causing environment to the yield strength in air, $\sigma_{y,\,SCC}/\sigma_{y,Air}$, will indicate the severity of the SCC. The choice of the failure ratio used to determine the severity of the SCC is not limited to the strength, but can be elongation data, reduction of area or time to failure. The magnitude of the failure ratio indicates the SCC severity with a decreasing value indicating more severe SCC. Based on years of development of this test method, typically a ratio <0.85 indicates that SCC has occurred.

SSRT was performed on the various X-70 microstructures to determine if microstructure has an affect on SCC and to determine what microstructural variables increase or decrease SCC resistance. Testing was also completed on the carbon steel microstructures to confirm if microstructure has an affect on SCC resistance.

### *6.1 X-70 Pipeline Steel*

Figure 6-1 compares the stress versus strain data for edge X-70 tested in air and in NS4. The two curves are basically identical up to the ultimate tensile strength and then there is a faster decline of the stress with increasing strain for the specimen in NS4 compared to the test completed in air. This figure is not a typical situation, normally there is less of a difference between the elongation and this situation was presented for its clarity of data.

If the elongation ratios for this data are used to compare the data a failure ratio of 0.88 is attained indicating slight SCC. However, a comparison of the reduction of area shows that there is a significant difference in the ductility (Figure 6-2) and hence the reduction of area ratio was used as the indication of SCC.

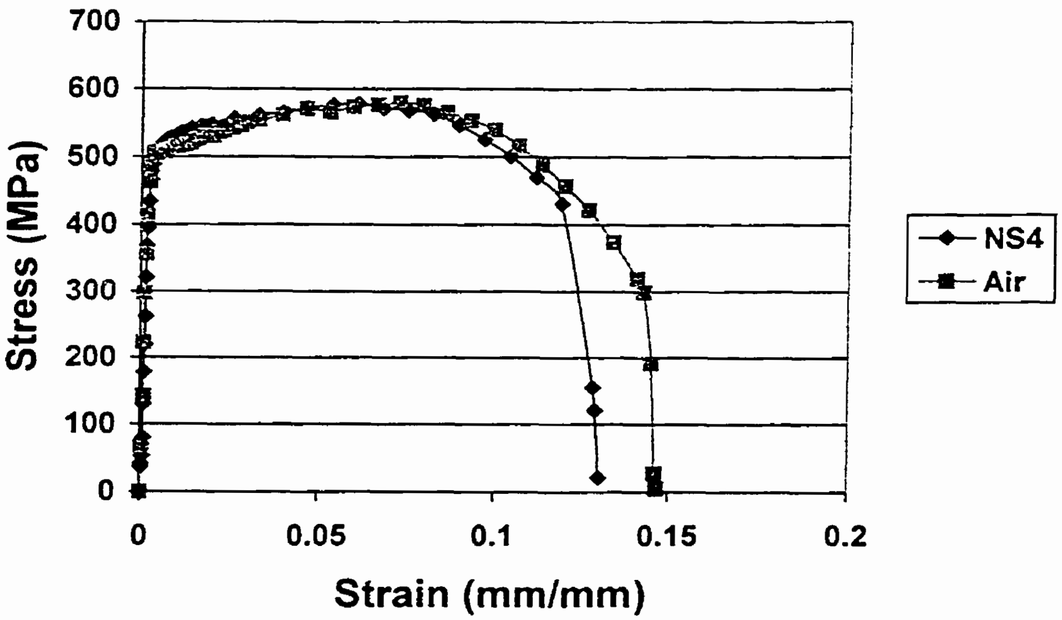

**Figure 6-1: Stress strain curve for edge X-70 tested in air and NS4**

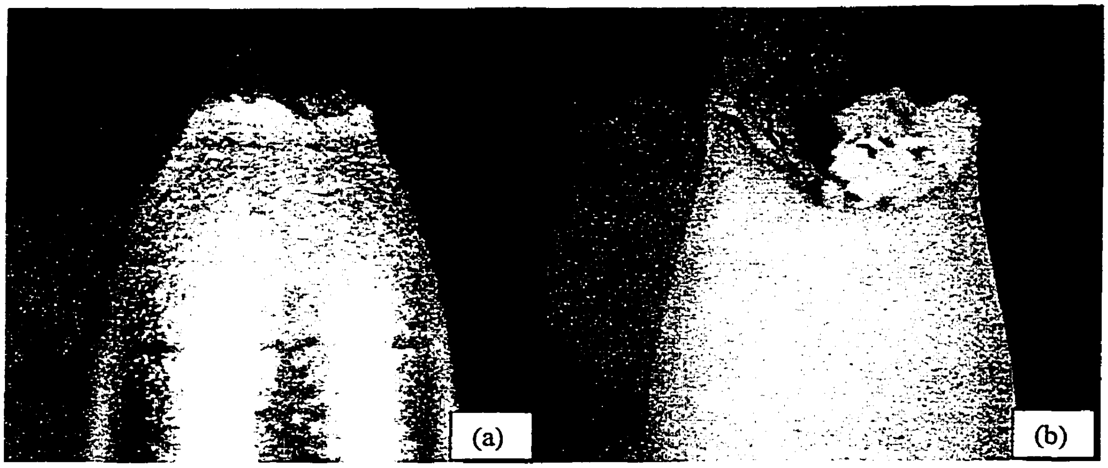

**Figure 6-2: Images of the failed edge X-70 specimen indicating the loss of ductility in the NS4 environment, (a) specimen failed in air, (b) specimen failed in NS4**

Figure 6-3 shows the results of the SSRT for the various X-70 microstructures along with error bars to indicate the small range in results for each microstructure. The quenched and the centre X-70 had the least resistance to near-neutral-pH SCC as indicated by having the lowest failure ratios. Conversely the annealed X-70 had greatest resistance to SCC with a failure ratio of 0.84. The other microstructures had intermediate failure ratios with the Q+T X-70 showing more resistance to the SCC than the other microstructures. The variation in the severity of the SCC with a variation in the microstructure indicates that SCC resistance is a function of the microstructure, and this agrees with the conclusions of other researchers (Lopez et al., 1996). Although this is conclusive from these SSRT, other test methods should be used to confirm these results.

The orientation had no effect with centre X-70 having failure ratios of 0.67 for the transverse and longitudinal orientations. Parkins et al. (1994) tested the orientation effect by testing longitudinal and transverse orientations of X-65 in dilute bicarbonate solutions with no $CO_2$ purge gas. There was no obvious effect of the orientation in terms of the %RA failure ratio but the transverse specimens tended to develop more cracks and cracks outside the necked region in several different testing conditions.

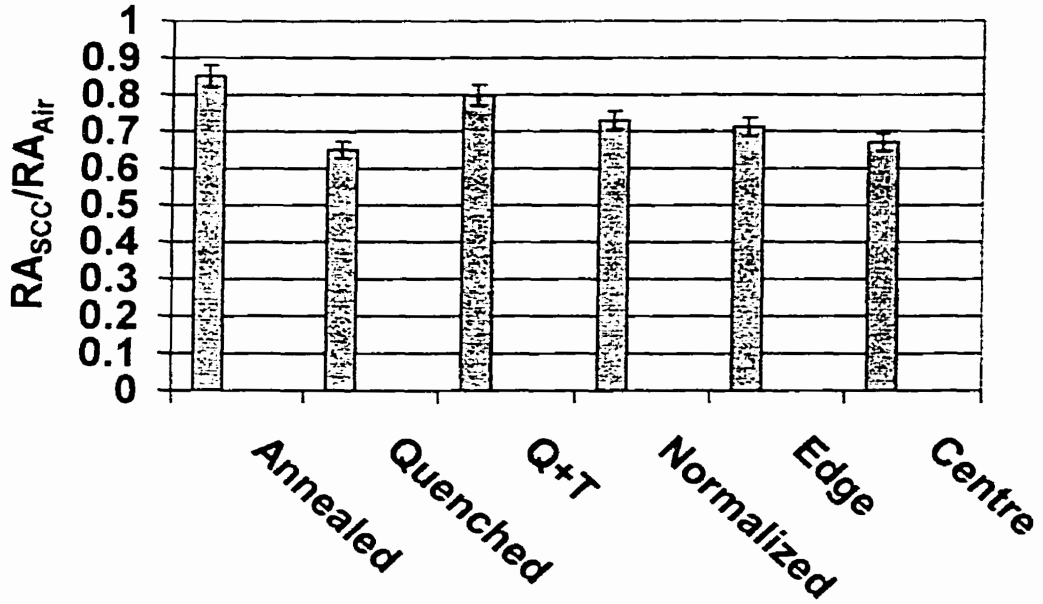

Figure 6-3: SCC performance of X-70 linepipe in NS4

The annealed and normalized microstructures have similar microstructures in that they are both ferritic/pearlitic but there is a difference in grain size with the annealed microstructure having the larger grain size. Comparison of the SCC results shows that the annealed X-70 has less severe SCC (higher failure ratio than the normalized X-70) indicating that the severity of the SCC decreases with increasing grain size. Comparing the edge and centre SCC results, centre X-70 with the smaller grain size, more inclusions and more retained austenite has more severe SCC. This result reinforces that grain size may play a role in the severity of the SCC since the centre X-70 has a smaller grain size, but the role of the greater amount of inclusions and retained austenite in the severity of the SCC was not investigated. The above results do indicate that grain size has a role in the severity of the SCC, but further tests are required with a larger range of grain sizes to confirm these results.

Figure 6-4 superimposes the polarization resistance of the X-70 microstructures onto the SCC results. There is an obvious similarity in the results suggesting that corrosion plays an important role in the near-neutral-pH SCC mechanism. The same type of similarity would have been obtained if any of the corrosion tests were used in the comparison since they all led to the same conclusion.

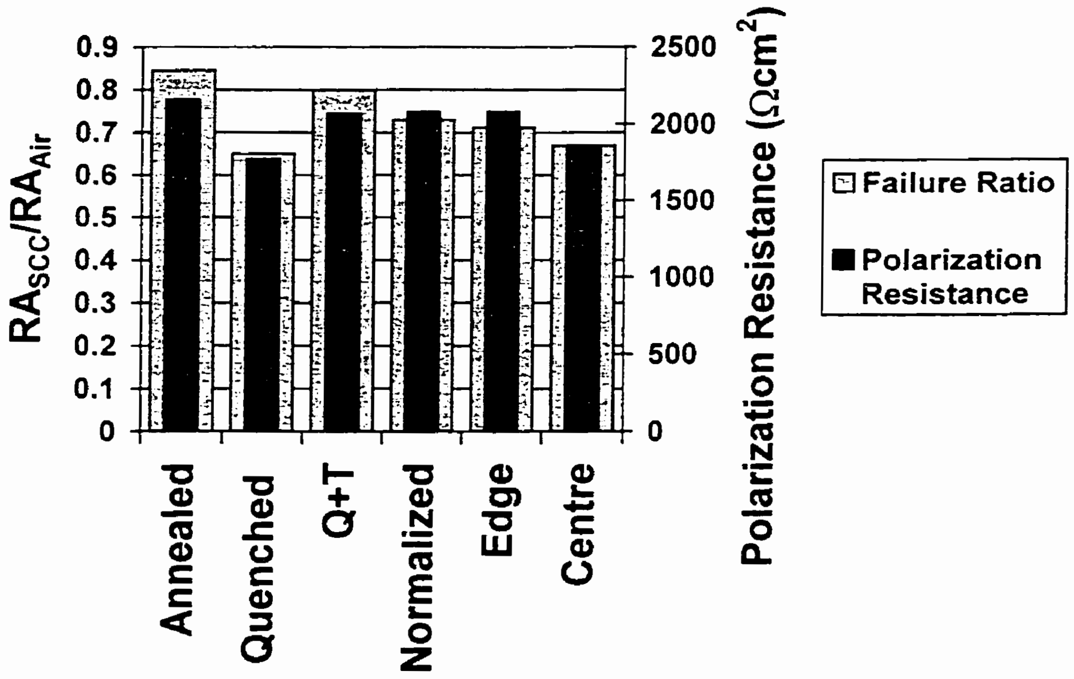

Figure 6-4: Polarization resistance superimposed on the SCC results

The relationship shown in Figure 6-4 between the corrosion data and SSRT results indicates that the mechanism of near-neutral-pH SCC is an anodic dissolution mechanism (the higher the corrosion rate, the more severe the SCC). This agrees with the two mechanisms that have been proposed for near-neutral-pH SCC by Gu et al. (1999) and Wang et al. (1998). However, further testing is required to determine which of these mechanisms is more likely.

The susceptibility of steels to sulphide stress cracking (SSC) is thought to be a function of the hardness of the steel with steels under HRC 22 being resistant to SSC. In order to investigate a relationship between near-neutral-pH SSC and hardness, the inverse of hardness (inverse of hardness is used since the hypothesis is that a higher hardness should result in a lower SCC failure ratio) is superimposed on the SCC results in Figure 6-5. Although some of the microstructures seem to follow this inverse relationship, Q+T X-70 and centre X-70 have about the same hardness but vastly different severity of SCC and the same conclusion can be drawn from the comparison of normalized X-70 to edge X-70. Hence, hardness is not a reliable method of determining the susceptibility to near-neutral-pH SCC.

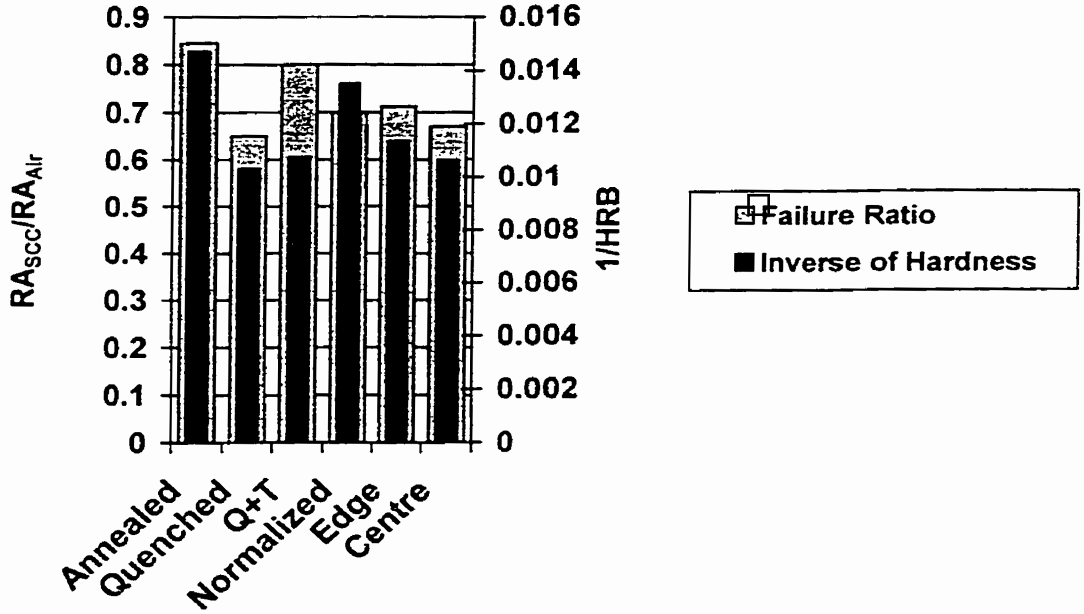

**Figure 6-5: The inverse of the hardness superimposed on the SCC results**

### 6.1.1 Transgranular Cracking of X-70 Pipeline Steel

Non-classical SCC is associated with transgranular cracking. Figure 6-6 shows a secondary crack that is transgranular, demonstrating that the proper conditions were achieved during testing. This particular crack was extremely long with a length of approximately 300 μm.

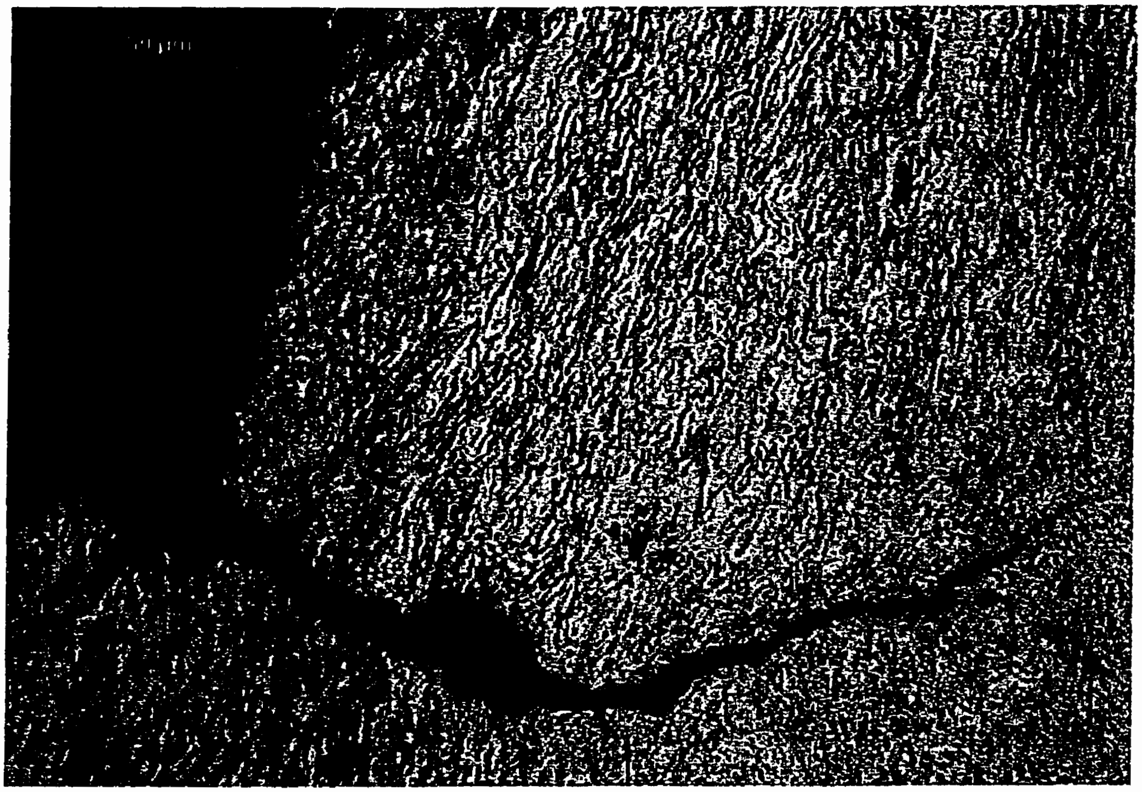

Figure 6-6: Transgranular cracking in as-received X-70

Many shallow cracks existed throughout the entire length of the specimens and typical examples are shown in Figure 6-7. The tips of these cracks were normally blunt indicating that they had become dormant.

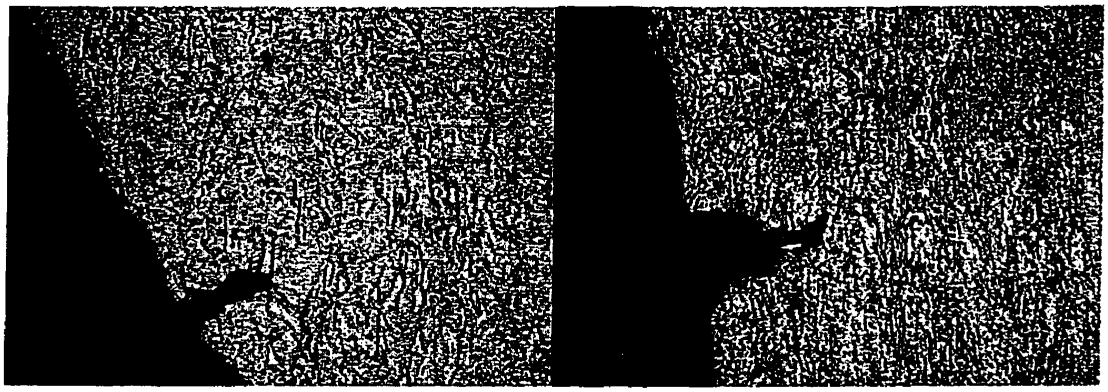

**Figure 6-7: Shallow cracks in as-received X-70**

In the above figures, the crack mouth at the surface was normally large compared to the crack tip. There are two reasons behind the large crack mouth: 1) there is corrosion of the crack walls, 2) cracks will initiate on non-metallic inclusions (Wang et al., 1998). The mouth of the crack in Figure 6-8 shows a central cavernous region with a much slenderer crack emanating from either side. The size of this cavernous region is about 20 µm in diameter, which is close to the average inclusion size for centre X-70. However, the majority of the secondary cracks did not show this type of cavernous region and the corrosion of the crack wall is more likely to cause the widening of the crack mouth.

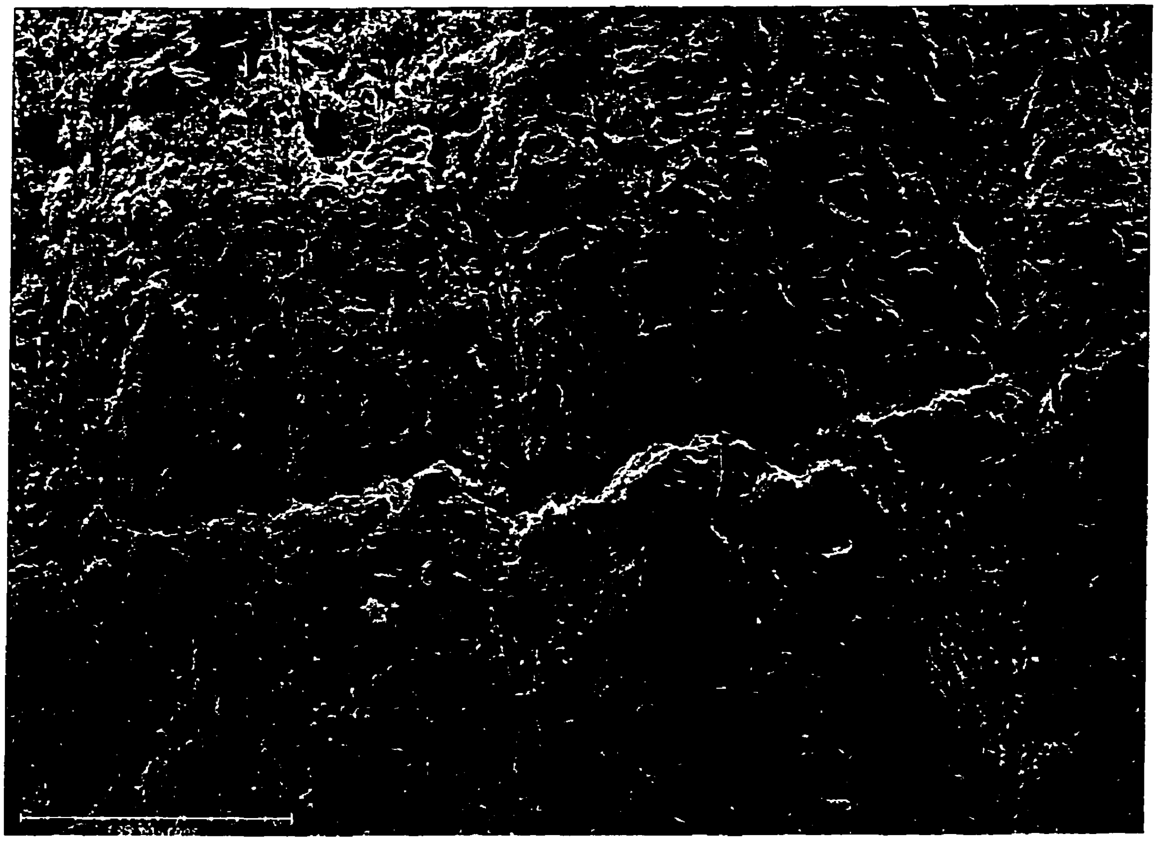

**Figure 6-8: A secondary crack in centre X-70**

### 6.1.2 Fractography of X-70 Pipeline Steel

Investigations using SSRT to produce SCC depends on two conditions:

- The first condition is that a failure ratio such as the reduction of area in the SCC causing environment divided by the reduction of area in air is below a set value such as 0.85 (set below unity since a ratio close to unity may be only a variation in material property).
- A second condition is that the fracture surface displays features that indicate the failure was due to SCC rather than mechanical failure.

The fracture features that indicate SCC are dependent on the material/environment combination so other SCC test methods or field observations are required to find the typical fracture features. Therefore, examination of the fracture surfaces is a necessity when using the SSRT method for SCC investigations.

There is another reason to examine the fracture surfaces. Section 6.1 showed that varying the microstructure of X-70 linepipe steel varied the severity of near-neutral-pH SCC. The variations in severity ranged from relatively severe in the quenched and centre X-70 to mild SCC in the annealed X-70. A hypothesis is that this severity is also reflected in the fracture surfaces.

In order to compare the fracture surfaces, the fracture surfaces of the different microstructures failed in air were examined. All microstructures showed ductile fracture as shown in Figure 6-9, which was expected based on the failure elongations of approximately 10% for the quenched X-70 to over 28% for the annealed X-70. There was, however, a difference in the fracture surfaces between the microstructures even though they did share a common fracture mode. The annealed X-70 had relatively large microvoid diameter compared to the less ductile (based on elongation data) quenched X-70. Even comparing the microstructures that had less difference in their elongation (normalized $\varepsilon_f$=17%, Q+T $\varepsilon_f$=13%) there were still some differences in the microvoid size when examining Figure 6-9c and d. In these tests, an increase in void diameter reflected an increase in the ductility.

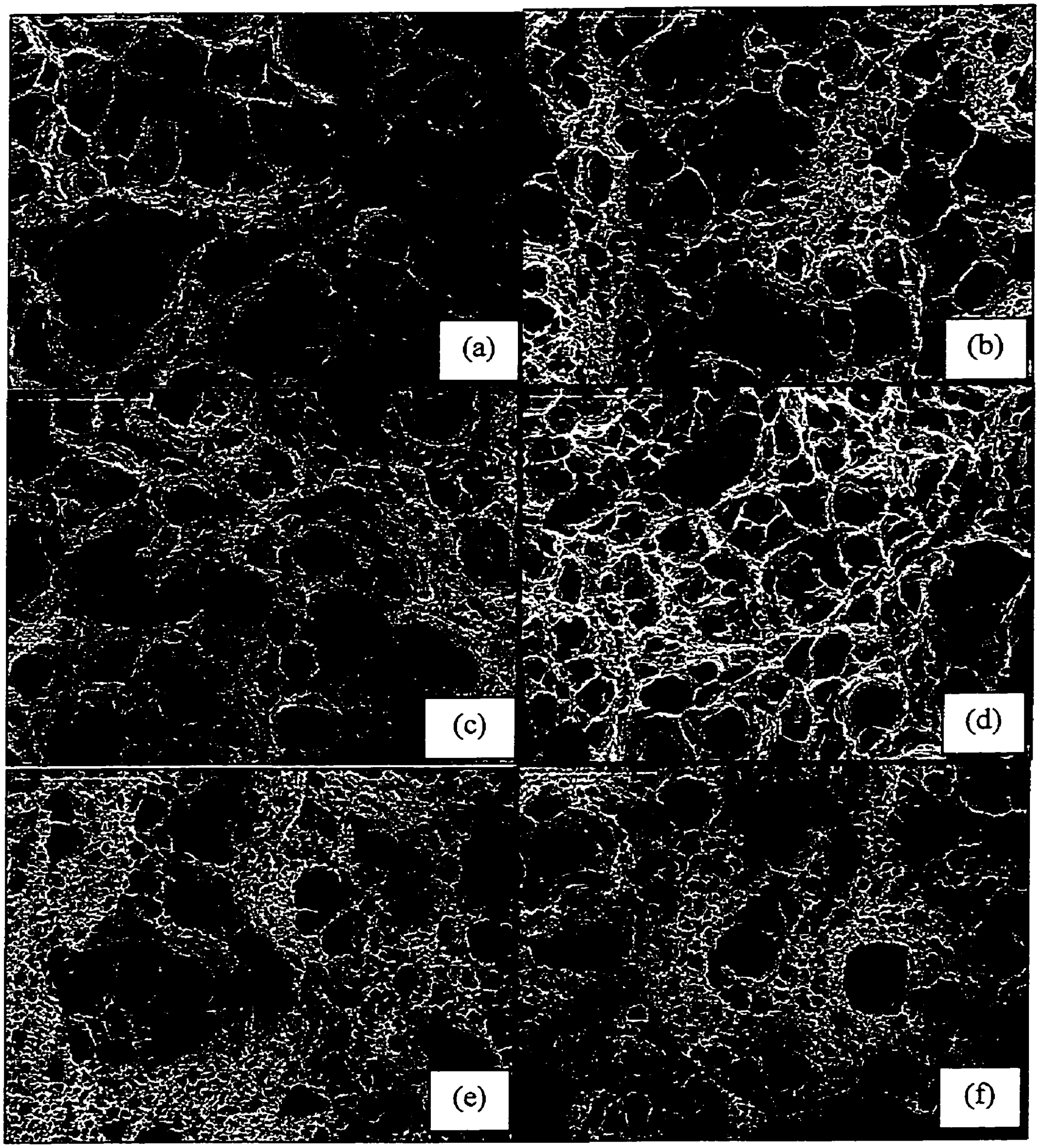

**Figure 6-9: Fracture surfaces of different microstructures of X-70 failed in air, (a) annealed, (b) quenched, (c) Q+T, (d) normalized, (e) edge, (f) centre**

The fracture surfaces of the various X-70 steel microstructures failed in NS4 are shown in Figure 6-10. The fracture surfaces show a variety of fracture features depending on the severity of the SCC. Figure 6-10a is the annealed microstructure showing a large portion of microvoid coalescence and ductile tearing. There are some quasi-cleavage facets in the upper right hand corner and a secondary crack in the upper left hand corner, both of which are indications of SCC. The quenched microstructure in Figure 6-10b shows a large quasi-cleavage facet surrounded by some very small voids. The Q+T X-70 fracture surface in Figure 6-10c shows a lot of ductile tearing and microvoids similar to the annealed microstructure. There also is a quasi-cleavage facet in the upper middle portion of the image continuing down through the middle. Figure 6-10d shows the normalized microstructure showing quasi-cleavage facets intermixed with microvoids throughout the entire image. The edge X-70 in Figure 6-10e shows microvoids surrounding a secondary crack that has a region of quasi-cleavage above it in the middle of the image. Figure 6-10f shows a large quasi-cleavage facet on the fracture surface of centre X-70 that was similar to the facets found in the quenched microstructure.

The severity of the SCC was prevalent on the fracture surfaces with the quenched and centre X-70 showing a large portion of quasi-cleavage and secondary cracking whereas the annealed and Q+T fracture surfaces showed a large portion of microvoid coalescence and some quasi-cleavage. The fracture surfaces reflect the failure ratios found in the SSRT with the quenched and centre X-70 having the most severe SCC in terms of the lowest failure ratio and the largest portion of brittle features and the annealed and Q+T having the least severe SCC with high failure ratio and a large portion of ductile features.

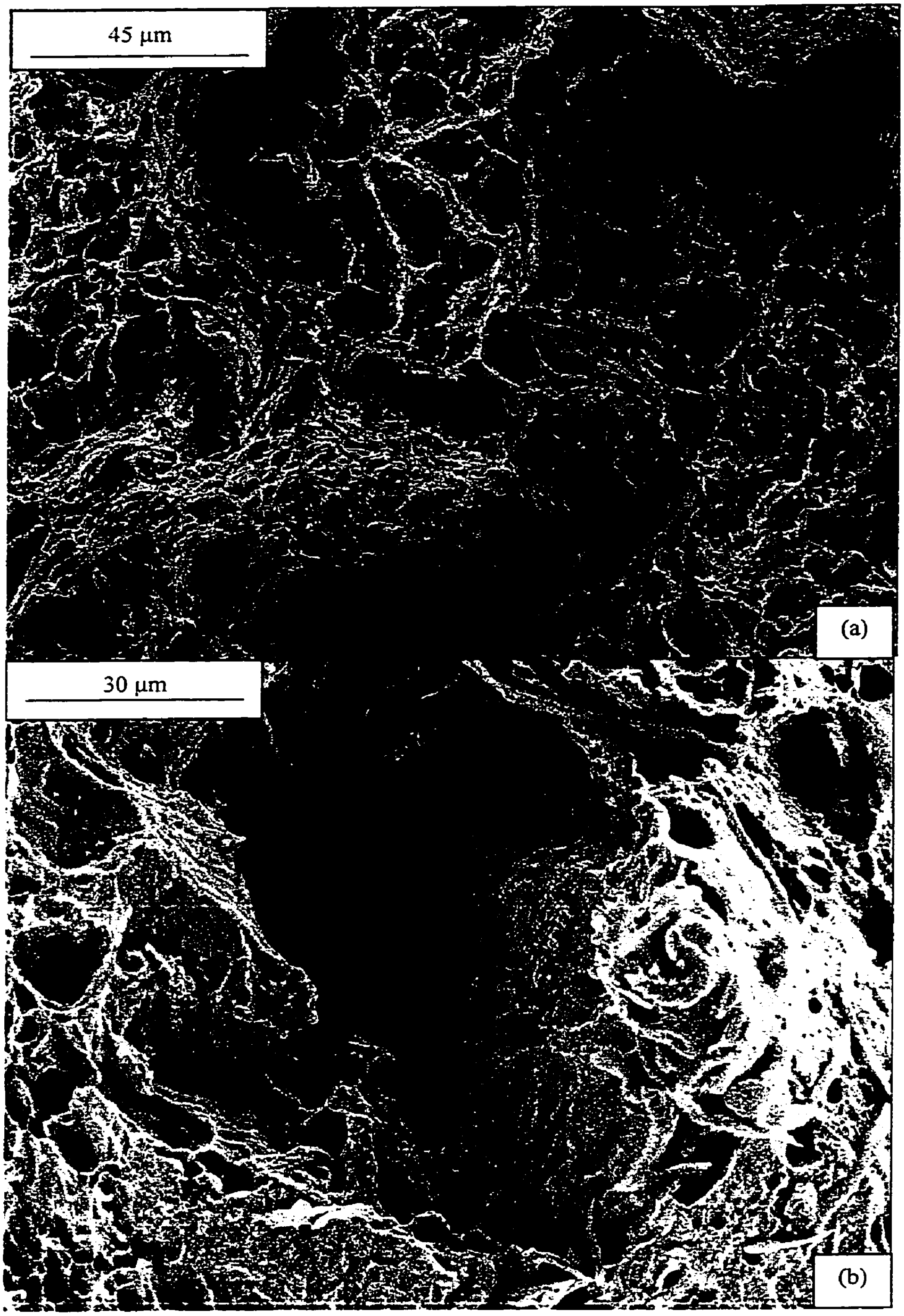

**Figure 6-10: Fracture surfaces of various X-70 steel microstructures failed in NS4, (a) annealed, (b) quenched, (c) Q+T, (d) normalized, (e) edge, (f) centre**

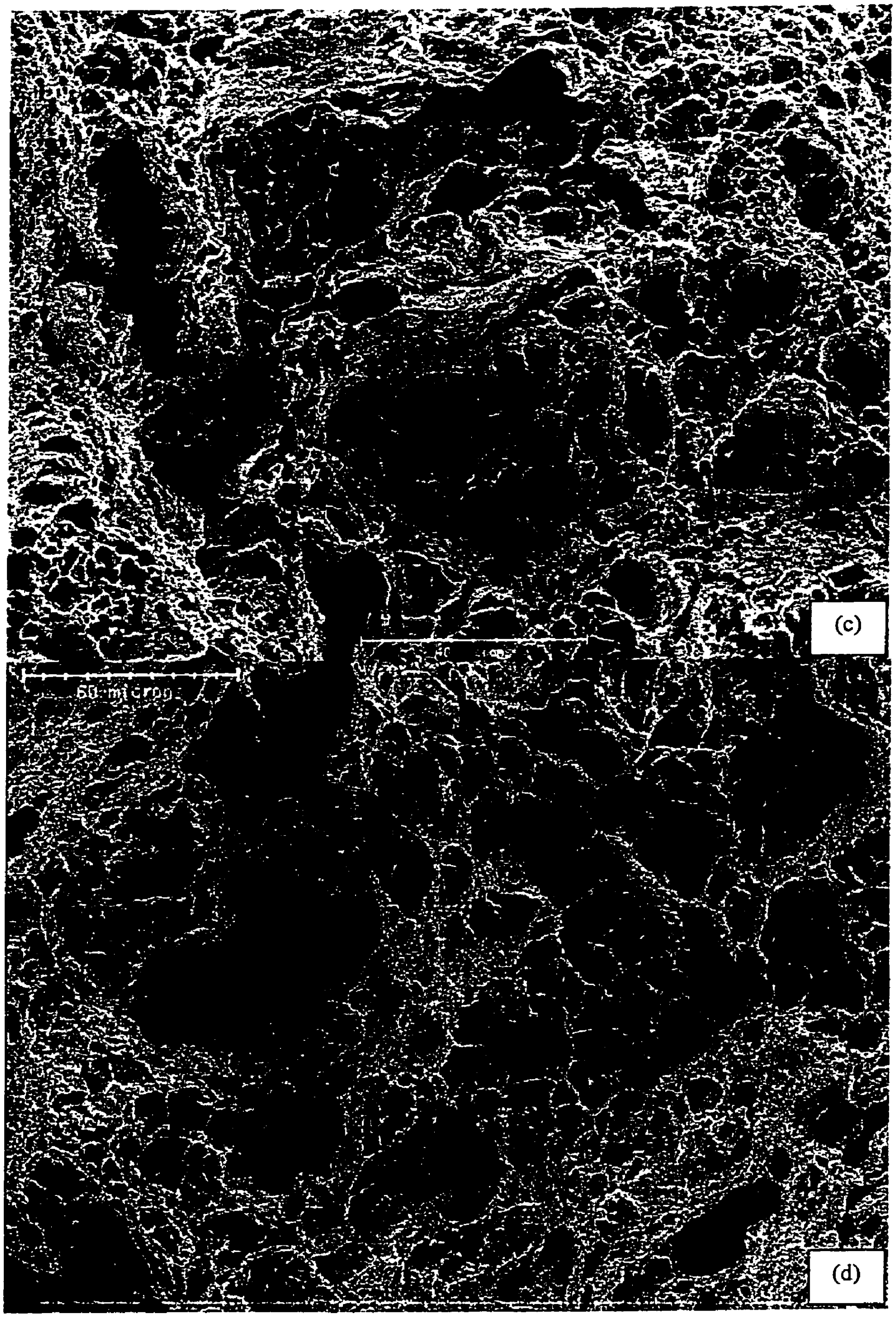

Figure 6-10: Fracture surfaces of various X-70 steel microstructures failed in NS4, (a) annealed, (b) quenched, (c) Q+T, (d) normalized, (e) edge, (f) centre

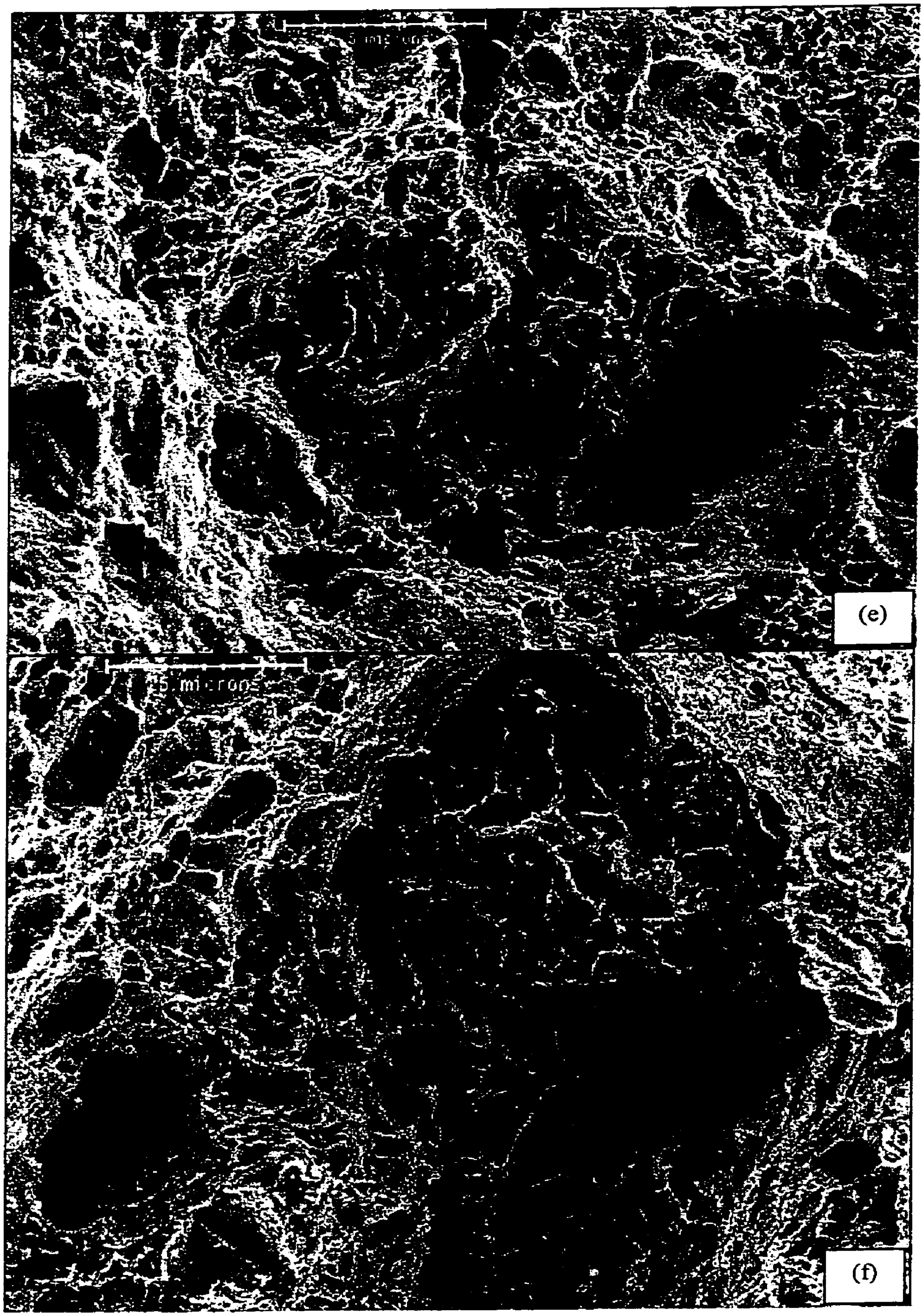

Figure 6-10: Fracture surfaces of various X-70 steel microstructures failed in NS4, (a) annealed, (b) quenched, (c) Q+T, (d) normalized, (e) edge, (f) centre

Parkins et al. (1994) also found a relationship between the severity of non-classical SCC and the degree of quasi-cleavage and microvoid coalescence. They found that as the failure ratio increased, the amount of microvoid coalescence also increased indicating that the severity of the SCC had decreased. Even though the annealed fracture surface and other fracture surfaces did show microvoid coalescence, the voids were significantly smaller than those obtained when the microstructures were failed in air. The Q+T fracture surface of Figure 6-10c had void size that basically less than 5 μm in diameter and normally had a diameter close to 1 μm compared to void diameter in air of greater than 5 μm and as high as 25 μm. The smaller void size indicates a loss in ductility and absorbed hydrogen is known to decrease void size (ASM, 1987).

The fact that the decrease in void size has been linked to hydrogen assisted failures in other materials indicates that further testing is required to find the influence of hydrogen on near-neutral-pH SCC. In the testing completed in this investigation, tensile specimens that were used in the SSRT had a low volume to surface area ratio (these specimens however were still significantly larger than the specimens used by Parkins et al. (1994)). This may impact the severity of the SCC since hydrogen is generated over the whole surface due to corrosion and is absorbed into the specimen. With a low volume to surface area ratio, the hydrogen has a small diffusion length to reach the crack front (i.e.: with these specimens of diameter 3.14 mm, hydrogen generated on the opposite side of a crack would have to diffuse 3.14 mm to reach the crack front). However, if a specimen with a larger volume to surface area ratio were used (a round specimen with a large diameter), hydrogen generated on the opposite side of a crack front would have a much larger diffusion length to reach the crack front and the increased amount of traps due to a larger volume would also impair the hydrogen from reaching the crack front. Hence, the role of hydrogen generated outside the crack front could be differentiated by varying the diameter of a round SSRT specimen and this is left as a recommendation.

The quasi-cleavage facets were sometimes associated with a titanium nitride precipitate as shown in Figure 6-11. This large quasi-cleavage facet has a centrally located black square feature that was determined to be a titanium nitride based on the EDX analysis and the morphology. Titanium nitrides are hydrogen traps (Garet et al., 1998) and the higher levels of hydrogen may influence the subsequent cracking in the adjacent region. Although a single precipitate initiating fracture in non-classical SCC has not been reported before, the role of precipitates/inclusions influencing the fracture has been reported (Ahmed et al., 1997).

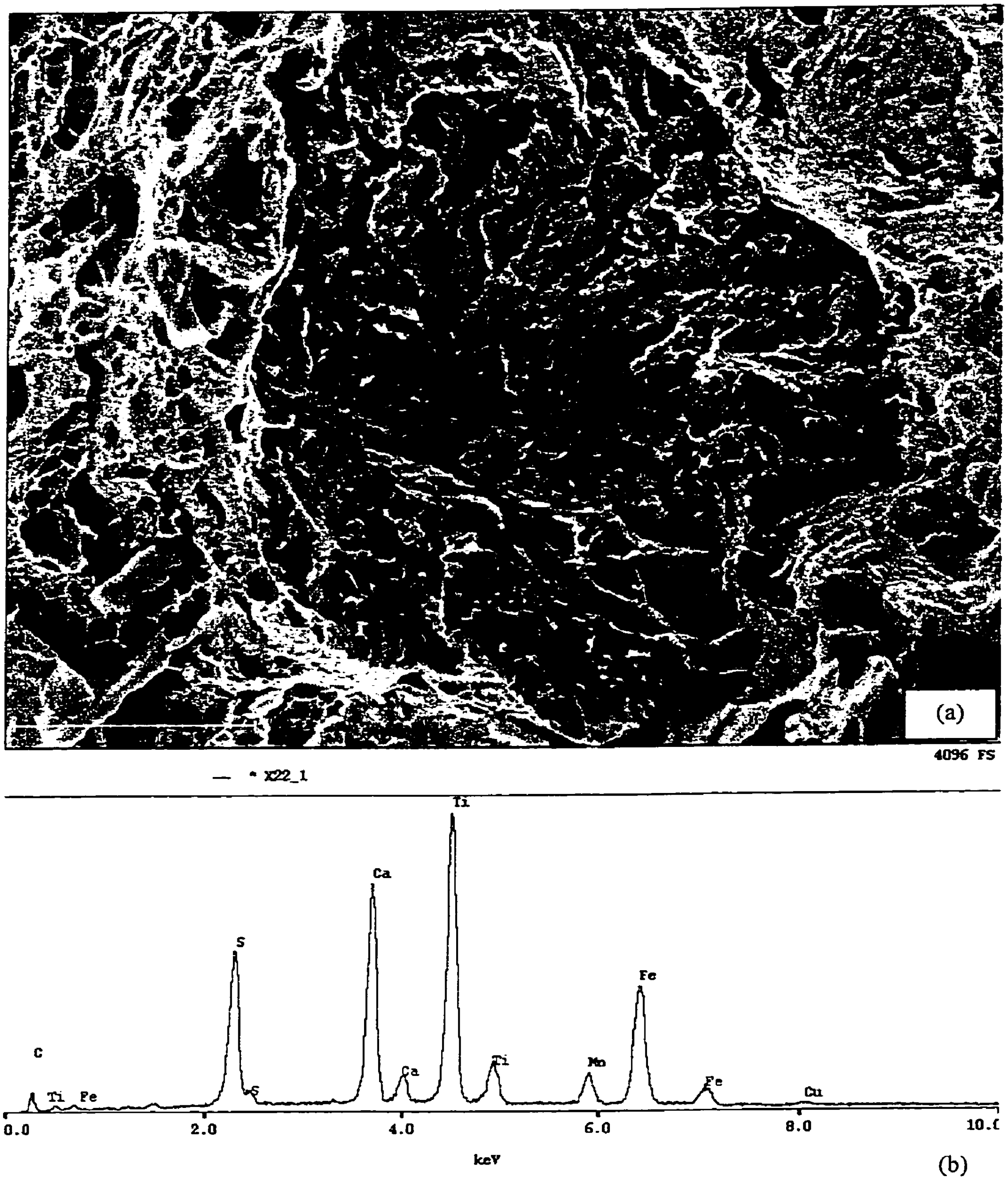

**Figure 6-11: (a) Quasi-cleavage fracture surface, (b) EDX analysis of the centrally located precipitate**

Figure 6-12 shows a schematic of the fracture sequence during a SSRT. Hydrogen generated from corrosion and absorbed into the steel accumulates on the titanium nitride due to either a high triaxial stress field around the nitride or microvoids formed around the nitride during the nitride formation. When the combination of stress and hydrogen concentration reaches a certain limit, fracture takes place along a fracture plane(s) revealing either a cleavage or quasi-cleavage facet with a titanium nitride located on the facet.

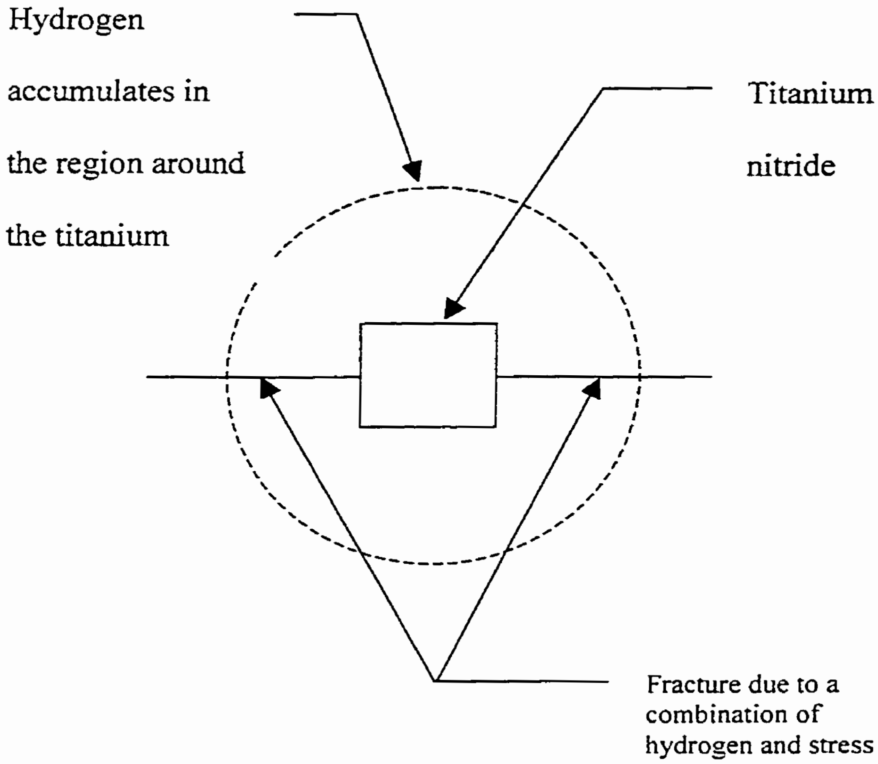

**Figure 6-12: Schematic of the influence of the titanium nitride on fracture**

## *6.2 Carbon Steel*

SSRT testing was also done on a variety of carbon steel microstructures in order to confirm the result from the X-70 linepipe SCC tests. Figure 6-13 displays the carbon steel results for both 1018 and 1045 carbon steels. The microstructure of the 1018 steel affects the SCC susceptibility with the annealed microstructure having the highest resistance and the Q+T425 having the lowest resistance to SCC. The effect of microstructure on the susceptibility of the 1045 steel is only slight since the corrosion rates for these 1045 microstructures were almost identical. The variation of the SCC severity with microstructure reinforces the previous results found with the X-70 linepipe that SCC severity is a function of microstructure.

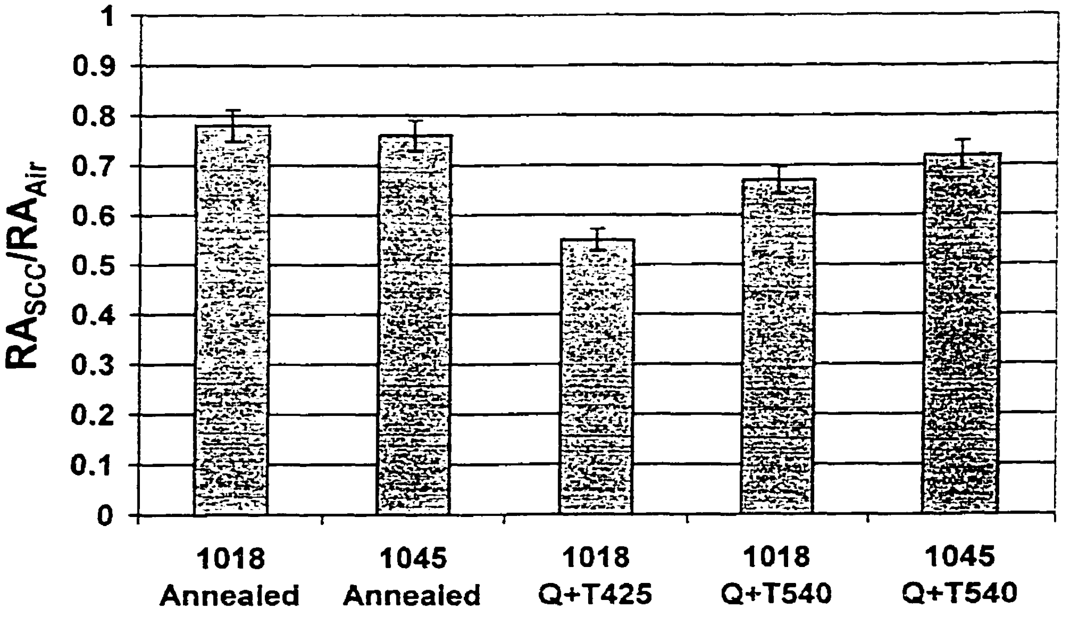

**Figure 6-13: SCC results for various carbon steel microstructures**

Figure 6-14 compares the corrosion characteristics to the SCC susceptibility of these microstructures. Similar to the X-70 results, the carbon steel SCC susceptibility shows a strong relationship with the corrosion characteristics for each microstructure indicating that the mechanism for the SCC is likely an anodic dissolution mechanism.

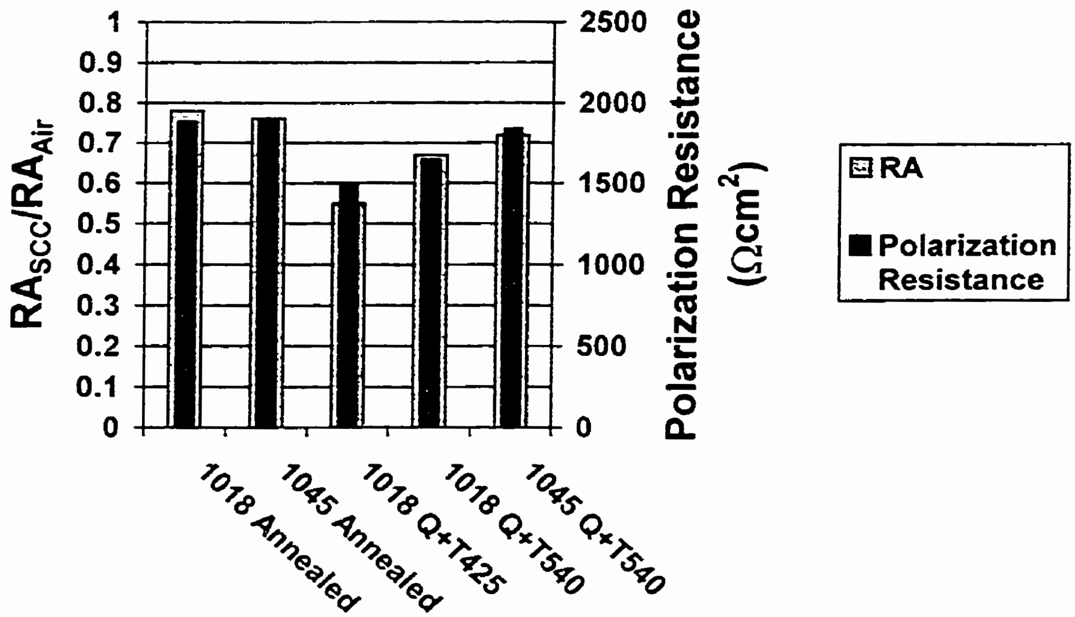

Figure 6-14: Comparison of SCC susceptibility and polarization resistance for carbon steel

### 6.2.1 Fractography of Carbon Steel

The carbon steel exhibited transgranular cracking typical of near-neutral-pH SCC. The fracture surfaces of the carbon steel failed in air showed purely ductile features similar to Figure 6-9. Figure 6-15 shows the fracture surfaces of the carbon steel failed in the NS4 environment.

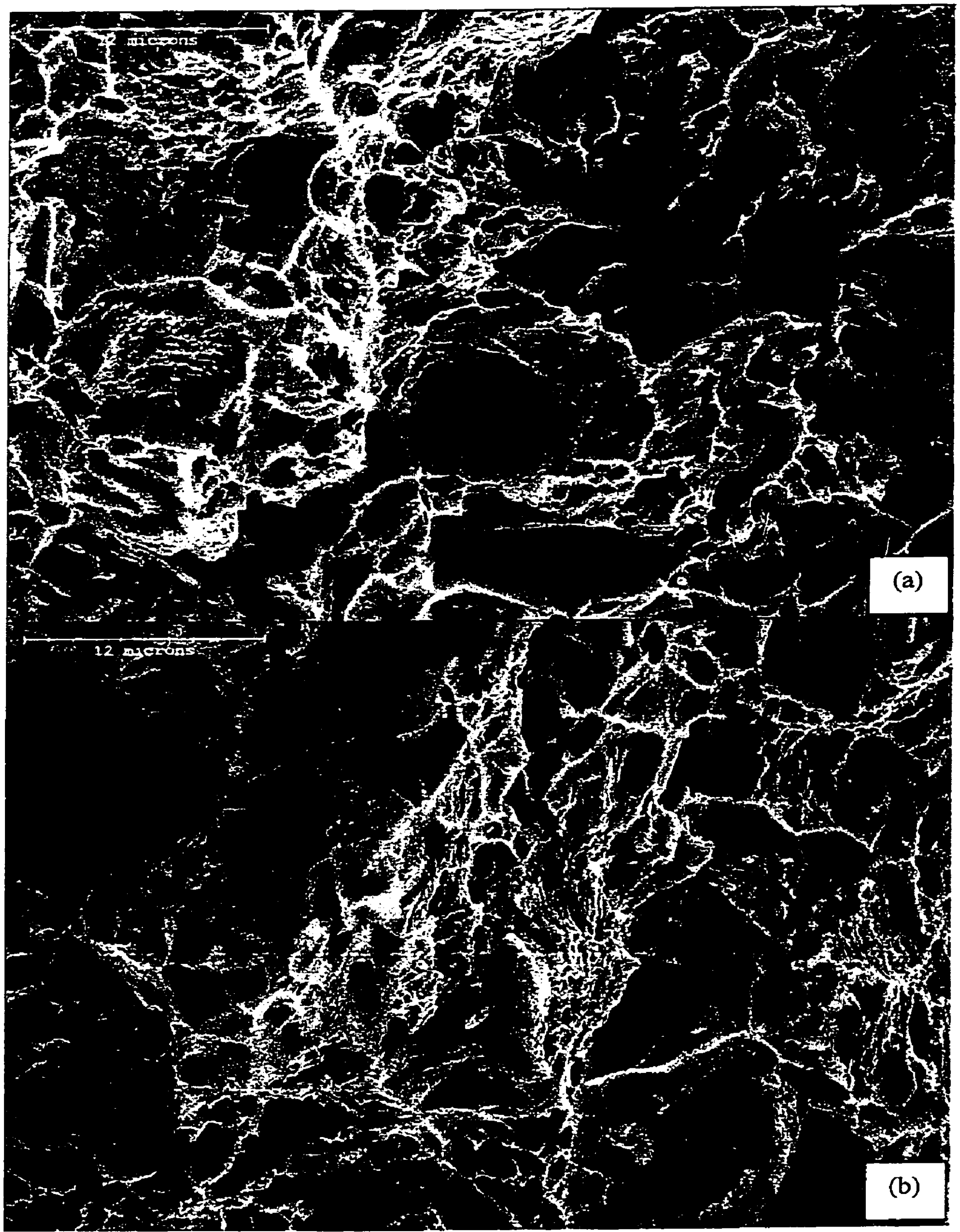

**Figure 6-15: Typical fracture surfaces of carbon steel microstructures failed in NS4, (a) 1018 annealed, (b) 1045 annealed, (c) Q+T425 1018, (d) Q+T540 1018, (e) Q+T540 1045**

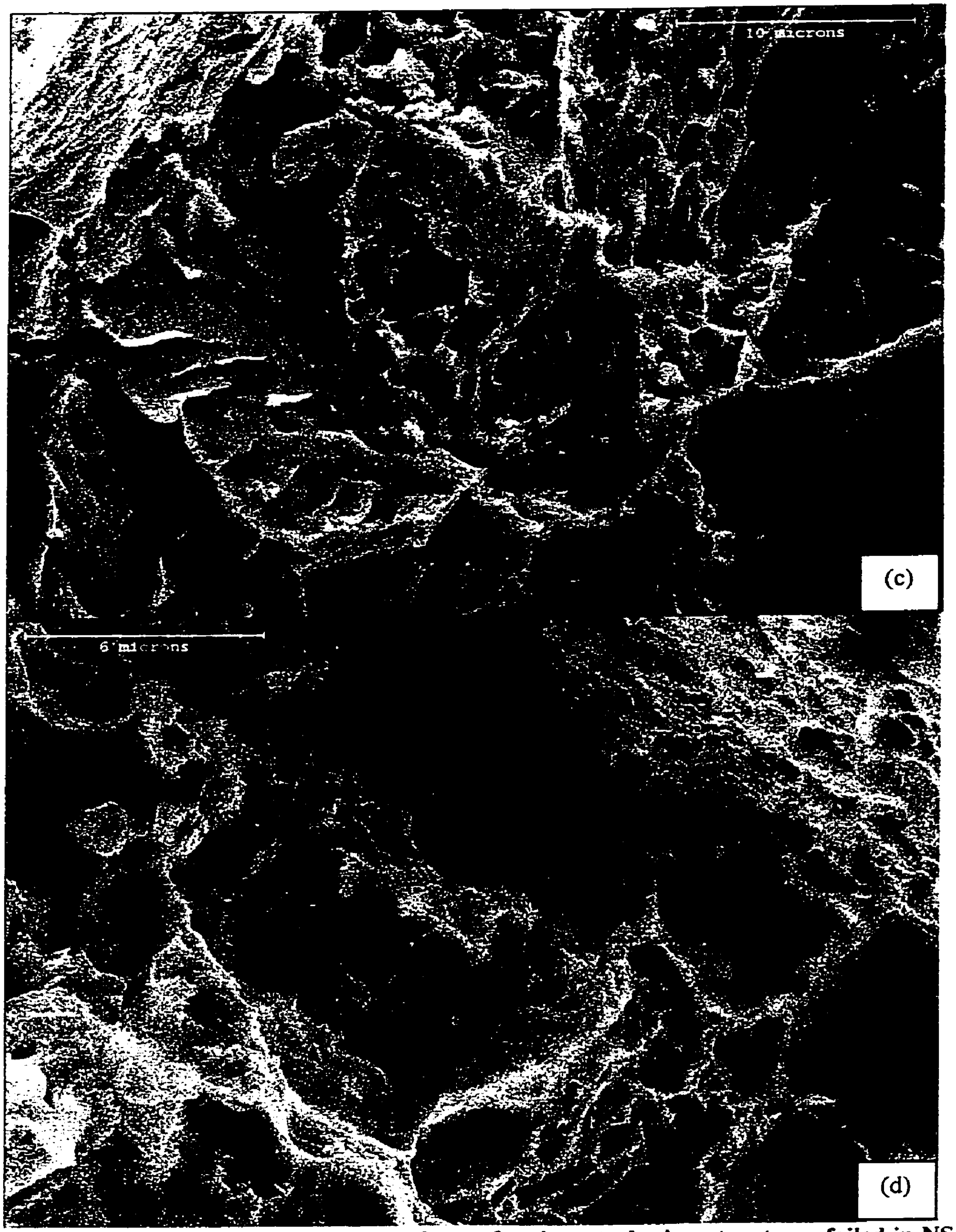

**Figure 6-15: Typical fracture surfaces of carbon steel microstructures failed in NS4, (a) 1018 annealed, (b) 1045 annealed, (c) Q+T425 1018, (d) Q+T540 1018, (e) Q+T540 1045**

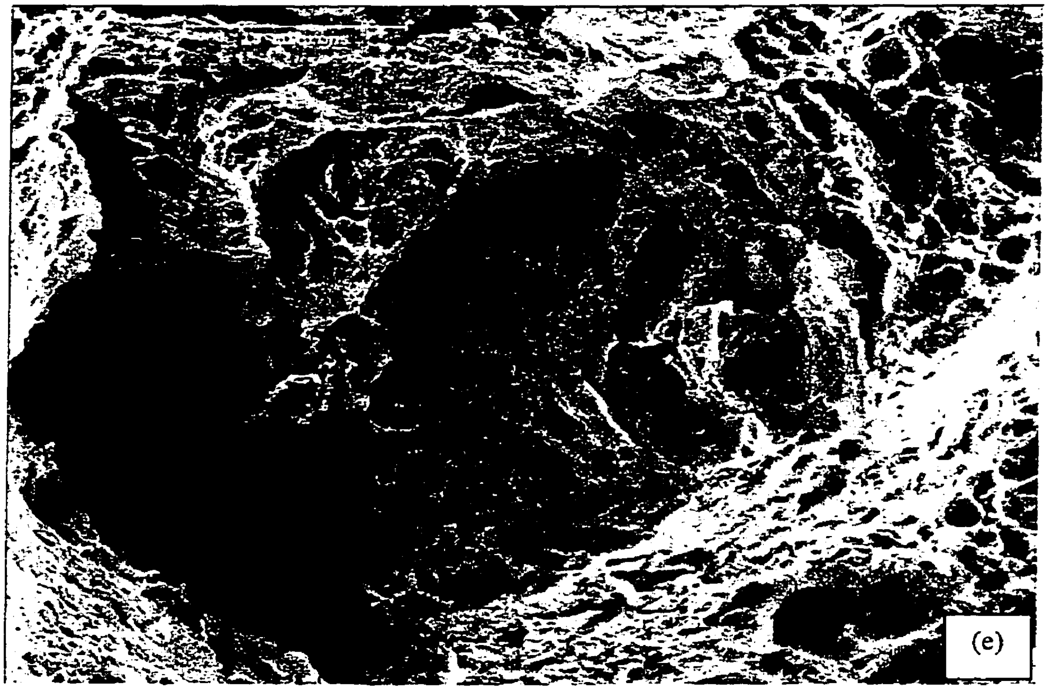

**Figure 6-15: Typical fracture surfaces of carbon steel microstructures failed in NS4, (a) 1018 annealed, (b) 1045 annealed, (c) Q+T425 1018, (d) Q+T540 1018, (e) Q+T540 1045**

The surfaces of Figure 6-15 show varying amounts of cleavage, quasi-cleavage and microvoids with the annealed microstructures showing more microvoid coalescence than the cleavage features and the Q+T425 1018 showing more quasi-cleavage than microvoid coalescence. The fracture surfaces seem to reflect the failure ratios of the SSRT with severity of the SCC reflected by the ratio of quasi-cleavage to ductile features. This was similar to the X-70 steel fracture surfaces presented earlier and is in agreement with Parkins et al. (1994).

# Chapter 7 Conclusions and Recommendations

## *7.1 Conclusions*

The following are the conclusions based on the experimental results for the corrosion and SCC of X-70 pipeline steel and carbon steel in NS4:

1) The as-received X-70 had a variation of microstructure across the width of the skelp. Material from the edge of the skelp had a larger grain size and a lower content of both retained austenite and inclusions.
2) X-70 linepipe, AISI 1018 and AISI 1045 carbon steels all exhibit active corrosion behaviour in NS4 with the corrosion rate dependent on the microstructure. Corrosion rate decreases due to the following:
    - Increasing grain size;
    - Decreasing amount of inclusions and retained austenite;
    - With a decrease in the surface roughness.
3) Corroded steel surfaces have cathodic regions centred on a titanium nitride for the X-70 steel and an inclusion for the carbon steel.
4) An increase in the amount of cold work decreases the corrosion rate for X-70 linepipe steel. Although there is an increase in the cathodic Tafel constant, the role of the cold work in decreasing the corrosion rate remains unclear.
5) Cold work will increase the harmful effects of hydrogen on the corrosion rate of X-70.

6) The severity of near-neutral-pH SCC is dependant on microstructure for both X-70 and the carbon steels. Decreasing grain size is deleterious to near-neutral-pH SCC.
7) Large titanium nitrides may intiate brittle failure.
8) There is a direct relationship between the corrosion rate and the SSRT results for near-neutral-pH SCC indicating that the mechanism is an anodic dissolution mechanism. This was shown with both the X-70 steel in Figure 6-4 and the carbon steels in Figure 6-14.

## *7.2 Recommendations*

The following are recommendations for further study into the aspects of corrosion in the NS4 environment and near-neutral-pH SCC:

1) The corrosion characteristics of titanium nitride are unknown. Knowledge of their corrosion characteristics will provide a clearer view of their role in the corrosion of pipeline steel. The effect of increasing or decreasing the amount of titanium nitrides and the effect of the large titanium nitrides compared to the small titanium nitrides also needs to be gauged.
2) The corrosion surface of the linepipe showed cathodic regions centred on a titanium nitride. Attempts should be made to find if the cathodic region is due solely to the galvanic effect of the nitride or is due to a titanium distribution about the nitride.
3) The effect of cold work on the corrosion rate is unclear. Experiments should be performed on other types or grades of steel to determine the

effect of cold work. Straining a sample should not be limited to cold rolling, but tensile straining should also be tried.

4) The effect of hydrogen on the corrosion rate should be studied to correlate the increase in the corrosion rate to hydrogen concentration within the metal.

5) The effect of surface preparation should be investigated. Although surface roughness was looked at in this investigation, shot peening or grit blasting should be used to find if the residual compressive stress affects the corrosion rate.

6) The effect of microstructure on near-neutral-pH SCC for X-70 steel should be further tested using a different test method (cyclic tests) to confirm these results.

7) The effect of cold work on the SCC performance of X-70 steel needs investigation to find the overall effect and if there is a critical level of cold work that decreases or enhances the effect.

8) SSRT using specimens of varying sizes should be completed to see the effect of specimen size on near-neutral-pH SCC. If hydrogen plays an important role, then increasing the diameter of a round tensile specimen will increase the volume to surface area ratio and hence decrease the amount of available hydrogen at the crack front and this should increase the resistance to SCC. If the crack advances by a purely anodic mechanism, varying the specimen size should have a very small influence on the resistance.

## References

Ahmed, T.M., Lambert, S.B., Sutherby, R., Plumtree, A., 1997, "Cyclic Crack Growth Rates of X-60 Pipeline Steel in a Neutral Dilute Solution," *Corrosion*, Vol. 53, No. 7, pp. 581-590.

ASM, 1987, *Metals Handook Ninth Edition Volume 12 Fractography*, ASM International, Metals Park, Ohio, U.S..

Baker, T.R., 1983, "Stress Corrosion Cracking In High Pressure Natural Gas Pipelines," *APIA Annual Convention*

Baker, T.R., Parkins, R.N., and Rochfort G.G., 1986, "Investigations Relating to Stress Corrosion Cracking on The Pipeline Authority's Moomba to Sydney Pipeline," *Proc. 7th Symp. Line Pipe Research*, AGA, Arlingtion, Virginia, Catalogue No. L51495/27-1.

Beachem, C.D., 1972, "A New Model for Hydrogen-Assisted Cracking Hydrogen Embrittlement," *Metall. Trans. A*, Vol. 3, pp. 437-451.

Beams, J. W., 1959, "Structure and Properties of Thin Films," Neugebauer, Newkirk, and Vermilyea, Editors, John Wiley & Sons, New York, pp. 183.

Beavers, J.A., Durr, C.L., and Shademan, S.S., 1998, "Mechanistic studies on near-neutral-pH SCC on underground pipelines," *Proc. of the Intern. Symp. on Materials for Resource Recovery and Transport*, Metall. Soc. of CIM, Calgary, Canada, pp.51-69.

Beavers, J.A., Thompson, N.G., and Coulson, K.E.W., 1993, "Effects of Surface Preparation and Coatings on SCC Susceptibility of Line Pipe Phase 1- Laboratory Studies," Corrosion/93, NACE, Houston, TX, Paper No. 597.

Champion, F.A., 1948, *Symp. Internal Stresses in Metals and Alloys*, Institute of Metals, p. 468.

Charles, E.A, and Parkins, R.N., 1995, "Generation of Stress Corrosion Cracking Environments at Pipeline Surfaces," *Corrosion*, Vol. 51, No. 7, pp. 518-527.

Cottis, B, and Turgoose, S, 1999, *Corrosion Testing Made Easy: Impedance and Noise Analysis*, NACE, Houston, U.S..

Delanty, B. and O'Beirne, J., 1992, "Major Field Study Comparing Pipeline SCC with Coatings," *Oil and Gas Journal*, June 15, 1992, pp. 39-44.

Edeleanu, C, and Forty, A.J., 1960, "Some Observations on the Stress-Corrosion Cracking of α-Brass and Similar Alloys," *Phil. Mag.*, Vol. 5, pp. 1029-1040.

Eklund, G., 1970, "Corrosion Around Slag Inclusions in Steel," *Jernkonterets Ann*, Vol. 154, No. 7, pp. 321-325.

Engle, H.J., 1971, "The Role of Surface Films on Stress Corrosion Cracking of Metals," *The Theory of Stress Corrosion Cracking in Alloys*, North Atlantic Treaty Organization, Brussels, pp. 86-104.

Fessler, R.R., 1976, "Combination of Conditions causes Stress-Corrosion Cracking," *Oil and Gas Journal,* Feb. 16, 1976 , pp. 81-83.

Forty, A. J., and Humble P., 1963, "The Influence of Surface Tarnish on the Stress-corrosion of α-brass" *Philos. Mag.*, Vol 8, pp. 247-264.

France, W.D., Jr., 1970, "Effects of Stress and Plastic Deformation on the Corrosion of Steel," *Corrosion*, Vol. 26, No. 5, pp. 189-199.

Gahr, S., Grossbech, M.L. and Birnbaum, H.K., 1977, "Hydrogen Embrittlement of Nb I-Mascroscopic Behaviour at Low Temperatures," *Acta Metall.*, Vol. 3, pp. 125-134.

Galvele, J.R., 1992, "Surface Mobility Mechanism of SCC," *Parkins Symposium on Fundmental Aspects of Stress Corrosion Cracking*, Bruemmer, S.M., et al., eds., TMS, pp. 85-102.

Garet, M., Brass, A.M., Haut, C., and Guttierez-Soloana, F., 1998, "Hydrogen Trapping on Non Metallic Inclusions in Cr-Mn Low Alloy Steels," *Corrosion Science*, Vol. 40, No. 7., pp. 1073-1086.

Gu, B., Luo, J., and Mao, X., 1999, "Hydrogen-Facilitated Anodic Dissolution-Type Stress Corrosion Cracking of Pipeline Steels in Near-Neutral pH Solution," *Corrosion*, Vol. 55, No. 1, pp.96-106.

Harston, J.D., and Scully, J.C., 1969, "Stress Corrosion of Type 304 Steel in $H_2SO_4$-NaCl Environments at Room Temperature," *Corrosion*, Vol. 25, No. 12, pp. 493-501.

Jones, D.A., 1996, *Principles and Prevention of Corrosion*, Prentice-Hall, Inc., Toronto, Canada, pp. 255-256.

Huang, H., and Shaw, W.J.D., 1992, "Electrochemical Aspects of Cold Work Effect on Corrosion of Mild Steel in Sour Gas Environments," *Corrosion*, Vol. 48, No. 11, pp. 931-939.

Huang, H-H, Tsai, W-T, and Lee, J-T, 1994, "The Influence of Microstructure and Composition on the Electrochemical Behaviour of A516 Steel Weldment," *Corrosion Science*, Vol. 36, No. 6, pp. 1027-1038.

IIW, 1988, "Guide to the Light Microscope Examination of Ferritic Steel Weld Metals," IIW Doc.No.IX-1533-88, IXJ-123-87 Revision 2.

Liu, X., Mao, X., and Revie, R.W., 1993, "Pitting Corrosion Behaviour of Pipeline Steel in Solutions with Coating Disbonded Area Chemistry and in Bicarbonate Solutions," *Corrosion Control for Low-Cost Reliability, 12th International Corrosion Congress Preceedings*, NACE, Houston, Vol. 4, pp. 2831-2839.

Logan, H.L., 1952, *J. Res. Natl.Bur. Stand.*, Vol. 48, p. 99.

Lopez, H.F., Raghunath, R., Albarran, J.L., and L. Martinez, 1996, "Microstructural Aspects of Sulfide Stress Cracking in an API X-80 Pipeline Steel," *Metall. Trans. A,*, Vol. 27A, pp. 3601-3611.

Manuel, R.W., 1984, "Effect of Carbide Structure on the Corrosion Resistance of Steel," *$CO_2$ Corrosion in Oil and Gas Production-Selected Paper, Abstracts, and References*, NACE, pp. 197-206.

McEvily, A. J., and Bond, P. A., 1965, "On the Initiation and Growth of Stress Corrosion Cracks in Tarnished Brass," *J. Electrochem. Soc.*, Vol 112, pp. 131-138.

National Energy Board, 1996, "Public inquiry concerning stress corrosion cracking on Canadian oil and gas pipeline," MH-2-95.

Nesic, S., Postlethwaite, J., and Olsen, S., 1996, "An Electrochemical Model for Prediction of Corrosion of Mild Steel in Aqueous Carbon Dioxide Solutions," *Corrosion*, Vol. 52, No. 4, pp. 280-294.

Newman, R.C., and Procter, R.P.M., 1990, "Stress Corrosion Cracking: 1965-1990," *Br. Corr. Jour.*, Vol. 25, pp. 259-269.

Oriani, R.A., 1977, "A Decohesion Theory for Hydrogen-Induced Crack Propagation,"*Stress Corrosion Cracking and Hydrogen Embrittlement of Iron Base Alloys*, Staehle R.W., Hochmann, J., McCright, R.D., and Slater, J.E. eds., NACE, Houston, TX, pp. 351-358.

Parkins, R.N., 1974, "The Controlling Parameters in Stress-Corrosion Cracking," *5th Symp. on Line Pipe Research*, AGA, Houston, Texas, paper V.

Parkins, R.N., Belhimer, E., and Blanchard Jr., W.K., 1993, "Stress Corrosion Cracking Characteristics of a Range of Pipeline Steels in Carbonate-Bicarbonate Solution," *Corrosion*, Vol. 49, No. 12, pp. 951-966.

Parkins, R.N., Blanchard Jr., W.K., and Delanty, B.S., 1994, "Transgranular Stress Corrosion Cracking of High-Pressure Pipelines in Contact with Solutions of Near Neutral pH," *Corrosion*, Vol. 50, No. 5, pp. 394-408.

Petch, N.J. and Stables, P., 1952, "Delayed Fracture of Metals under Static Load," *Nature*, Vol. 169, pp. 842-843.

Pickering, H.W., and Swann, P.R., 1973, "Electron Metallography of Chemical Attack Upon Some Alloys Susceptible to Stress Corrosion Cracking," *Corrosion*, Vol. 19, pp. 373t-389t.

Pilkey, A.K., Lambert, S.B., Plumtree, A., 1995, "Stress Corrosion Cracking of X-60 Line Pipe Steel in a Carbonate-Bicarbonate Solution," *Corrosion*, Vol. 51, No. 2, pp. 91-96.

Pugh, E. N., 1977, "A Post Conference Evaluation of Our Understanding of the Failure Mechanisms," *Stress Corrosion Cracking and Hydrogen Embrittlement of Iron Based Alloys*, NACE, Houston, TX, pp. 37-51.

Pugh, E.N., 1985, "Progress Towards Understanding the Stress Corrosion Problem," *Corrosion*, Vol. 41, pp. 517-526.

Revie, R.W., and Uhlig, H.H., 1974, "Effect of Applied Potential and Surface Dissolution on the Creep Behaviour of Copper," *Acta Metall.*, Vol. 22, pp. 619-627.

Scully, J.C, 1975, "Stress Corrosion Crack Propagation: A Constant Charge Criterion," *Corrosion Science*, Vol. 15, pp. 207-224.

Sharma, U., 2000, "Microstructural Characterization of Microalloyed Linepipe Steel" Master's Thesis, Department of Chemical and Materials Engineering, University of Alberta.

Sieradzki, K., and Newman, R.C., 1985, "Brittle Behaviour of Ductile Metals During Stress-Corrosion Cracking," *Phil. Mag.*, Vol. 51, No. 1, pp. 95-132.

Staehle, R.W., 1971, "Stress Corrosion Cracking of Fe-Cr-Ni Alloy System," *The Theory of Stress Corrosion Cracking in Alloys*, North Atlantic Treaty Organization, pp. 223-288.

Stafford, D.A., Wheatley, B.I., and Hughes, D.E., 1980, "Anaerobic Digestion," Applied Science Publishers Ltd, London, England.

Sutcliffe, J.M., Fessler, R.R., Boyd, W.K., and Parkins, R.N., 1972, "Stress Corrosion Cracking of Carbon Steels in Carbonate Solutions," *Corrosion*, Vol. 28, No. 8, pp. 313-320.

Sutherby, R.L., 1998, "The CEPA Report on Circumferential Stress Corrosion Cracking," *Proceedings of the International Pipeline Conference*, ASME, New York, Vol. 1, pp. 493-503.

Tabata, T., and Birnbaum, H.K., 1983, "Direct Observations of the Effect of Hydrogen on the Behaviour of Dislocations in Iron," *Scripta. Metall.*, Vol. 17, No. 7, pp. 947-950.

Tabata, T., and Birnbaum, H.K., 1984, "Direct Observations of Hydrogen-Enhanced Crack Propagation in Iron," *Scripta. Metall.*, Vol. 18, No. 3, pp. 231-236.

Tetelman, A.S., 1969, "The Mechanism of Hydrogen Embrittlement in Steel," *Proceedings of Conference Fundamental Aspects of Stress-Corrosion Cracking*, Staehle, R.W., Forty, A.J., and van Rooyen, D., eds., NACE, Houston, TX, pp. 446-464.

Tomlison, W.J., and Smith, K.P., 1983, "The Effect of Shot Peening on the Polarization Behaviour of Steel," *Corrosion*, Vol. 39, No. 11, pp. 432-434.

Troiano, A.R., 1960, "The Role of Hydrogen and Other Interstitials in the Mechanical Behviour of Metals," *Trans. ASM*, Vol. 52, pp. 54-80.

Uhlig, H.H., 1959, *Physical Metallurgy of Stress Corrosion Fracture*, Rhodin, T.N., ed., Interscience, pp. 1-16.

Vermilyea, D.A., 1972, "A Theory for the Propagation of Stress Corrosion Cracks in Metals," *Joun. Electrochemical Soc.*, Vol. 119, No. 4, pp.405-407.

Wilmott, M., Erno, B., Jack, T., and Worhtingham, R., 1998, "The Role of Coatings in the Development of Corrosion and Stress Corrosion Cracking on Gas Transmission Pipelines," *Proceedings of the International Pipeline Conference*, ASME, New York, Vol. 1, pp. 399-408.

Wang, Y-Z, Revie, R.W., Shehata, M.T., Parkins, R.N., and Krist, K., 1998, "Initiation of Environment Induced Cracking in Pipeline Steel: Microstructural Correlations," *Proceedings of the International Pipeline Conference*, ASME, New York, Vol. 1, pp. 529-542.

Wenk, R.L., 1974, "Field Investigation of Stress Corrosion Cracking," *5th Symposium on Line Pipe Research*, American Gas Association, Inc., Catalog No. L30174, p. T-1.

Wilmott, M.J., and Diakow, D.A., 1996, "Factors Influencing Stress Corrosion Cracking of Gas Transmission Pipelines: Detailed Studies Following a Pipeline Failure. Part 2: Pipe Metallurgy and Mechanical Testing," *Proceedings of the International Pipeline Conference*, ASME, New York, pp. 573-585.

Wilmott, M., and Sutherby, R.L., 1998, "The Role of Pressure and Pressure Fluctuations in the Growth of Stress Corrosion in Line Pipe Steels," *Proceedings of the International Pipeline Conference*, ASME, New York, Vol. 1, pp. 409-422.

Wiskel, B., 1999, Private Communication

Wranglen, G., 1974, "Electrochemical Properties of Sulfides in Steel and the Role of Sulfides in the Initiation of Corrosion," *Sulfide Inclusions in Steel*, ASM, Metals Park, Ohio, pp. 361-379.

Xie, S.X., and Hirth, J.P., 1982, "Permeation of Hydrogen, Trapping, and Damage in Spheroidized AISI 1090 Steel," *Corrosion*, Vol. 38, No. 9, pp. 486-493.

Yang, M.Z., Luo, J.L., Yang, Q., Qiao, L.J., Qin, Z.Q. and Norton, P.R., 1999, "Effects of Hydrogen on Semiconductivity of Passive Film and Corrosion Behavior of 310 Stainless Steel," *Journal of the Electrochemical Society*, Vol. 146, No. 6, pp. 2107-2112.

Zapffe, C. and C. Sims, 1941, "Hydrogen Embrittlement, Internal Stress and Defects in Steel," *Trans. AIME*, Vol. 145, pp. 225-259.

Zhang, X.-Y., Lambert, S.B., Sutherby, R., and Plumtree, A., 1999, "Transgranular Stress Corrosion Cracking of X-60 Pipeline Steel in Simulated Ground Water," *Corrosion*, Vol. 55, No. 3, pp. 297-305.